

# **Towards Autonomous and Robust Damage Detection and Health**

## **Monitoring of Mechanical Systems**

Yi Lu, Ph. D.

University of Connecticut, 2011

In this dissertation research, a series of signal processing and decision making techniques have been developed for both machinery condition monitoring (passive detection) and structural damage detection (active interrogation), as one research thrust. In one effort, utilizing accelerometer and microphone signals collected around a gearbox testbed during its operation, a data-driven framework that combines information from multiple sensors and fundamental physics of the gearbox is established to detect gearbox faults passively under non-steady operations (e.g., in wind turbine systems). The feature extraction is facilitated through the usage of harmonic wavelet transform and statistical analysis, and enhanced by incorporating the tachometer readings and gear meshing relationships to develop a speed profile masking technique. In another effort, building upon the Lamb wave based ultrasonic wave approach for structural damage detection, a computationally efficient adaptive harmonic wavelet transform is employed, together with principal component analysis and Hotelling  $T^2$  analysis, to elucidate the wave propagation change upon damage occurrence under measurement noise and uncertainty. Analytical, numerical and experimental investigations have been conducted to demonstrate the effectiveness and efficiency of the proposed methodology.

A wireless sensing platform is developed, with hardware prototyping and software programming for microphone signal collection/transmission, to demonstrate on-board processing and wireless transmission capabilities. A fundamental hurdle against the wide usage of wireless sensing which presumably is inexpensive and allows dense sensor distribution is the power supply to the

wireless sensors. Meanwhile, the ultimate goal of health monitoring and maintenance is to elongate the service life of structures/machineries under adversities such as vibration-induced fatigue/damage. The other research thrust of this dissertation research thus is to develop a new electro-mechanical tailoring scheme using piezoelectric transducers and periodically-arranged circuitry elements to manipulate wave/energy flow. It is identified that, upon proper circuitry tuning, we can create a variety of frequency bands that correspond to different wave/energy propagation patterns, to benefit either vibration-based energy harvesting (to be used in wireless sensing) or vibration isolation (to mitigate high cycle fatigue under tonal vibrations).

The components of this dissertation work have laid down a foundation for robust and autonomous damage detection and health monitoring of machineries (e.g., wind turbine gearbox) and structural elements (e.g., wind turbine blades), as well as for self-powering wireless sensors and for concurrent monitoring and vibration control through electro-mechanical tailoring. Together, these components will contribute to the eventual goal of developing sustainable mechanical systems.

**Towards Autonomous and Robust Damage Detection and Health  
Monitoring of Mechanical Systems**

Yi Lu

B.E., Tsinghua University, 2005

A Dissertation

Submitted in Partial Fulfillment of the

Requirements for the Degree of

Doctor of Philosophy

at the

University of Connecticut

2011

UMI Number: 3504782

All rights reserved

INFORMATION TO ALL USERS

The quality of this reproduction is dependent upon the quality of the copy submitted.

In the unlikely event that the author did not send a complete manuscript and there are missing pages, these will be noted. Also, if material had to be removed, a note will indicate the deletion.



UMI 3504782

Copyright 2012 by ProQuest LLC.

All rights reserved. This edition of the work is protected against unauthorized copying under Title 17, United States Code.



ProQuest LLC  
789 East Eisenhower Parkway  
P.O. Box 1346  
Ann Arbor, MI 48106-1346

**APPROVAL PAGE**

Doctor of Philosophy Dissertation

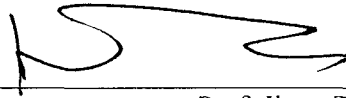
**Towards Autonomous and Robust Damage Detection and Health**

**Monitoring of Mechanical Systems**

Presented by

Yi Lu, B.E.

Major Advisor



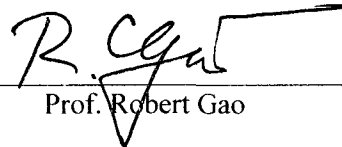
Prof. Jiong Tang

Associate Advisor



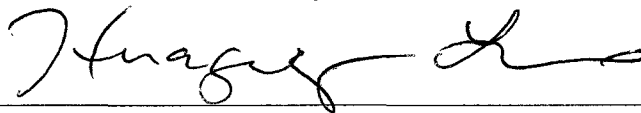
Prof. Richard Christenson

Associate Advisor



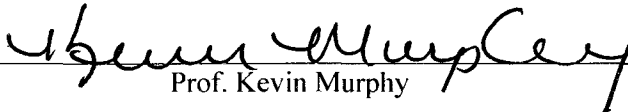
Prof. Robert Gao

Associate Advisor



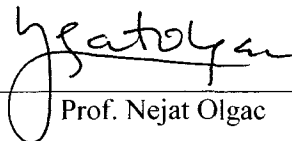
Dr. Huageng Luo

Associate Advisor



Prof. Kevin Murphy

Associate Advisor



Prof. Nejat Olgac

## ACKNOWLEDGEMENTS

I would like to acknowledge the help of many people during my doctoral studies. Foremost, I would like to express my gratitude to my advisor Prof. Jiong Tang for providing me with the opportunity to complete my graduate study at the University of Connecticut. This dissertation would not have been possible without the support and guidance of Prof. Tang. I have been amazingly fortunate to have an advisor who gave me the freedom to explore on my own, and in the meantime the guidance to recover when my steps faltered. His patience, motivation, enthusiasm, and immense knowledge make him a great mentor.

I would also like to thank Prof. Richard Christenson, Prof. Robert Gao, Dr. Huageng Luo, Prof. Kevin Murphy and Prof. Nejat Olgac, for serving on my advisory committee. Their insightful comments and constructive criticisms on many aspects of my research are invaluable.

Also, I am grateful to former and current colleagues in the Structure and System Dynamics Laboratory: Xingjie Fang, Xingjian Xue, Xin Wang, Ji Zhao, Dong Yang, Wei Dong, Kai Zhou, Edward Diehl, and Qi Shuai. Their generous sharing of knowledge and their friendship have been extremely important to me.

Special thanks to Wuming Zhang, Shaopeng Liu, Richard Fu and Max Villa, who helped me stay sane through these difficult years.

I am also thankful to the staff in the Mechanical Engineering Department for their various forms of support -- Thomas J. Mealy, Igor Parsadanov, George L. Assard II, Jacqueline Veronese, Laurie Hockla, Emily Jerome and Kelly Tyler.

Most importantly, none of this would have been possible without the love and patience of my family. My fiancée Ying Le has been a constant source of love, concern, support and strength all these years. My parents, Hongnian Lu and Jingchun Li, receive my deepest gratitude for their encouragement, understanding and continuous support.

Finally, I appreciate the financial support from National Science Foundation that funded parts of the research discussed in this dissertation.

## TABLE OF CONTENTS

Chapter 1. Introduction and Research Overview .....	1
Chapter 2. Health Monitoring of Rotating Machinery Using Multi-Sensor Signals and Feature Level Data Fusion .....	7
2.1 Gearbox dynamics experimental setup .....	10
2.2 Harmonic wavelet based signal representation .....	13
2.3 Feature highlighting using speed profile masking .....	15
2.4 Feature level multi-sensor data fusion .....	18
2.5 Case studies and discussion .....	21
2.6 Concluding remarks .....	25
Chapter 3. Lamb Wave Based Structural Damage Detection Using Piezoelectric Transducers and Robust Time-Frequency Analysis .....	27
3.1 Research overview .....	31
3.2 Robust signal processing and decision making.....	32
3.3 Parametric analysis and case studies.....	43
3.4 Concluding remarks .....	52
Chapter 4. Wireless Sensing Platform for Distributed Signal Processing and Decision Making .....	53
4.1 Hardware and software development of the wireless sensing platform.....	55
4.2 Test results .....	60
4.3 Concluding remarks .....	64
Chapter 5. Electro-mechanical Tailoring of Structures Through Periodically Coupled Piezoelectric Circuitry .....	66
5.1 Mono-coupled periodic circuitry .....	70



5.2	Baseline analysis of host structure without periodic circuitry .....	73
5.3	Electro-mechanical periodic system .....	76
5.4	Discussions and case studies.....	85
5.5	Concluding remarks .....	93
Chapter 6.	Conclusions and Future Work.....	95
Bibliography	.....	98

## TABLE OF FIGURES

Figure 1. Gearbox dynamics testbed with multiple sensors.....	11
Figure 2. Typical time domain sensor signals (unit: volt). (a) Accelerator #1; (b) Accelerator #2; (c) Microphone #1 (d) Microphone #2 (e) Tachometer.....	12
Figure 3. (a) A typical vibration signals collected from an accelerometer and its time-frequency representations using (b) the harmonic wavelet, (c) Daubechies 4 wavelet and (d) Morlet wavelet, respectively.....	14
Figure 4. A tachometer signal and the motor speed contour converted.....	15
Figure 5. a) Speed profile mask constructed from the tachometer signal. Solid contours correspond to the gear pair between input and intermediate shafts, while dotted contours correspond to the gear pair between intermediate and output shafts. b) Time-frequency features highlighted using the constructed speed profile mask. ....	16
Figure 6. Typical wavelet maps generated from (a) accelerometer #1 and (b) microphone #1, compared with (c) the fused wavelet map for all sensors.....	18
Figure 7. (a) Normally distributed random noise simulating the signal from a failed accelerometer. (b) Wavelet features extracted from the signal and highlighted using the speed profile masking as if the sensor is normal.....	20
Figure 8. Wavelet features fused from multiple sensors, including the failed accelerometer, using (a) simple averaging and (b) the PCA based method.....	21
Figure 9. Fault diagnosis process based on statistical analysis of baseline library and test features .....	23
Figure 10. T scores calculated using wavelet features from the healthy gearbox.....	24
Figure 11. T scores calculated using wavelet features from a faulty gearbox: eccentricity.....	24
Figure 12. T scores calculated using wavelet features from a faulty gearbox: surface wear.....	25
Figure 13. Side and top view of the experimental set-up (dimensions in mm).....	32
Figure 14. Discrete-time adaptive harmonic wavelet transform implemented using FFT/IFFT (N=16).....	35
Figure 15. Comparing AHWT with Daubechies 4 wavelet transforms.....	36
Figure 16. Procedure of the robust and quantitative decision making (N=16, L=5, K=3). ....	42
Figure 17. Damage detection demonstration. (Notch width $w=0.8\text{mm}$ and depth $h/2d=33.3\%$ ) ..	43

Figure 18. Detection sensitivity versus signal-to-noise ratio. (Notch width $w=0.8\text{mm}$ and depth $h/2d=33.3\%$ ) .....	45
Figure 19. Detection sensitivity versus truncation threshold. (Notch width $w=0.8\text{mm}$ and depth $h/2d=33.3\%$ ) .....	47
Figure 20. Detection sensitivity versus center frequencies of the excitation signal. (Notch width $w=0.8\text{mm}$ and depth $h/2d=33.3\%$ ).....	47
Figure 21. Equivalent set-ups for generating (a) mixed modes, (b) pure S0 mode and (c) pure A0 mode Lamb waves. The same equity holds for the sensor signals (d), (e) and (f). .....	48
Figure 22. Detection using pure A0 or pure S0 mode Lamb waves excited at (a) 50 kHz, (b) 90 kHz, (b) 115 kHz and (d) 130 kHz. (Notch width $w=0.8\text{mm}$ and depth $h/2d=33.3\%$ ) .....	49
Figure 23. Detection sensitivity versus (a) notch depth (when $w=0.8\text{mm}$ is fixed) and (b) notch width (when $h/2d=33.3\%$ is fixed).....	51
Figure 24. Microphone circuit on the Imote2 wireless node. ....	55
Figure 25. Hardware and software block diagram.....	57
Figure 26. The prototype platform and the testing system. A segment of data received by the local Imote2 transmitted via SPI port. ....	59
Figure 27. (a) A segment of data received by the remote Imote2 via wireless transmission. (b) Another segment with discontinuities.....	61
Figure 28. A segment of data (a) collected from one microphone and its frequency content (b)..	61
Figure 29. A segment of data collected from the 4-member microphone array using an ADS1278 evaluation board.....	64
Figure 30. Mono-coupled periodic circuitry. ....	69
Figure 31. One propagation constant versus nondimensionalized frequency for the mono-coupled periodic circuitry.....	72
Figure 32. (a) A bare beam structure virtually divided into identical elements. (b) Beam elements and their state vectors.....	73
Figure 33. Two propagation constants (solid line and dotted line) versus nondimensionalized frequency for the bare beam structure.....	75
Figure 34. Tri-coupled electro-mechanical periodic system with a piezoelectric circuitry coupled onto the beam structure. ....	76
Figure 35. (a) Three propagation constants (solid line, dotted line and dashed line) versus nondimensionalized frequency for the electro-mechanical periodic system. (b) Two propagation	

constants (solid line and dotted line) for a separate beam structure, and one propagation constant (dashed line) for a separate periodic circuitry..... 81

Figure 36. An electro-mechanical periodic system with two piezoelectric circuitries coupled onto the beam structure ..... 83

Figure 37. Three real part of the propagation constants (solid line, dotted line and dashed line) versus nondimensionalized frequency.  $C_c = 1.68\mu\text{F}$  and  $L = 0.0063\text{H}$ . ..... 85

Figure 38. (a) A 10-segment electro-mechanical system excited by a harmonic force.  $C_c = 1.68\mu\text{F}$  and  $L = 0.0063\text{H}$ . Vertical displacement  $w_i$  along the beam length direction (solid line) compared to that of the bare beam without the PZT circuitry (dotted line). The excitation frequency is (b) within and (c) out of the “all-attenuation zone”..... 87

Figure 39. (a) 20-segment electro-mechanical system excited by a harmonic force.  $C_c = 1.68\mu\text{F}$  and  $L = 0.0063\text{H}$ . Vertical displacement  $w_i$  along the length direction when the excitation frequency is (b) within or (c) out of the “all-attenuation zone”..... 88

Figure 40. (a) 20-segment electro-mechanical system excited by a harmonic force.  $C_c = 1.68\mu\text{F}$  and  $L = 0.0063\text{H}$ . Vertical displacement  $w_i$  along the length direction when the excitation frequency is (b) within or (c) out of the “all-attenuation zone”..... 89

Figure 41. Electric charge in each circuit as shown in Figure 38, when the excitation frequency is (a) within or (b) out of the “all-attenuation zone”. ..... 90

Figure 42. Three propagation constants (solid line, dotted line and dashed line) versus nondimensionalized frequency when (a)  $r_c = 8$  or (b)  $r_c = 25$ . The inductance  $L$  has been chosen to fix  $r_L = 1$  ..... 93

Figure 43. Three propagation constants (solid line, dotted line and dashed line) versus nondimensionalized frequency when (a)  $r_L = 0.8$  or (b)  $r_L = 1.2$ .  $r_c$  has been fixed at  $r_c = 20$  ..... 93

## Chapter 1. Introduction and Research Overview

Qualitative and non-continuous monitoring, diagnosis and prognosis of mechanical systems can be traced back to the early 19th century, when railroad wheel-tappers used the sound of a hammer striking the train wheel to evaluate if damage was present. Also, for decades, engineers have been using vibration analysis to evaluate performance of rotating machinery. However, accuracy of such empirical techniques depends highly on human interpretation. In the last ten to fifteen years, as microelectronics and information technologies evolve drastically, innovative monitoring and diagnosis systems have emerged. Although visual inspections are still needed in certain cases, vibration, acoustic, wave propagation and other sensor signals become viable inputs for structural health monitoring and damage detection. An **autonomous** methodology means that detection, diagnosis and prognosis of mechanical damages/defects/faults can be achieved with no or little human intervention. The data-driven approach becomes a natural choice. Data or signals can be collected by small yet sensitive sensors and then processed through signal processing and decision making algorithms. Current condition of the monitored mechanical system can thus be evaluated by comparing signal features from the on-line measurements with those from a baseline library. Hardware wise, such an autonomous methodology requires a self-contained platform with on-board actuators, sensors, power supply and other supporting circuits. Software wise, the key is to extract signal *features* that can characterize faults or damages. To make the process **robust** against operational and environmental variances, additional improvements are required. For example, signal noises should not only be treated in the time domain but also in the feature domain, so that representative features can be highlighted. Obviously, utilizing features from multiple channels (sensors) or multiple collections may also enhance the robustness. An autonomous and robust system for structural health monitoring and fault detection is particularly valuable for mechanical systems located in remote areas. Wind turbines are a good example.

Major components where faults or damages may occur include, but are not limited to, the gearbox and blades.

Active and passive approaches have both been explored in various damaged detection and health monitoring applications. Lamb wave based structural damage detection is a typical example of an active approach. Lamb waves are elastic guided waves propagating in solid plate (or layer) with free boundaries. Studies (Lin and Yuan 2001b; Lin and Yuan 2001a; Giurgutiu 2005; Raghavan and Cesnik 2005) have shown that their propagation patterns are sensitive to local damages in the structure. To excite Lamb waves in the test structure, an actuator should be employed to apply surface tractions in a specific form. In this dissertation research, piezoelectric patches are used as the actuator as well as the sensor. Piezoelectric materials, e.g., lead zirconate titanate (PZT), exhibit the direct piezoelectric effect (the internal generation of electrical charge resulting from an applied mechanical force) and the reverse piezoelectric effect (the internal generation of a mechanical strain resulting from an applied electrical field). When a specific voltage input is applied to one PZT patch attached on the structure, Lamb waves can be excited. Similarly, the wave propagation in the structure can cause strain change on another PZT patch, which in return generates an electric signal as a sensor. On rotating machinery, however, signals are often collected passively. The operational vibration of the test machine provides sufficient excitation for the signal to be collected, so other external excitations may not be necessary. In such a passive approach, the focus is to fully utilize that vibration source and collect signals from different positions or time periods.

Various types of signals may be collected and used but in real world, they are inevitably contaminated by environmental and operational noises. Signal processing is thus a critical part of structural damage detection and health monitoring (Staszewski 2002). For example, to reduce noise, averaging multiple collections (Raghavan and Cesnik 2005) or adopting some filtering techniques (Yu and Giurgutiu 2005) are common in practice. Both discrete and continuous

wavelet transform have recently been studied for denoising. Another aspect of signal processing is feature extraction and representation. The Fourier transform, though most widely used, provides only the global frequency information averaged over the entire time span. To preserve time information in the signal, the wavelet analysis was developed to map a signal into time and frequency domain. Each wavelet coefficients represents how well the input signal correlates with a windowed basis function called wavelet. For different applications a variety of wavelets have been adopted, e.g., Haar, Daubechies, Mexican Hat, Gabor and Morlet wavelets. Generally speaking, wavelet analysis is capable of extracting time-frequency features from complex signals (Daubechies 1992). Choosing a specific wavelet oftentimes remains empirical in specific engineering applications. In this dissertation research, a computationally efficient wavelet transform is adopted, which has been demonstrated to generate better representation of vibration, acoustic and wave propagation signals in the time-frequency domain.

Multiple sensors are often deployed for the purpose of information redundancy in various applications, especially when individual sensor's performance may be compromised under certain constraints. Thus, the autonomous and robust methodology requires the information contained in *multiple* data collections to be *fused* together before diagnosis. For example, accelerometers, acoustic sensors and tachometers are used in my gearbox condition monitoring application. While each sensor covers one aspect/area/parameter of the overall running condition, multi-sensor data fusion techniques are employed to take full use of the redundant information. Simple averaging appears to be a straightforward way to fuse data. However, noise may easily spread out from one data set into multiple data sets and thus affect the fusion results. So an advanced data fusion technique is necessary to take into account statistical properties of the multiple data sets.

The ultimate goal of signal processing techniques is to enhance the decision making performance in the diagnosis stage. To quantify the severity of a fault, damage or defect, numerical indices are calculated using the extracted features. Some scalar indices adopted include (Tseng and Naidu

2002) root-mean-square deviation (RMSD), mean absolute percentage deviation (MAPD), covariance (Cov) and correlation coefficient (CC). For multiple signals data sets, advanced statistical methods and vector indices become a natural choice. For example, principal component analysis (PCA) combined with Hotelling's  $T^2$  analysis can be used for feature highlighting and decision making (Ganesan et al. 2004). PCA is an orthogonal linear transformation that projects data onto a new coordinate system in such a way that the largest variance lies on the first coordinate (first principal component), the second greatest variance on the second coordinate, and so on. A direct application of PCA is denoising, by truncation of the principal components with major eigenvalues. The highlighted features after PCA can then be compared to other signals using Hotelling's  $T^2$  statistic, based on which statistical decision making can be achieved.

In some cases such as on a legacy system, the sensors for data acquisition are preferred to be deployed in a more convenient manner with no or less wiring. Then we may choose wireless technologies. Wireless nodes can provide flexibility and re-configurability in sensor deployment; meanwhile, on-board computational capability enables local signal processing. Examples of utilizing wireless sensors for damage detection in various systems have become abundant recently, e.g., Lynch and his team (Lynch et al. 2004; Lynch et al. 2006) exploited the merits of wireless sensing on civil structures. Requiring little or no human intervention, wireless sensors in general may reduce the overall maintenance costs of mechanical systems. However, compared to the conventional wired scheme, wireless sensors do pose new challenges due to its power constraints. For example, energy consuming IC chips may not be selected in the circuit design, nor do some signal processing algorithms with high computational costs. Balance between performance and resources have to be considered carefully at all time.

Indeed, energy is the key for any wireless implementation. With a sustainable power supply, a mechanical system can be monitoring continuously using my autonomous and robust algorithms on the wireless setup. The question is if we can take advantage of the existing configuration and



find a way to satisfy the energy demand. Recall that piezoelectric transducers enable electro-mechanical interaction between the mechanical structure and the electrical circuits, which essentially provides conversions of mechanical energy into electrical energy and vice versa. That said, a spatially connected piezoelectric circuitry has great potential to be used not only directly as an energy harvester to collect mechanical energy but also reversely as a tailoring tool to prevent excessive vibration. An electro-mechanical periodic system that is capable of manipulating energy propagation is proposed in Chapter 5.

In this dissertation research, three major tasks are covered:

- Health monitoring of machineries using vibration, acoustic and rotation speed sensors
- Lamb wave based damage detection on structural systems using piezoelectric transducers
- Electro-mechanical tailoring of structure through coupled piezoelectric circuitry

Common challenges from the first 2 tasks include feature extraction, feature highlighting/denoising, and statistical decision making. To extract characteristic features from vibration, acoustic or wave propagation signals, I develop an adaptive harmonic wavelet transform (AHWT) based method in the time-frequency domain. A principal component analysis (PCA) based feature highlighting technique is also adopted for Lamb wave features. As for rotating machinery, to deal with the non-stationary operating conditions, I propose to make full use of both the online measurements from the sensors and the fundamental characteristics of the system dynamics. Features from multiple sources are then fused together in a statistical manner. The final evaluation of the current system condition can thus be conducted quantitatively using statistical scalar or vector indices calculated from those extracted, highlighted and fused features. The effectiveness and efficiency of the proposed methodology is investigated using numerical simulations and lab experiments. Also, a wireless sensory platform has been developed to further evaluate the implementation of the developed algorithms and the issues associated with them. In task 3, an original design of an electro-mechanical periodic system is presented. With the help of

piezoelectric transducers and electrical circuitry attached onto the mechanical structure, the vibration energy can be manipulated by tuning electrical parameters. Analytical modeling and numerical simulations demonstrate that potential applications of such a design include not only vibration energy harvesting to power wireless sensors but also isolation of tonal vibration with varying frequency content.

## **Chapter 2. Health Monitoring of Rotating Machinery Using Multi-Sensor Signals and Feature Level Data Fusion**

As introduced in Chapter 1, both active and passive approaches can be used for structural damage detection and health monitoring. For rotating machinery, since its operation generally provides a constant vibration source, passive approach is often chosen in this case. Engineers have used vibration based analysis for decades to evaluate the condition of complex rotating machinery. Other sensor signals can be collected for this purpose too. However, there are many challenges for example, faults occur primarily at the materials level but their effects can only be observed indirectly at a system level. Another problem is the many-to-many relationship between faults and the observable quantities. The accuracy of the empirical techniques may be significantly subject to human interpretation. In recent years, along with the rapid advancements of microelectronics and information technologies, innovative monitoring and diagnosis systems have emerged. Although visual inspections are still needed in certain situation, vibration and acoustic emission signals have become main inputs in many cases. Those signals can be easily obtained by employing small yet sensitive sensors of different types. Even when individual sensor's performance may be compromised due to cost or energy constraints, multiple sensors can be deployed for information redundancy. Utilizing signal processing algorithms, an intelligent monitoring scheme can enable the implementation of a condition-based maintenance (CBM) philosophy (Jardine et al. 2006).

To make the condition monitoring and fault diagnosis autonomous, signal processing is the critical factor, especially when raw data are collected in a noisy observing environment (Staszewski 2002). It is well known that the vibrations and acoustic emissions produced by rotating machinery contain important diagnostic and prognostic information about the condition of the gears. The key is to extract fault-sensitive features from those signals and perform

statistical analysis of the features for decision making. The Fourier transform as a widely used signal representation method provides only the global frequency information averaged over the entire time span, which means the time information is lost during the transformation. To preserve the time information as well as the frequency information, wavelet analysis has been utilized to transform a signal into the joint time-frequency domain (Daubechies 1992). Each wavelet coefficients represents how well the input signal correlates with a windowed basis function called wavelet. For different applications, a variety of wavelets have been adopted, including, e.g., Haar, Daubechies, Mexican Hat, Gabor and Morlet wavelets. Choosing a wavelet for a specific system/application, however, is not straightforward. Several previous studies (Yan and Gao 2010; Wan et al. 2004; Lu et al. 2008) have shown that the harmonic wavelet is particularly suitable for analyzing vibration and acoustic signals.

Data-driven gearbox fault diagnosis is not only about choosing a transform to extract time-frequency features from the data. An even more important step is to make full use of the fundamental physics of the gearbox and highlight those fault-sensitive features. Each wavelet coefficient can be interpreted as the energy concentration at a specific time-frequency point, but not every wavelet coefficient is equally valuable for fault diagnosis. In gearbox systems, it is known that there are certain frequencies are more sensitive to certain fault conditions (Girdhar and Scheffer 2004). For example, gear mesh frequency and its multiples may be sensitive to gear faults, while shaft rotational speed may be sensitive to gear or bearing faults. Also, it is easy to understand that a gear with a missing tooth may show a different noise pattern than a gear with eccentricity. By incorporating the fundamental understanding of gearbox dynamics into signal analysis, it is possible to highlight time-frequency features that are of physical meanings for fault diagnosis.

In a multi-sensor setup, data fusion can improve the ability to detect, characterize, and eventually identify fault conditions. Despite extensive research on mechanical models, pattern recognition,

neural network, and other signal processing techniques for individual sensor, relatively less research has been conducted on fusion of multi-sensor data for condition monitoring (Hall and McMullen 2004). The sensor-level data fusion is mainly raw data alignment, denoising, normalization, and resampling, etc. Techniques such as frequency banding and time-domain averaging are commonly adopted at this lowest level to ensure data quality and provide sensor self-check. Other examples can be found in (Byington et al. 2008). When features are extracted from the raw data, through wavelet analysis for example, it becomes feature-level data fusion. Next, determining the health condition of the monitored system based on the fused features involves decision-level data fusion. There are statistical, voting or neural network based algorithms developed at this level (Liggins, Hall, and Llinas 2009), where decisions are weighted, blended and quantified as indicators of fault existence.

In what follows, I outline a fault detection methodology for wind turbine gearboxes using multiple sensors. In this data-driven framework, time domain vibration and acoustic emission signals collected from a gearbox first undergo the harmonic wavelet transform which allows me to analyze the response characteristics under non-stationary operating condition. The reason I choose harmonic wavelet is that the wavelet map reveals how the frequency components of the signal vary in terms of time, since neighbor wavelet levels have no interference with each other. Such wavelet is also computational efficient, which leads to additional advantage for implementation in embedded systems. An important advancement of this proposed methodology is the integration of the tachometer signal as well as gear meshing relationships into the analysis. A tachometer provides online measurement of the shaft rotational speed, which can be depicted as a time-frequency contour. From the shaft speed contour, I can further calculate several other time-frequency contours corresponding to gear/bearing characteristics. These time-frequency contours form the speed profile mask, which identifies fault-sensitive components on a wavelet map. By applying this speed profile mask, I can achieve feature highlighting by retaining only

those characteristic wavelet coefficients in the time-frequency domain. The data fusion will then be carried out at the feature level. In a gearbox system, features extracted respectively from accelerometers, microphones and tachometer measurement may cover one aspect/area/property of the overall condition. When combined, these features can obviously provide a more comprehensive characterization of the condition or reduce the size of the critical feature subspace for easier decision-making. Mathematically, in this framework these features are fused together through a statistical weighting approach based on principal component analysis. Utilizing all above, my goal is to achieve a condition-based maintenance (CBM) philosophy through the proposed autonomous and robust monitoring scheme. By autonomous I mean little of no human intervention/interpretation is needed in the process, while by robust I mean the fault can be detected/identified/located even with the presence of environmental or operational variations. Data analyses based on experimental investigations on a gearbox testbed are carried out to demonstrate the effectiveness of the proposed methodology in detecting faulty conditions. My results also show that different feature patterns can be extracted for different gear faults, which can be used for further identification and classification.

## **2.1 Gearbox dynamics experimental setup**

Gearbox is typical rotating machinery that serves as a major dynamic component in many mechanical systems. There are often multiple pairs of meshing gears in each gearbox mounted on rotating shafts, while the shafts themselves require bearings and fixtures to be installed. Many types of mechanical faults and failures can occur in a gearbox, for example, surface wear, misalignment, eccentric or crack gears. Vibration and acoustic sensor signals collected from such a system may reveal partial information about its running operating condition.

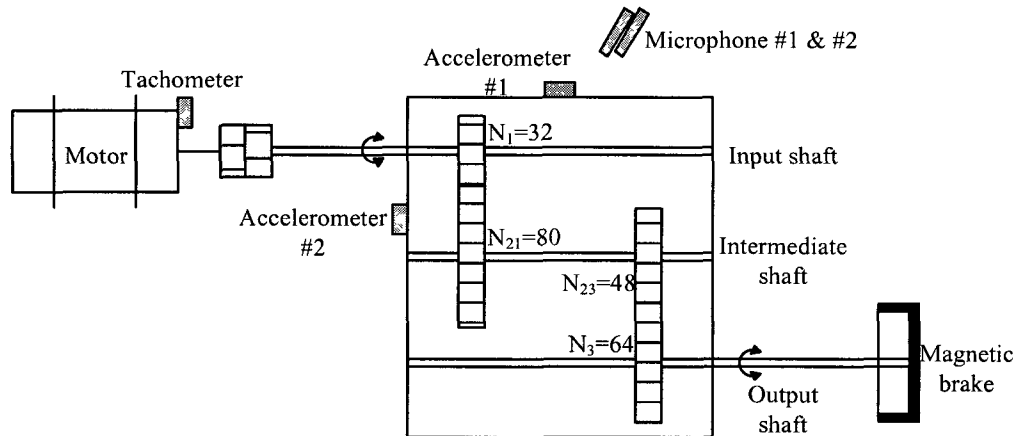
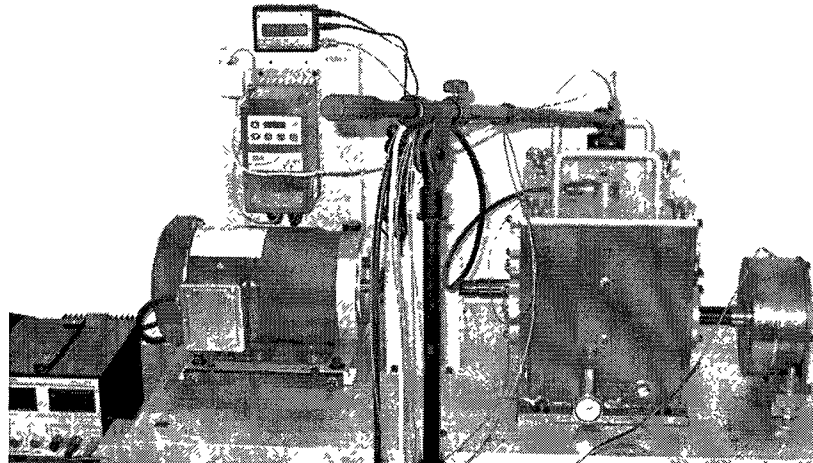


**Figure 1. Gearbox dynamics testbed with multiple sensors.**

To obtain real-time operating information of a gearbox with or without faults, I use a gearbox dynamics simulator manufactured by SpectraQuest Inc (Richmond, VA). It consists of a 3 HP motor controlled via USB by a software package on PC, a gearbox with 3 shafts and 2 pairs of meshing gears, and a voltage controlled magnetic brake. According to the configuration shown in Figure 1, we can see that the two-stage gearbox is a speed reducer, in which the input speed is first reduced to its 40% and then reduced to its 30%. A built-in tachometer measures the rotational speed of the input shaft. In addition, I use two accelerometers (Model 355B03, PCB Piezotronics Inc., Depew, NY) and two microphones (Model 130E20, PCB Piezotronics Inc.,

Depew, NY) to record the vibration and acoustic signals. All the sensor readings are converted into digital signals and recorded onto PC through a dSPACE system (DS1006 processor board, dSPACE Inc., Wixom, MI) with DS2004 high speed A/D board. Gears in this gearbox testbed are replaceable. A healthy or faulty gear ( $N_1 = 32$ ) can be installed on the input shaft. For faulty cases, I have one gear with a missing tooth, one gear with eccentricity ( $e = 0.1$ ), one gear with surface wear, and one gear with a cracked tooth. First, the healthy gear is installed and sensor signals are collected multiple times. Each collection consists of time-domain signals from the 2 accelerometers, 2 microphones and 1 tachometer. Multiple collections are used to build a baseline library for the healthy case. Then, a faulty gear is installed. The same data acquisition procedure is run to collect signals for the faulty case.

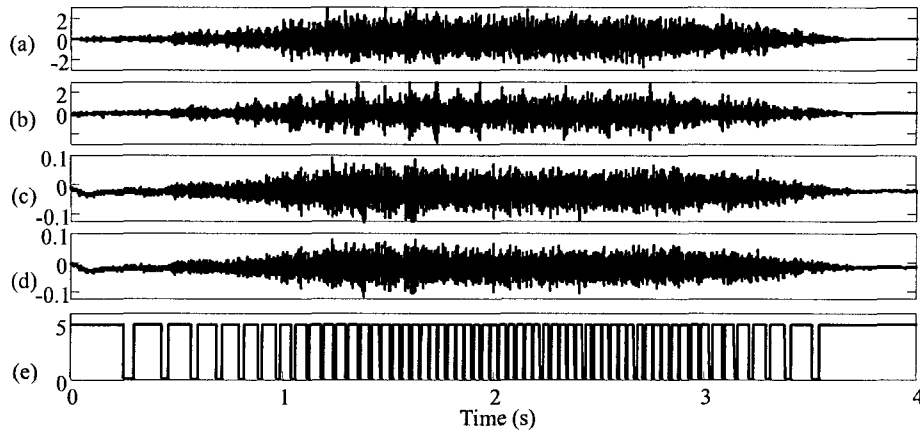


**Figure 2. Typical time domain sensor signals (unit: volt). (a) Accelerator #1; (b) Accelerator #2; (c) Microphone #1 (d) Microphone #2 (e) Tachometer.**

To emulate the non-stationary operation conditions in wind turbines, I create a speed profile in the driver controller software. Starting from zero speed, the motor first accelerates to 1500 rpm within 2 sec, remains that speed for 1 sec, and then decelerates to zero within 1 sec. This speed profile may mimic a testing process from start-up to shut-down. A typical signal collected from the accelerometer is shown in Figure 2 together with its frequency spectrum. Since the signals are



non-stationary, the frequency spikes on the spectrum do not necessarily correspond to harmonics. A time-frequency domain method is thus needed for feature representation.

## 2.2 Harmonic wavelet based signal representation

One challenge for wind turbine gearbox condition monitoring comes from the non-stationary nature of its operation. A direct consequence is that harmonic based method like Fourier transform cannot be used effectively. Instead, time-frequency methods such as wavelet analysis become a natural choice (Wang and McFadden 1995). A number of recent studies (Yan and Gao 2010; Lu et al. 2008) have shown that harmonic wavelet developed by Newland (Newland 1993; Newland 1994) is effective and efficient in analyzing vibration related signals. Harmonic wavelet transform combines the advantages of the short-time Fourier transform and the continuous wavelet transform. Signal analysis can thus be restricted to specific wavelet levels (frequency bands) with straightforward physical interpretations. The family of generalized harmonic wavelets can be express as

$$w_{mnk}(t) = \frac{\exp\left[in2\pi\left(t - \frac{k}{n-m}\right)\right] - \exp\left[im2\pi\left(t - \frac{k}{n-m}\right)\right]}{(n-m)i2\pi t} \quad (1)$$

where  $m$  and  $n$  are the level parameters,  $0 \leq m < n$ , and the integer  $k$  denotes the translation parameter within the level  $(m, n)$ . Harmonic wavelets are compact and complete in the frequency domain. Each wavelet level  $(m, n)$  covers the frequency range  $(m2\pi, n2\pi)$  so that it forms an ideal bandpass filter with its Fourier transform as

$$W_{mnk}(\omega) = \begin{cases} \frac{1}{(n-m)2\pi} e^{-i\omega \frac{k}{n-m}} & \text{for } m2\pi \leq \omega \leq n2\pi \\ 0 & \text{otherwise} \end{cases} \quad (2)$$

We can see that it is a square window function, i.e., constant in a certain octave band and zero elsewhere. Harmonic wavelet transform combines the advantages of the short-time Fourier

transform and the continuous wavelet transform. Signal analysis can thus be restricted to specific frequency bands with known physical meanings. This partially explains why harmonic wavelet has been chosen for many vibration based applications (Yan and Gao 2010, Wan et al 2004). Another advantage of harmonic wavelets is that the coefficients can be calculated through a FFT/IFFT based algorithm (Lu et al 2008). It is well known that FFT is an extremely efficient, compact and well-developed algorithm. Unlike other wavelets that using filtering/convolution based algorithms, harmonic wavelet coefficients can be calculated with minimum computational cost if the levels are preset. This can benefit its implementation to embedded system with wireless platform (Lu and Tang 2009).

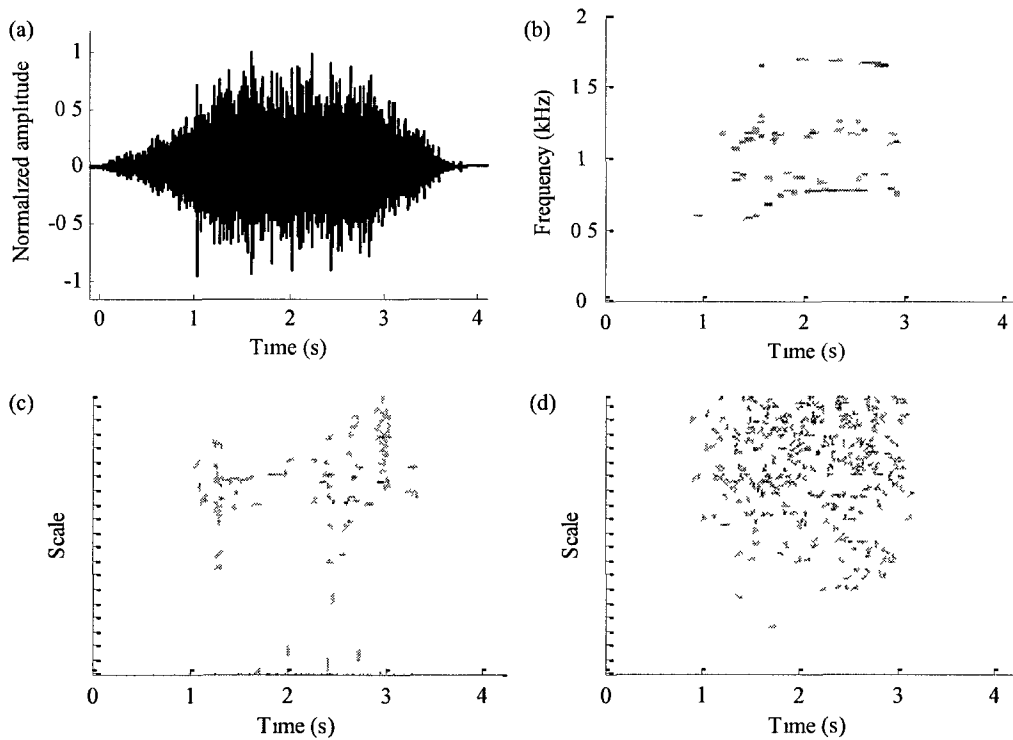


**Figure 3. (a) A typical vibration signals collected from an accelerometer and its time-frequency representations using (b) the harmonic wavelet, (c) Daubechies 4 wavelet and (d) Morlet wavelet, respectively**

Figure 3 (b) shows the harmonic wavelet map of a typical acceleration signal recorded from the aforementioned gearbox testbed. The value of each wavelet coefficient on the map indicates

energy concentrated on that specific frequency component at that specific time instant. Dark color indicates large value, while light color indicates small value. Comparing the wavelet maps in Figure 3 calculated using different wavelets, only on the harmonic wavelet map we can recognize a pattern resembling the designed motor speed profile accelerating for the first 2 seconds, remaining steady for the third second, and decelerating for the last second. Since the vertical axis corresponds to frequency, we can further identify that specific profile around 500-800 Hz, which matches exactly the gear mesh frequency of the gear pair on the input and intermediate shafts. In contrast, Daubechies 4 wavelet vaguely reveals the signal's time-varying nature, while the Morlet wavelet hardly captures any meaningful pattern. Both Daubechies 4 and Morlet wavelet maps are plotted using MATLAB's wavelet toolbox, none of which can reveal features with clear physical meanings.

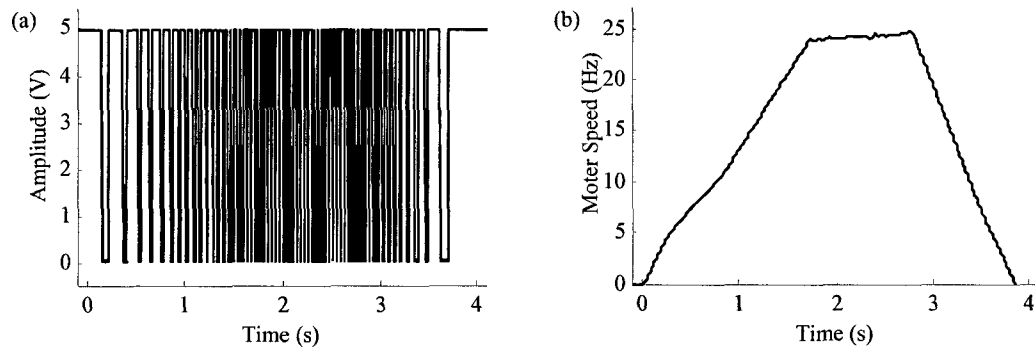


**Figure 4. A tachometer signal and the motor speed contour converted.**

### 2.3 Feature highlighting using speed profile masking

While the harmonic wavelet map could lead to physically meaningful interpretations of the acceleration signal analyzed as shown in Figure 3, it is still difficult to draw direct correlation with respect to the operating condition of the gearbox based on such map only. This is especially true for wind turbine gearboxes having constantly changing frequency components in its vibration/acoustic responses. In order to further highlight the meaningful time-frequency features out of the above wavelet map, here in this research I propose to incorporate the operating

condition of the gearbox into the analysis. Specifically, the online measurements from the tachometer as well as the gear meshing relationship are utilized.

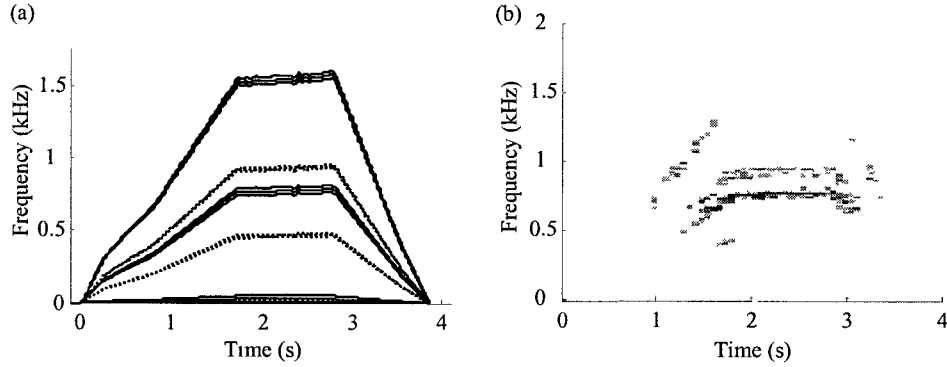


**Figure 5. a) Speed profile mask constructed from the tachometer signal. Solid contours correspond to the gear pair between input and intermediate shafts, while dotted contours correspond to the gear pair between intermediate and output shafts. b) Time-frequency features highlighted using the constructed speed profile mask.**

As mentioned, there are two pairs of gears mounted in the gearbox testbed analyzed in this research. One pair connects the input and intermediate shafts, and the other pair connects the intermediate and output shaft. Figure 4 shows a segment of signal from the tachometer mounted on the input shaft. The speed profile can be easily converted into Hz. From the gear mesh relationship, I can then derive the rotational speed of each shaft and the gears on it. The gear mesh frequency is defined as the product of the shaft speed and the tooth number, i.e.,

$$GMF = v_{gear} \times N_{gear} = v_{pinion} \times N_{pinion} \quad (3)$$

where  $v_{gear}$  ( $v_{pinion}$ ) is the gear (pinion) rotational speed in Hz and  $N_{gear}$  ( $N_{pinion}$ ) is the gear (pinion) tooth number. Also, since the tooth number of each gear is known, we can calculate rotational speeds of other shafts if we know the speed of the input shaft. In general, rotating machineries have been studied extensively in the past, to gain insights on the vibratory characteristics and the failure modes. It has been demonstrated that certain frequency components are of high value for fault diagnosis (Girdhar and Scheffer 2004). If the operating condition is stationary, it is possible to use empirical experience to identify gearbox faults based

on the frequency spectrum of measured signals. To name a few, the shaft speed and its multiples, as well as the gear mesh frequency and its multiples sidebanded by the shaft speed, are all of high interest.

To deal with the non-stationary operating conditions, in this research I propose to make full use of both the online measurements from the sensors and the fundamental characteristics of the gearbox dynamics. Recall that the tachometer provides online measurements of the shaft rotation speed. I can thus calculate gear mesh frequencies and other characteristic frequency at any given time. Furthermore, I can construct a mask to identify the critical time-frequency contours on the harmonic wavelet map. Figure 5 (a) shows a constructed mask, where solid contours correspond to the critical time-frequency components for the first gear pair between the input and intermediate shafts, whereas the dotted contours correspond to the second gear pair between the intermediate and output shafts. Here I include 1x and 2x shaft frequencies, as well as 1x and 2x gear mesh frequencies sidebanded by 1x shaft frequency. In practice, we also need, for example, 2% relaxation to account for various uncertainties. On the constructed mask, each point along a contour indicates the characteristic time-frequency component that is valuable to us. To apply the mask onto the harmonic wavelet map, I keep those wavelet coefficients that overlap with any contour in the time-frequency domain while deleting those with no such overlapping. It is a unique property of the harmonic wavelet analysis: each wavelet coefficient corresponds to an exact frequency range at a time instant. Figure 6 (b) shows the masking result on the same wavelet map without those deleted coefficients. Compared to the wavelet map prior to the masking as shown in Figure 3, we can see that most characteristics have been extracted while the stationary noise or unrelated frequency components, such as those caused by the cooling fan, are thrown away.

It is worth mentioning that, for different kinds of faults, the constructed speed profile mask may be different. For example, we only need the shaft speed and its multiples for shaft faults or

journal bearing faults. For ball bearing faults, we may need to include certain sidebands determined by ball bearing dimensions. In gearboxes with multiple shafts and meshing gear pairs, if we are only interested in some of them, we can build a speed profile mask just including some time-frequency contours instead of all the above.

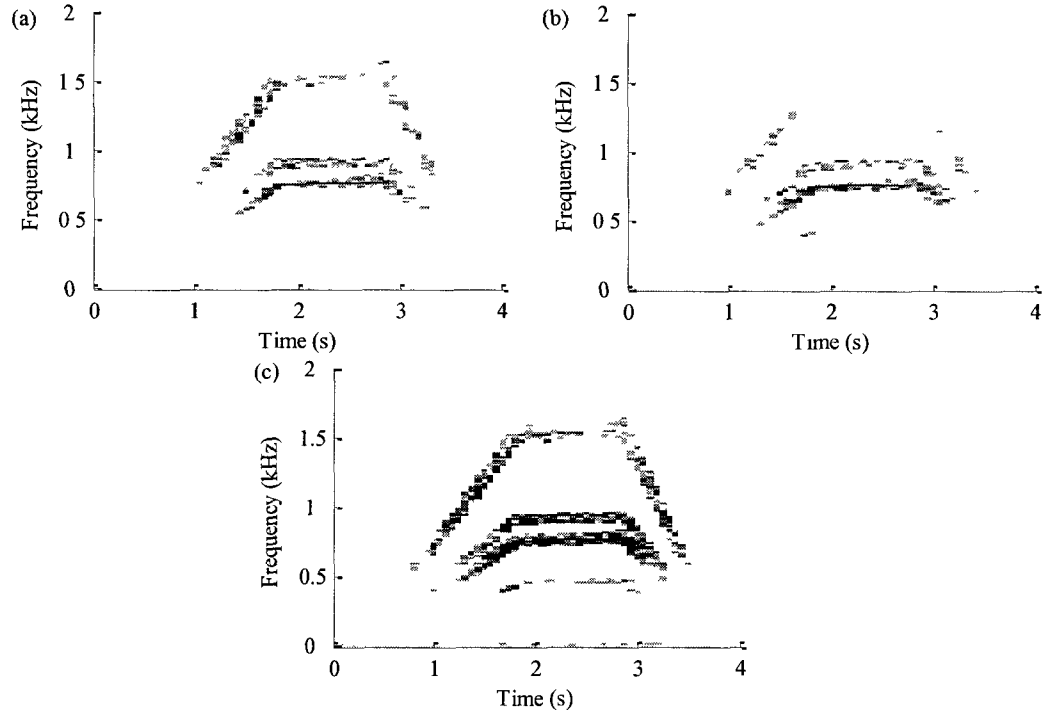


**Figure 6. Typical wavelet maps generated from (a) accelerometer #1 and (b) microphone #1, compared with (c) the fused wavelet map for all sensors.**

#### 2.4 Feature level multi-sensor data fusion

Through the above procedure, each recorded time series can generate an array of time-frequency features. Thus, every time a collection of multi-sensor signals will generate multiple arrays of features simultaneously. For the aforementioned experimental setup, I have 4 sensor signals (2 from accelerometer and 2 from microphones) and thus 4 arrays of features in total. To enhance performance using the enriched information, I need to fuse these features together effectively and efficiently.

Instead of simply averaging the features, here I use a statistical method based on the principal component analysis (PCA). PCA is a multivariate statistical procedure that transforms a number of correlated variables into a smaller number of uncorrelated new variables called the principal components (Jackson 2003). The first principal component accounts for as much of the variation in the data as possible, and each succeeding component explains as much of the remaining variability as possible. To be exact, the first principal component is along the direction with the maximum variance, and the second component is constrained to lie in the subspace perpendicular to the first component. Within the subspace, the second component points to the direction of maximum variance. And the third component is taken in the maximum variance direction in the subspace perpendicular to the first two, and so on. Suppose we have a  $K \times L$  matrix  $\mathbf{X}$  indicating  $K$  arrays of features, where each array has  $L$  elements. We can find its eigenvector matrix  $\mathbf{V} = [\mathbf{v}_1 \ \mathbf{v}_2 \ \cdots \ \mathbf{v}_K]$  and its eigenvalue matrix  $\mathbf{D} = \text{diag}(\lambda_1, \lambda_2, \dots, \lambda_K)$ . Without loss of generality, we assume the eigenvalues are in a descending order. Then the first eigenvector is called the first principal component. The fusion weights can thus be defined using the first principal component  $\mathbf{v}_1$ . The fused array of features is

$$\mathbf{x}_{\text{fused}} = \sum w_i \mathbf{x}_i \quad (4)$$

where the normalized fusion weights are, e.g.,  $w_i = \frac{\mathbf{v}_1(t)}{\sum \mathbf{v}_1(t)}$ . In this way, each fusion weights is

determined by the variance (information) contained in the corresponding feature array  $\mathbf{x}_i$ . This PCA based fusion method was originally used for image processing (Naidu and Raol 2008) with excellent performance. It can also be applied block by block, when a smaller segment size may enhance fusion performance. I adopt this method here partially because the wavelet maps are essentially images plotted in the time-frequency domain. Figure 6 shows the wavelet maps extracted from individual sensors as well as the fused wavelet map using the above PCA based

method. In Figure 6 (c), we can see that meaningful features are highlighted and fused into one single wavelet map.

Compared with simple averaging, such PCA-based data fusion can deal with sensor errors or failures. I can use an extreme case to illustrate. Suppose one accelerometer in the aforementioned testbed failed, its sensor readings are random noise in the time domain as shown in Figure 7 (a). If the signal is processed as if the sensor is normal, then after wavelet feature extraction and speed profile masking, the highlighted features can be shown as in Figure 7 (b). Compared with Figure 6 (a), we can see that Figure 7 (b) includes dark spots all over the wavelet map, which represent the random nature of the original sensor signal. If the features from the multiple sensors are fused through simple averaging, then the errors shown in Figure 7 (b) will spread out over all other wavelet maps and the fusion result will look like Figure 8 (a). Gearbox faults can hardly be detected because useful information is covered up by noise and errors. In contrast, if the PCA based method is used, the weight will be automatically reduced for the signal from the failed accelerometer. Comparing the fusion result shown in Figure 8 (b) with Figure 6 (c), we can see that the wavelet map is lighter in color but have a similar pattern as before. Thus, faults may still be detected using the fused features.

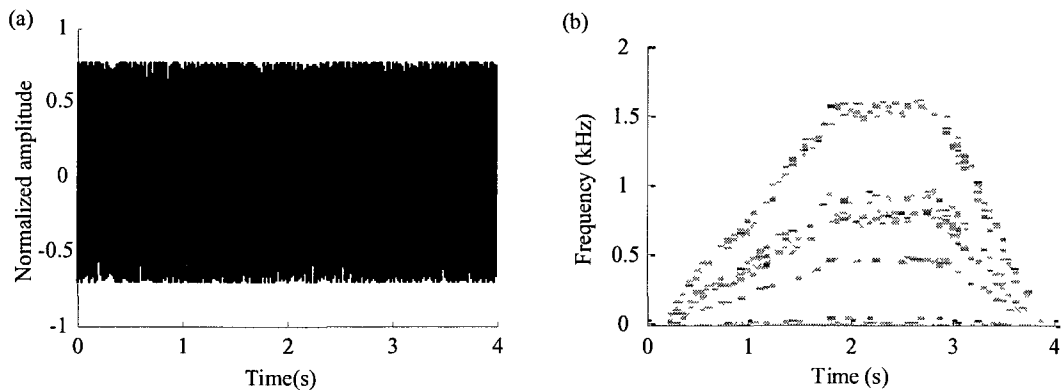


**Figure 7. (a) Normally distributed random noise simulating the signal from a failed accelerometer. (b) Wavelet features extracted from the signal and highlighted using the speed profile masking as if the sensor is normal.**



## 2.5 Case studies and discussion

We can construct a baseline library using feature vectors extracted, highlighted and fused from the known healthy gearbox. In my experimental setup, a healthy gear is then be replaced by a faulty one. From this gearbox under test, a new collection of signals gives another feature vector after the same signal processing procedure. It is worth mentioning here that in the beginning I need to align all the signals in the time domain as there is no guarantee that they are perfectly synchronized. It is a common practice to use the Generalized Cross Correlation with Phase Transform (GCC-PHAT) as presented by (Knapp and Carter 1976) and (Brandstein and Silverman 1997). Given two time series  $y_1(n)$  and  $y_2(n)$  the GCC-PHAT is defined as

$$\hat{G}_{PHAT}(f) = \frac{Y_1(f)Y_2^*(f)}{|Y_1(f)Y_2^*(f)|} \quad (5)$$

where  $Y_1(f)$  and  $Y_2(f)$  are the Fourier transforms of the two signals and \* denotes the complex conjugate. The time delay for these two inputs is estimated as

$$\hat{d}_{PHAT} = \arg \max_d \hat{R}_{PHAT}(d) \quad (6)$$

where  $\hat{R}_{PHAT}(d)$  is the inverse Fourier transform of  $\hat{G}_{PHAT}(f)$ . Harmonic wavelet features are then extracted from the shifted signal using the above mentioned method.

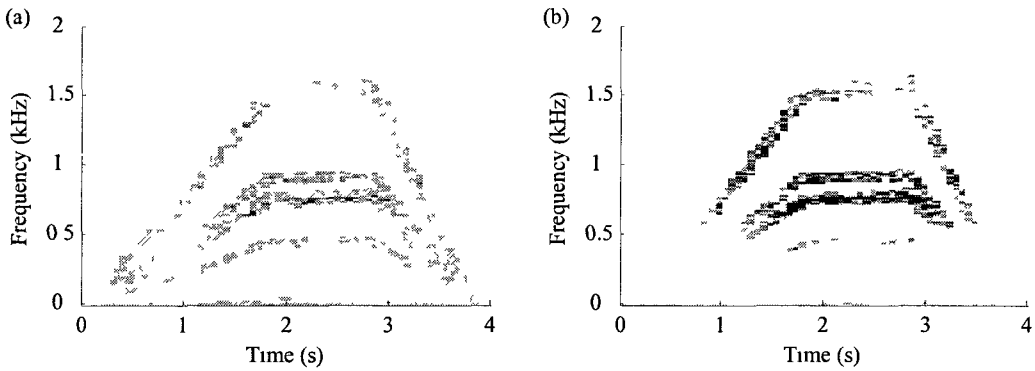


**Figure 8. Wavelet features fused from multiple sensors, including the failed accelerometer, using (a) simple averaging and (b) the PCA based method.**

The gearbox condition is examined by comparing the new feature vector with the baseline library as illustrated in Figure 9. Statistically speaking, the more different they are, the more likely the gearbox under test is faulty. To quantify the difference, generally one may calculate a statistical index by comparing features from a gearbox under test with those from the healthy baseline. Common scalar indices (Tseng and Naidu 2002) include root-mean-square deviation (RMSD), mean absolute percentage deviation (MAPD), covariance (Cov) and correlation coefficient (CC). In order to demonstrate the effectiveness of my proposed signal processing methodology, here I choose a straightforward statistical indicator, the  $T$  score.

In statistics, the  $T$  score measures how many sample standard deviations an observation is above or below the sample mean. In this case, each wavelet feature on the time-frequency domain can be treated as a random variable. Suppose we have  $R$  runs of data collections and thus  $R$  feature vectors in the baseline library. Then, for each random variable there are  $R$  samples (observations), for example,  $x_1, \dots, x_R$ . Let  $\bar{x} = (x_1 + \dots + x_R) / R$  be the sample mean and

$s = \sqrt{\frac{1}{R-1} \sum_{i=1}^R (x_i - \bar{x})^2}$  be the sample standard deviation, then for a new sample  $x$  from the

gearbox under test, the  $T$  score is defined as

$$T = \frac{x - \bar{x}}{s / \sqrt{R}} \quad (7)$$

For each random variable (wavelet coefficient) in the time-frequency domain, we can calculate a corresponding  $T$  score from the highlighted and fused wavelet features. In the following discussion, all the  $T$  scores are absolute values. The larger the  $T$  score is, the more significantly is the test feature different from the baseline. In other words, we will have more confidence to claim the gearbox under test is faulty if the calculated  $T$  score is large. It is worth mentioning that here the  $T$  score is defined without the assumption of normality. The values calculated using the highlighted and fused wavelet features generally do not follow the Student's t-

distribution because normal distribution in the feature space cannot be guaranteed. However, the role of the  $T$  score as a statistical indicator is not affected.

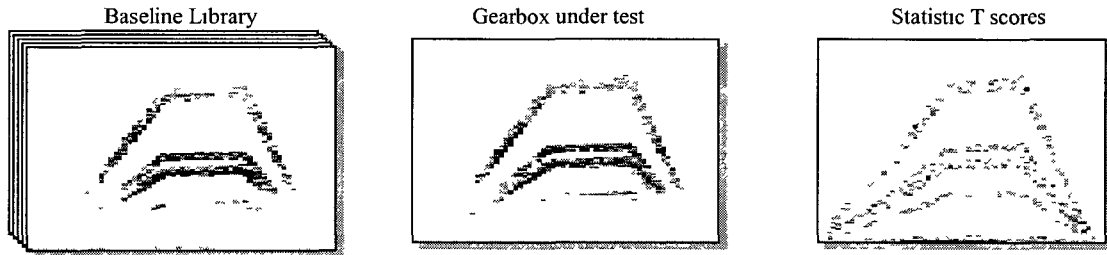


**Figure 9. Fault diagnosis process based on statistical analysis of baseline library and test features**

#### 2.5.1. Baseline self-checking

I first collect a new set of signals from the same healthy gearbox that has been used to build the baseline library. In this case, the calculated  $T$  scores should indicate a healthy condition pattern. To better present these results, I plot the absolute  $T$  scores onto the wavelet map so that the implied statistical difference can be pinpointed onto each specific time-frequency spot. Light colors represent small  $T$  scores while dark colors represent large  $T$  scores. Figure 10 shows the calculated  $T$  scores plotted onto the time-frequency map. We can see almost all  $T$  scores are smaller than 5 (mid-range), meaning the test features are statistically not different from the baseline. Thus, no major gear fault is detected in this case, confirming the baseline library has been constructed correctly.

#### 2.5.2. Faulty condition I: gear with eccentricity

I replace the healthy gear on the input shaft by an eccentric gear, which is a standard test sample provided by the testbed manufacturer (SpectraQuest Inc., Richmond, VA). Time domain signals from multiple sensors are collected following the same procedure as before. They are processed the same way as for the baseline. Using the new set of wavelet features along with the baseline library, I calculate the new  $T$  scores and mark them onto the time-frequency map as shown in

Figure 11. Compared with Figure 10, we can see there are many  $T$  scores larger than 8 (black spots), indicating significant difference from baseline and thus faulty condition. Recall the speed profile mask shown in Figure 5. We find those large  $T$  scores only appear along the contours corresponding to the first meshing gear pair (between the input and the intermediate shafts). Therefore, gear fault is not only detected (by large  $T$  scores) but also located (via the corresponding contours) as within the first meshing gear pair.

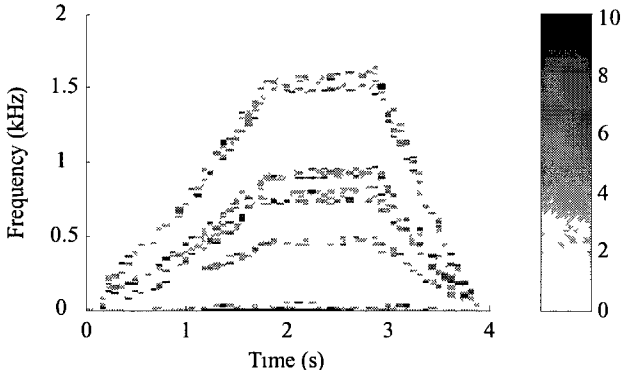


Figure 10.  $T$  scores calculated using wavelet features from the healthy gearbox.

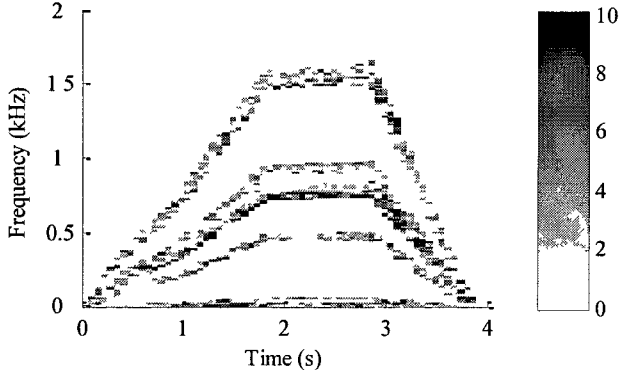
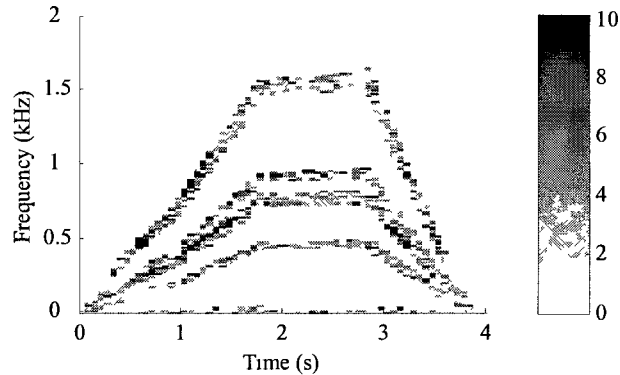


Figure 11.  $T$  scores calculated using wavelet features from a faulty gearbox: eccentricity.

2.5.3. Faulty condition II: gear with surface wear

I then replace the healthy gear on the input shaft by a gear with surface wear, which is another standard test sample provided by the testbed manufacturer. Following the same procedure as above, I have the  $T$  scores calculated and marked onto the time-frequency maps as shown in

Figure 12. This time large  $T$  scores (dark spots) appear also along the contours corresponding to the first meshing gear pair. Again, gear fault is not only detected but also located using the proposed methodology. The color pattern shown in Figure 12 is different from that in Figure 11. For example, the darkest area in Figure 12 appears between 0.5 s and 1.2 s, with frequency ranging from 0.5 kHz to 0.9 kHz. In contrast, the darkest area in Figure 11 appears between 2.9 s and 3.5 s, with frequency ranging from 0.8 kHz to 0.4 kHz. Since the only difference between the two cases is the fault type, I can conclude that the different color patterns represent different fault types. With advanced pattern recognition techniques, I may further identify fault types by building a library of fault patterns.



**Figure 12. T scores calculated using wavelet features from a faulty gearbox: surface wear.**

## 2.6 Concluding remarks

In this chapter I present a data-driven fault detection framework suitable for gearboxes that constantly operate under varying speeds such as those used in wind turbines, employing time-frequency feature extracted, highlighted and fused from multiple sensors. First, raw data are collected from my gearbox dynamics testbed, on which either a healthy or a faulty gear can be installed to simulate different faulty cases. A motor speed profile with time-varying rotation is designed to account for the non-stationary operation condition. To deal with the non-stationary nature of the collected time domain signals, I use a harmonic wavelet based method to extract

time-frequency features effectively and efficiently. Then a speed profile masking technique is developed to make full use of sensor data and physical understanding of the gearbox dynamics. Time-frequency wavelet features are highlighted by the mask constructed using tachometer readings and gear meshing relationships. After that, features from multiple sensors are fused through a statistical weighting approach based on principal component analysis. Finally a simple statistical indicator is employed to demonstrate the effectiveness of the proposed fault detection scheme. Using experimental data collected from the gearbox testbed, different gear faults can not only be detected but also be located to a certain gear pair.

### **Chapter 3. Lamb Wave Based Structural Damage Detection Using Piezoelectric Transducers and Robust Time-Frequency Analysis**

In the preceding chapter, I discuss a passive approach of monitoring current condition of rotating machinery using vibration and acoustic signals. In this chapter, I present an active approach to detect damages and defects of a structure in a quantitative and robust manner. Lamb waves, which are elastic guided waves propagating in solid plate (or layer) with free boundaries, have been well studied and widely used in damage detection (Rose 2004). Lamb waves can be excited in a structure by an actuator, e.g., piezoelectric transducer. When there is a damage or defect along the wave propagation path, the content and pattern of the waves will change accordingly. We can collect these wave patterns using sensors and detect the damage or defect through various signal processing techniques. In recent years, a large amount of research on the modeling and analysis has been carried out to understand the properties of Lamb waves excited by piezoelectric transducers (Lin and Yuan 2001b; Lin and Yuan 2001a; Giurgutiu 2005; Raghavan and Cesnik 2005). In general, Lamb waves are more sensitive to the presence of local damages than the global response of a structure; thus the Lamb wave techniques could provide more useful information than vibration based techniques (Kessler and Dunn 2003) in certain cases. This promising advantage provides possibilities of in situ damage detection in various applications.

Excitation and propagation of Lamb waves are affected by several parameters such as excitation center frequency, excitation wave form and sensor size, which introduce practical complexity to Lamb wave based applications. Often times, multiple wave modes are excited at given frequency. To investigate and eventually optimize the detection performance, researchers have built various mathematical models to analyze the wave modes. For each mode, there is one dispersion curve relating its phase/group velocity with respect to the excitation frequency. Giurgutiu *et al.* (Giurgutiu et al. 2002) first suggested the use of “sweet spot” frequency. At that frequency, the

amplitude ratio of the excited  $S_0$  mode (lowest symmetric wave mode) over the  $A_0$  mode (the lowest antisymmetric wave mode) reaches its maximum. They claimed such selection can minimize the inherent interference between different Lamb wave modes and thus lead to easier sensor signal interpretation. Wang *et al* (Wang et al. 2008) drew a similar conclusion through analytical modeling and numerical simulation. However, the validity of the “sweet spot” frequency should be tested by quantitative detection performance. After all, we should select parameters that can indeed lead to satisfactory detection results under implementation conditions with variations and uncertainty.

Based on the information given by the Lamb wave propagation, previous researchers have developed a variety of damage detection or identification schemes to determine the status of a structure. One straightforward thought is to compare the time domain signals collected from undamaged and damaged structures. To quantify the degree by which the signals differ from each other, a number of damage indices have been proposed (Tseng and Naidu 2002), e.g., root-mean-square deviation (RMSD), mean absolute percentage deviation (MAPD), covariance (Cov) and correlation coefficient (CC). Most of these indices are scalars which average the difference over the time period; thus some time information has to be sacrificed. To take advantage of both the amplitude and the time information, the use of time-of-flight (TOF) has been suggested, which measures the traveling time of a wave packet from the actuator to the sensor. Some identification methodologies depend more or less on the time-of-flight concept. For example, Lin and Yuan (Lin and Yuan 2001b; Lin and Yuan 2001a) presented a damage identification scheme using a migration technique which treats the damage as a secondary source and the detected reflection waves are back-propagated towards the damage. Giurgiutiu et al (Giurgiutiu 2005; Giurgiutiu 2003) explored using the weighted sum of the wave-propagation signals in different directions collected by a sensor array. However, since the signals are often contaminated with noise, in certain cases the time-of-flight may not be measured accurately enough to determine the



damage location. Moreover, due to the complexity of multi-mode Lamb wave propagation, blind zones may exist, where extra caution and effort is needed (Tua et al. 2004).

In many applications, the timely detection of the occurrence of damage is of primary concern, especially in the presence of environmental uncertainties which make the identification of damage location/severity difficult. The environmental and operational variances (e.g., ground vibration or electrical disturbances) result in noisy and complex sensor data. Since any 'robust' decision making scheme requires proper handling of noise, the importance of signal processing has gradually been emphasized (Staszewski 2002). To reduce the noise effect, it is common to collect multiple signals from the same structure under the same condition. One straightforward and widely used signal processing method is to directly average multiple signals (Raghavan and Cesnik 2005), but such method does not take full usage of the information from the statistical point of view. Recently, denoising by using either discrete or continuous wavelet transform has also been studied, which leads to signal processing techniques in feature domains other than the time domain. Here arises the issue of feature extraction and representation. The Fourier transform, though most widely used (Cawley and Adams 1979), provides only the global frequency information over the entire time span but loses all the time information in the signal. To overcome this drawback, short time Fourier transform (STFT) was developed to map a signal into a two-dimensional function of time and frequency. STFT adopts a windowing technique, but the resolution depends on the size of the window, according to the uncertainty principle: a small window leads to fine time resolution but coarse frequency resolution, while a large window has the opposite effect. Wavelet analysis is another joint time-frequency domain technique, which can be treated as a short-time Fourier transform with variable-sized windows. It is essentially a correlation-based method that yields coefficients representing how well the input signal correlates with a series of windowed functions which are the wavelet basis. Kim and Melhem (Kim and Melhem 2004) reviewed recent studies on damage detection using wavelet analysis and put them

into three categories: (1) variation of wavelet coefficients; (2) local perturbation of wavelet coefficients; and (3) reflective wave caused by local damage. The detectability (capability of detecting damage) thus relies on the degree by which the waveform signal of a test structure differs from that of an undamaged structure. A variety of mother wavelets have been used, including Haar wavelet (Wang et al. 1999), Daubechies wavelets (Hou et al. 2000), Mexican hat wavelet (Lu and Hsu 2002), Gabor wavelet (Quek et al 2001), and Morlet wavelet (Park et al. 2006), etc

Using wavelet analysis for feature extraction, I can transform each time series collected into one array of wavelet coefficients. In the presence of environmental and operational variances, multiple signals are collected from the undamaged structure; thus a matrix instead of only one vector of wavelet coefficients will be obtained as the baseline data set. Although it is possible to use the aforementioned damage indices, the complexity due to multiple baseline signals may affect the accuracy or even the feasibility. Indeed, statistical techniques appear to be a natural choice. The research issue here is actually similar to that in process monitoring, where multivariate data are collected from different processes and used to determine abnormal operation conditions. Ganesan et al (Ganesan et al. 2004) performed a thorough literature review on wavelet-based multiscale statistical techniques in the field of process monitoring, where it was pointed out that the principal component analysis (PCA) combined with Hotelling's  $T^2$  analysis could be very useful for monitoring. PCA is an orthogonal linear transformation that projects data onto a new coordinate system such that the largest variance lies on the first coordinate (first principal component), the second greatest variance on the second coordinate, and so on. In some applications, the obtained wavelet features are compressed and denoised by the truncation of the principal components with the corresponding eigenvalues below a certain threshold. The PCA is usually followed by a decision making procedure based on the Hotelling's  $T^2$ , which is a statistic for a multivariate test of differences between the mean values of two data groups. In damage

detection studies, the  $T^2$  statistic not only can quantitatively detect a damage with a given confidence level, but also can help eliminate outliers from the set of baseline signals (Fang and Tang 2006).

### **3.1 Research overview**

Although significant amount of research has been carried out on Lamb wave based damage detection using piezoelectric transducers, there are still unsolved issues regarding detection decision-making algorithms. In particular, to date, the feature extraction and quantitative prediction of damage in the presence of environmental uncertainties remain as a challenging problem. Existing methods are either built upon the accurate analysis of wave propagation that might not be measured easily under noisy condition, or using overly-simplified threshold value that is rigid and overlooks the abundant information carried by the wave propagation signals. In this research, a combination of signal analysis tools will be studied to specifically address the issue of robust damage detection using piezoelectric transducers and the Lamb wave propagation. The damage detection is carried out by comparing the multiple time series (baseline signals) measured a priori from the undamaged structure with one test signal collected from the test beam (damaged or undamaged). In order to identify the critical features embedded in the baseline signals, I adopt the adaptive harmonic wavelet transform to analyze the wave propagation characteristics. This adaptive harmonic wavelet transform allows me to use the smallest number of wavelet coefficients (referred to as the baseline data set) to characterize the multiple signals in the joint time-frequency domain. Following that, the principal component analysis is applied to the wavelet coefficients for feature highlighting and denoising. During the detection process, the test signal will undergo the same data processing; thus a vector of wavelet coefficients of the test signal (the test data vector) is obtained. Finally, I use Hotelling's  $T^2$  analysis to analyze quantitatively the difference between the test data vector and the baseline data set, where the

decision making is achieved upon a given confidence-level. With this highly integrated procedure, human interference can be reduced so that the damage detection may become an automated process. Using this quantitative and robust decision-making procedure, I then investigate the influence of a variety of system parameters involved in the Lamb wave based damage detection using piezoelectric transducers. For example, it has been showed that the ‘sweet spot’ excitation center frequency concept that maximizes the amplitude ratio between the  $S_0$  and  $A_0$  mode waves. I can examine previous theoretical findings in actual damage detection applications with environmental and operational variances.

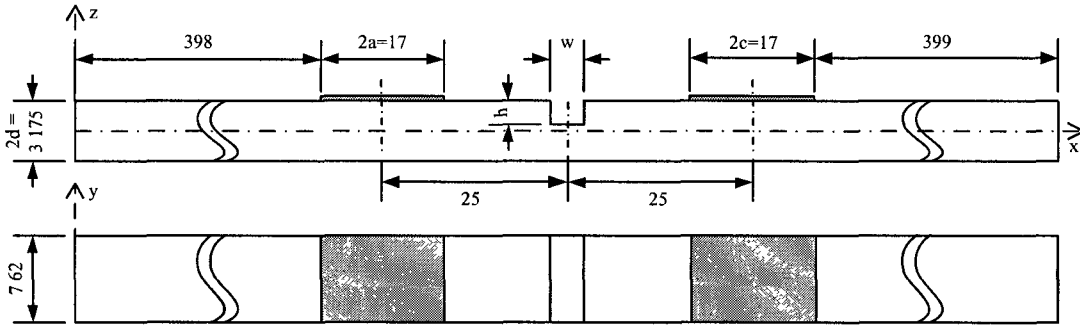


Figure 13. Side and top view of the experimental set-up (dimensions in mm)

### 3.2 Robust signal processing and decision making

As mentioned above, for signals like Lamb waves that contain non-stationary content, time-frequency analysis is preferred rather than frequency-only methods (Peng and Chu 2004). Among various time-frequency representations, wavelet analysis has the ability of multi-scale decomposition via dilation and translation; thus features in a signal can be extracted through wavelet basis. The advantage of wavelet transforms is the flexibility in using narrow windows for the analysis of high-frequency content and wide windows for low frequencies. Newland (Newland 1993; Newland 1994) developed the harmonic wavelet and its generalized form, whose wavelet levels represent non-overlapping frequency bands so that there is no interference term between any frequency components. It is preferable if the information contained in the original

signals can be isolated and concentrated in the wavelet domain, so that the decision about damage status could be made based on as few coefficients (i.e., features) as possible. Newland's harmonic wavelet transform offers great possibility for such analysis. In particular, here I adopt the adaptive harmonic wavelet transform (AHWT) proposed by Liu (Liu 2003) to analyze the baseline and test signals of Lamb waves propagation in the undamaged and test structures, respectively. With this as the basis for feature extraction, PCA and Hotelling's  $T^2$  analysis are employed to highlight the feature, remove the noise effect, and finally identify the response anomaly with given confidence level.

Let us consider aluminum beam structure in two states: undamaged and damaged. The experimental set-up in Figure 13 shows the damaged beam with single piezoelectric actuator and single sensor. In the damaged beam, a surface notch is introduced. The piezoelectric actuator is connected with a waveform generator while the sensor is connected with a digital oscilloscope. Since excitation signals with narrow bandwidth are preferred to reduce the dispersion of Lamb wave, we use sinusoidal waves under a Hann window as the transient excitation signal. It is expressed as

$$f(t) = \frac{1}{2} \sin(\omega_0 t) \left[ 1 - \cos\left(\frac{2\pi t}{T}\right) \right], \quad t < T \quad (8)$$

where  $\omega_0$  is the center frequency, and  $T$  is the duration of the excitation signal which is typically a multiple of the half period of the center frequency. Unless otherwise noted, in this dissertation research  $T$  is selected as ten times of the half period. As introduced in (Wang et al. 2008), Lamb wave modes can be categorized as symmetric and anti-symmetric based on the wave motions with respect to the median plane of the structure. In this case, I choose the center frequency lower than 160 kHz so that only the  $S_0$  mode (the lowest symmetric mode) and the  $A_0$  mode (the lowest anti-symmetric mode) can be excited.

### 3.2.1. Adaptive harmonic wavelet transform for multi-signal applications

As introduced in Chapter 2, harmonic wavelet transform is advantageous in processing vibration and wave propagation related system. Here the adaptive feature extraction technique is derived from harmonic wavelet. Recall that from the Fourier transform in the frequency domain

$$W_{mnk}(\omega) = \begin{cases} \frac{1}{(n-m)2\pi} e^{-i\omega \frac{k}{n-m}} & m2\pi \leq \omega \leq n2\pi \\ 0 & \text{otherwise} \end{cases} \quad (9)$$

Newland (1993, 1994) derived the family of generalized harmonic wavelets

$$w_{mnk}(t) = w_{mn}\left(t - \frac{k}{n-m}\right) = \frac{\exp\left[in2\pi\left(t - \frac{k}{n-m}\right)\right] - \exp\left[im2\pi\left(t - \frac{k}{n-m}\right)\right]}{(n-m)i2\pi t} \quad (10)$$

where  $m$  and  $n$  are the level parameters,  $0 \leq m < n$ , and integer  $k$  denotes the translation parameter within the level  $(m, n)$ . Notice that each level  $(m, n)$  corresponds to one wavelet function that covers the frequency range  $(m2\pi, n2\pi)$ . Harmonic wavelets are orthogonal so that a complete set of them could be called a wavelet basis. They are compact in the frequency domain, where each wavelet can be related to an ideal bandpass filter. The advantage is that the signal analysis is restricted to specific frequency bands with known physical meanings, and these bands are represented by the corresponding wavelet levels.

In Chapter 2, I briefly mentioned the discrete algorithm to obtain the coefficients by computing the inverse discrete Fourier transform (IFFT) of successive blocks (each corresponding to a  $(m, n)$  level) of the Fourier coefficients. Since the adaptive algorithm in the following paragraphs is its natural extension, I here present more details about the derivation of this wavelet transform. For a given Lamb wave response signal  $s(t)$  represented by the time series  $s(r)$ ,  $r = 0, 1, \dots, N-1$ , the corresponding complex wavelet coefficients can be obtained by computing

$$a_{mnk} = \sum_{l=0}^{n-m-1} F(m+l) \exp\left(\frac{i2\pi kl}{n-m}\right), \quad k = 0, 1, \dots, n-m-1 \quad (11)$$

where  $F(q)$ ,  $q = 0, 1, \dots, N-1$  are the Fourier coefficients calculated by discrete Fourier transform (or FFT)

$$F(q) = \frac{1}{N} \sum_{r=0}^{N-1} s(r) \exp\left(-\frac{i2\pi r q}{N}\right) \quad (12)$$

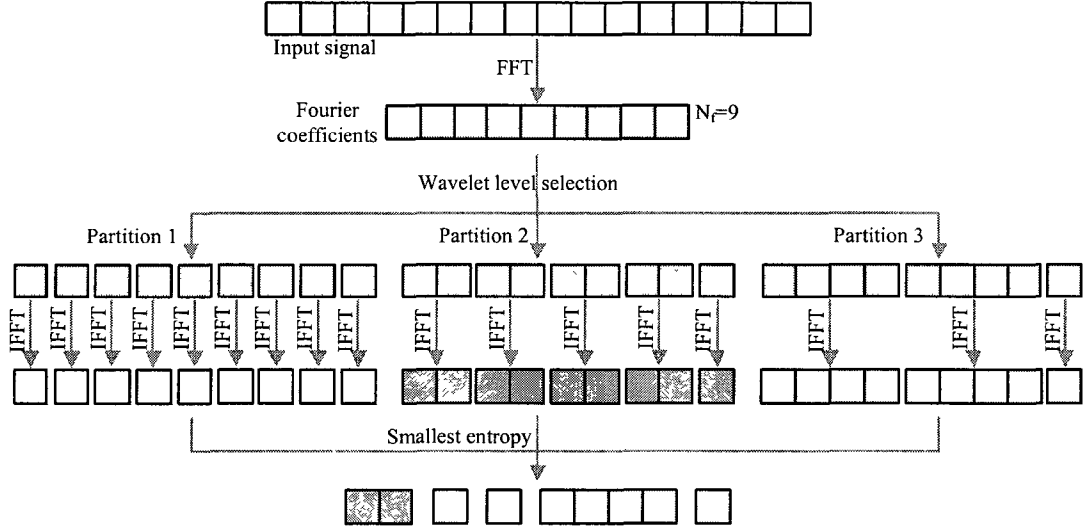


**Figure 14. Discrete-time adaptive harmonic wavelet transform implemented using FFT/IFFT (N=16)**

Moreover, in the discrete transform, each continuous wavelet function has to be replaced by a corresponding circular continuous function

$$w_{mnk}^{(c)}(r) = \frac{1}{(n-m)} \sum_{l=m}^{n-1} \exp\left(i2\pi l \left(\frac{r}{N} - \frac{k}{n-m}\right)\right) \quad (13)$$

Thus, the signal  $s(r)$  defined on the unit time interval can be expanded as

$$s(r) = \sum_{m,n} \sum_{k=m}^{n-1} \left\{ a_{mnk} w_{mnk}^{(c)}(r) + \bar{a}_{mnk} \bar{w}_{mnk}^{(c)}(r) \right\} \quad (14)$$

Each selection of level parameter pairs, e.g.,  $\{(m_0, n_0), (m_1, n_1), \dots, (m_{L-1}, n_{L-1})\}$ , must begin with a pair for which  $m_0 = 0$  and continue with touching (but not overlapping) pairs until  $n_{L-1} = N_f$ ,

where  $N_f$  corresponds to the Nyquist frequency and  $L$  denotes the number of levels (Newland 1993; Newland 1994).

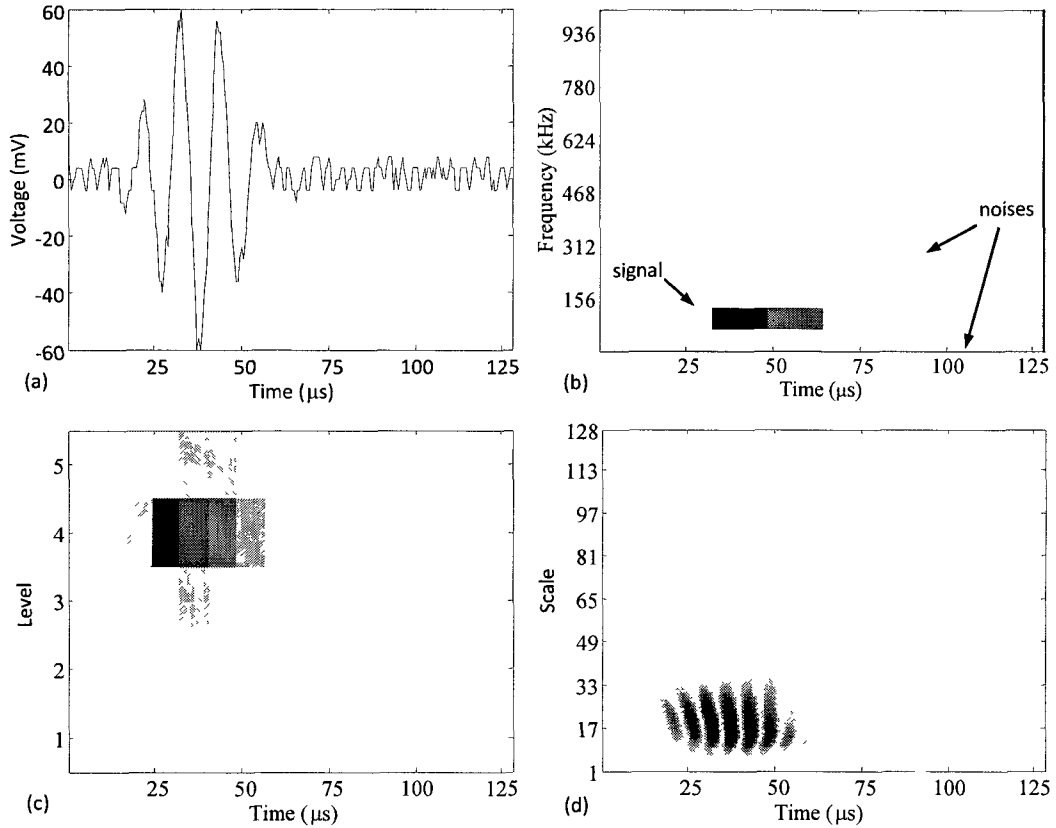


**Figure 15. Comparing AHWT with Daubechies 4 wavelet transforms.**

Liu (2003) treated each selection  $\{(m_0, n_0), (m_1, n_1), \dots, (m_{L-1}, n_{L-1})\}$  as a partition of  $\Omega = \{0, 1, \dots, N_f\}$  and adopted a Shannon entropy-based algorithm (Coifman and Wickerhauser 1992) to search a partition tree for the best partition (in the sense that the signal can be represented most sparsely). For any time series  $\mathbf{x} = \{x_j\}$ , the Shannon entropy is defined as

$$H(\mathbf{x}) = -\sum_j p_j \log p_j \quad (15)$$

where  $p_j = |x_j|^2 / \|\mathbf{x}\|^2$ , and  $p_j \log p_j$  is set to be 0 if  $p_j = 0$ . The entropy shown above is a measure of the sparsity, and therefore I expect smaller entropy for a better partition. The iteration



procedure for a sequence of 16 elements using a binary partition tree is illustrated in Figure 14. Since  $N_f = 9$  in this case, there are 9 Fourier coefficients left for the partition algorithm. For the initial partition, I consider each inverse Fourier coefficient as an initial subgroup, whose Shannon entropy is called the initial entropy. Here notice that each subgroup represents an aforementioned  $(m, n)$  pair corresponding to a wavelet. In the second partition, IFFT is applied to every two successive Fourier coefficients to form a subgroup, whose entropy is calculated and compared with the sum of corresponding initial entropies. As in the example shown in Figure 14, the sum entropy of the first two initial subgroups is smaller so that they are kept after the first selection. Through the entire iteration, the wavelet coefficients associated with the 'best' partition are computed. Meanwhile, the 'best' wavelet basis is generated by the same partition.

The advantages of the above-outlined adaptive harmonic wavelet transform (AHWT) over other wavelet transforms, like Daubechies 4, can be seen from the example illustrated in Figure 15. Figure 15(a) shows an experimental signal used as the input of the transforms to be compared. The signal is the waveform collected by the piezoelectric sensor from the aforementioned damaged beam with the center frequency at 90 kHz. Based on the information of the frequency contents, I could identify noise-related contents on the AHWT map, i.e., in Figure 15(b), the low frequency content around 0 kHz is due to the vibration of the experiment base, while the noise from the experimental equipment results in high frequency content at around 300 kHz. On the other hand, the content around 100 kHz, which is associated with the received Lamb waves, could be called signal-related content. In contrast to the signal-related content, which varies over time as the sensor signal does, the noise-related content remains unchanged over the entire time span. The excitation frequency of the actuation signal is set as 90 kHz; therefore, the features of the received signal have been highlighted and interpreted physically in the AHWT domain. In comparison, we cannot directly differentiate the features from the noise on the wavelet coefficient map shown in Figure 15(c), where the discrete Daubechies 4 wavelet is used. From Figure 15(d),

we can see a similar pattern in the continuous Daubechies 4 wavelet domain but could not interpret it directly. This is because its wavelet scale is not directly associated with physical parameters. It is also worth mentioning that Daubechies 4 wavelet transforms, which cannot be implemented by FFT, are of lower computational efficiency than AHWT.

AHWT is signal-dependent, i.e., multiple signals measured from the same structure may lead to different ‘best’ wavelet bases, due to the environmental and operational variances. In order to build a consistent baseline data set from multiple signals, my detection algorithm requires a common wavelet basis for all the signals to be compared. In other words, the problem becomes how to find a common wavelet basis such that the overall performance of the wavelet transforms from all the baseline signals could be maximized. It is worth mentioning that I have used the entropy to measure the performance of each wavelet transform, and entropies are addable for independent events. Thus, a natural idea is to use the summation of all the entropies as a measure of the overall performance. Recall that each time series  $\mathbf{s}_l = \{s_l(r), r = 0, 1, \dots, N-1\}$  ( $l = 1, 2, \dots, L$  is the sequence number) collected from the piezoelectric sensors generates a ‘best’ wavelet basis  $\{\mathbf{w}_{mnk}\}_l$  and an vector of wavelet coefficients  $\mathbf{a}_l$ . An entropy  $H(\mathbf{a}_l)$  can then be obtained for  $\mathbf{a}_l$ . Thus, if all  $L$  signals are projected on  $\{\mathbf{w}_{mnk}\}_l$ , then a matrix of wavelet coefficients  $\mathbf{A}_l = [\mathbf{a}_1 \quad \mathbf{a}_2 \quad \dots \quad \mathbf{a}_L]$  can be obtained. Here I define the total Shannon entropy for  $\mathbf{A}_l$

$$H(\mathbf{A}_l) = H(\mathbf{a}_1) + H(\mathbf{a}_2) + \dots + H(\mathbf{a}_L) \quad (16)$$

where  $l = 1, 2, \dots, L$ . Since high sparsity is my objective in the basis selection, I select the common wavelet basis  $\{\mathbf{w}_{mnk}\}_u$  such that the corresponding matrix of wavelet coefficients  $\mathbf{A}_u = [\mathbf{a}_1 \quad \mathbf{a}_2 \quad \dots \quad \mathbf{a}_L]$  have the smallest total Shannon entropy, i.e.,

$$u = \arg \min_l H(\mathbf{A}_l). \quad (17)$$

The baseline data set is then chosen as  $\mathbf{A}_u$ . By applying the same wavelet basis to the newly collected signal, I can obtain the new data vector to be compared with  $\mathbf{A}_u$ . This procedure ensures that the features extracted from the multiple baseline signals are comparable with the features extracted from newly collected signals, while all the advantages of AHWT remain.

### 3.2.2. Feature highlighting and quantitative decision making

Principal component analysis (PCA) is a multivariate statistical procedure that transforms a number of correlated variables into a smaller number of uncorrelated new variables called the principal components (Jackson 2003). The first principal component accounts for as much of the variation in the data as possible, and each succeeding component explains as much of the remaining variability as possible. By eliminating the information not contained in the first few principal components, noise can then be reduced. PCA has been applied in a variety of applications including process monitoring and fault diagnosis (Dunia and Qin 1998).

Consider a block of baseline data denoted by a  $K \times L$  matrix  $\mathbf{X}$ , whose  $L$  column vectors  $\mathbf{x}_1, \mathbf{x}_2, \dots, \mathbf{x}_L$  represent  $L$  signals, each with  $K$  coefficients (dimensions). Specifically in this application, the matrix  $\mathbf{X}$  is normally a part of the baseline data set  $\mathbf{A}_u$ . I can obtain the covariance matrix  $\mathbf{C} = \tilde{\mathbf{X}}\tilde{\mathbf{X}}^T / (L-1)$  using  $\tilde{\mathbf{X}} = [\mathbf{x}_1 - \boldsymbol{\mu} \quad \mathbf{x}_2 - \boldsymbol{\mu} \quad \dots \quad \mathbf{x}_L - \boldsymbol{\mu}]$ , where vector  $\boldsymbol{\mu}$  consists of the sample mean  $\mu_k$  along each dimension ( $k=1, 2, \dots, K$ ). Note that the square root of the  $k$ -th element along the main diagonal of the covariance matrix  $\mathbf{C}$  is the sample standard deviation  $\sigma_k$  along the  $k$ -th dimension. By singular value decomposition, it yields an orthogonal (eigenvector) matrix  $\mathbf{V} = [\mathbf{v}_1 \quad \mathbf{v}_2 \quad \dots \quad \mathbf{v}_K]$  and a diagonal (eigenvalue) matrix  $\mathbf{D} = \text{diag}(\lambda_1, \lambda_2, \dots, \lambda_K)$  such that  $\mathbf{CV} = \mathbf{VD}$ . The eigenvalues are arranged in descending order  $\lambda_j \geq \lambda_{j+1}$  for  $j=1, 2, \dots, K-1$ .

Theoretically, the denoising can be carried out by the following procedure. First I find the effective rank  $rk$  of  $\mathbf{X}$  such that  $\lambda_{y,k} \geq \varepsilon_1 > \lambda_{y,k+1}$  (Konstantinides and Yao 1988), where  $\varepsilon_1$  is the L1-norm of the noise. I then discard the eigenvectors (i.e. replacing them by zero) associated with  $\lambda_{y,k+1}, \dots, \lambda_K$  and form a modified eigenvector matrix  $\mathbf{V}_m$ . However, finding the optimal value of  $\varepsilon_1$  without a specific noise model is generally difficult. Thus, in practice an alternative method is carried out to choose  $rk$  as the smallest number so that accumulative energy is above a certain threshold  $ET\%$ ,

$$rk_0 = \min rk \quad \text{such that} \quad \sum_{j=1}^{rk_0} \lambda_j > ET\% \sum_{j=1}^K \lambda_j. \quad (18)$$

Here recall that the eigenvalues represent the distribution of the original energy among each of the eigenvectors. The selection of an appropriate  $ET\%$  will be discussed in the succeeding sections.

Previous studies have shown that the orthogonal wavelet transform of fractal noise is Karhunen-Loève-like in terms of correlation structure (Wornell 1996), which means the signal-to-noise ratio (SNR) can be enhanced by concentrating signal information to a relatively smaller number of non-zero coefficients. Consider a data vector  $\mathbf{x}_i$  consisting of wavelet coefficients transformed from a test signal  $s_i$ . First I need to standardize it using the same sample mean vector  $\boldsymbol{\mu}$  and the sample standard deviation vector  $\boldsymbol{\sigma}$  for the corresponding block of aforementioned baseline data block  $\mathbf{X}$ ,  $\mathbf{z} = (\mathbf{x} - \boldsymbol{\mu}) / \boldsymbol{\sigma}$ . Then I obtain the reduced-space data  $\mathbf{y} = \mathbf{V}_m^T \mathbf{z}$  by projecting  $\mathbf{z}$  onto  $\mathbf{V}_m$ . Finally the denoised data can be reconstructed as  $\hat{\mathbf{x}} = \mathbf{V}_m \mathbf{y}$ .

Now let us consider how to quantitatively indicate the potential damage from the obtained features. I adopt the Hotelling's  $T^2$  analysis, a widely used approach in multivariate analysis (MacGregor and Kourti 1995; Johnson and Wichern 2007). Its standard procedure consists of two phases. First, baseline data are subgrouped and used to establish an upper control limits

$UCL_1$  under a certain confidence level  $100(1-\alpha)\%$ , where  $\alpha$  indicates the error probability ( $0 < \alpha < 1$ ). I consider a subgroup (block) of the denoised baseline data set  $\hat{\mathbf{X}} = [\hat{\mathbf{x}}_1 \dots \hat{\mathbf{x}}_L]$  with  $L$  signals, each has  $K$  points ( $K < L$ ). Denote the signal mean vector and the covariance matrix as  $\hat{\boldsymbol{\mu}}$  and  $\hat{\mathbf{C}}$ , respectively. The statistic  $T^2$  for the  $l$ -th signal  $\hat{\mathbf{x}}_l$  is defined as  $T_l^2 = (\hat{\mathbf{x}}_l - \hat{\boldsymbol{\mu}})\hat{\mathbf{C}}^{-1}(\hat{\mathbf{x}}_l - \hat{\boldsymbol{\mu}})^T$ ,  $l = 1, 2, \dots, L$ . It is known that Hotelling's  $T^2$  follows the F-distribution (Seber 1984), therefore the phase I upper control limit can be obtained as

$$UCL_1 = \frac{K(L-1)^2}{L(L-K)} F_\alpha(K, L-K) \quad (19)$$

with  $F_\alpha(K, L-K)$  denoting the critical value for an F-distribution with  $K$  and  $L-K$  degrees of freedom. If any signal's  $T^2$  value is beyond the upper control limit and assignable causes are determined, the corresponding signal is omitted from the baseline data set. This procedure is called phase I self-checking. Following that, in phase II, a distinction is made between the baseline and the test data using a modified upper control limit  $UCL_2$ . Assuming the test data is independent of the baseline data, the phase II upper control limit is modified as

$$UCL_2 = \frac{K(L-1)(L+1)}{L(L-K)} F_\alpha(K, L-K) \quad (20)$$

The processing of a test signal follows the same procedure as is done to the baseline data set. If any calculated  $T^2$  value exceeds the phase II upper control limit, we may conclude that, at the confidence level of  $100(1-\alpha)\%$ , the analyzed structure is in damaged state. This completes the development of the signal processing and decision making methodology.

Figure 16 illustrates a complete procedure of detection decision-making. First, five input signals from an undamaged structure are processed to build up the baseline data set. Each input signal generates one 'best' wavelet basis and a corresponding matrix of wavelet coefficients using that basis. Here each matrix consists of  $L = 5$  vectors, whose entropies are summed up as the total

Shannon entropy of that matrix. I select the common wavelet basis as the one with the minimum total Shannon entropy, while the matrix is called baseline data set. PCA truncation is applied to the baseline data set after subgrouping ( $K=3$ ), followed by the Hotelling's  $T^2$  analysis. The phase I upper control limit is used for the self-checking procedure, where outliers are eliminated and the baseline data set is updated. After that, the test signal is processed using the identical common wavelet basis and then denoised by PCA truncation. Finally the  $T^2$  chart quantitatively indicates the extent to which the test data set in every subgroup deviates from the baseline. The damage detection decision is then made based on the statistical analysis at a certain confidence level.

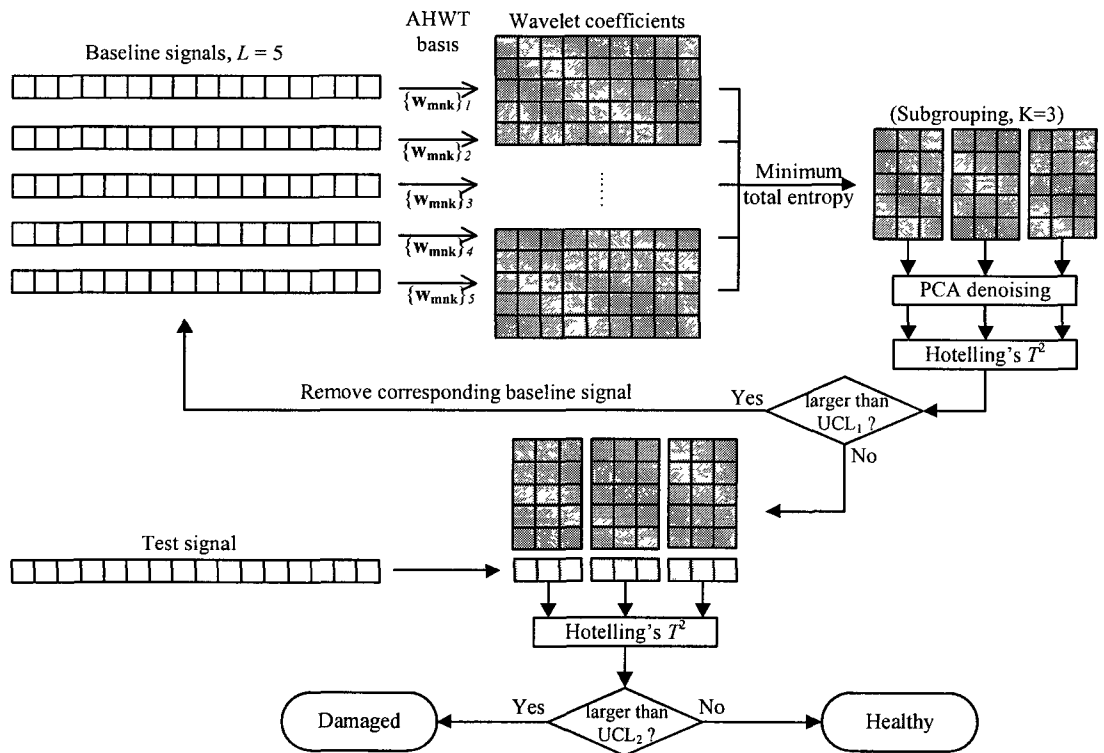


**Figure 16. Procedure of the robust and quantitative decision making ( $N=16$ ,  $L=5$ ,  $K=3$ ).**

### 3.3 Parametric analysis and case studies

In what follows I carry out detailed analysis and case studies of damage detection using the methodology outlined in the preceding section.

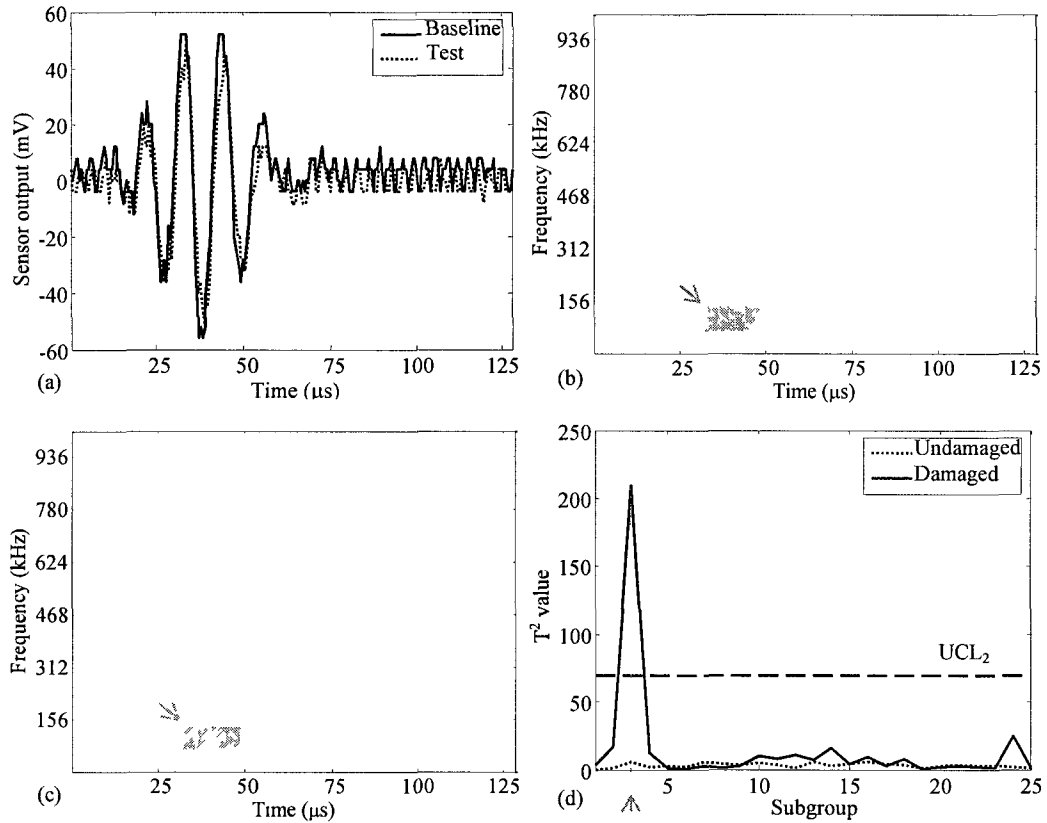


**Figure 17. Damage detection demonstration. (Notch width  $w=0.8\text{mm}$  and depth  $h/2d=33.3\%$ )**

#### 3.3.1. Detection demonstration

I start my discussion with a demonstration of my proposed methodology using experimental signals. I collect a group of eight time series from the undamaged beam and transform them to a matrix of wavelet coefficients using the procedure developed in section 3. Figure 17(a) shows one baseline signal collected via experiment, together with one test signal collected on a test beam with a notch (width  $w = 0.8$  mm and depth-to-beam-thickness ratio  $h/2d = 33.3\%$ ).

Notice that I need all the eight baseline signals for the following data processing, but the solid line in Figure 17(a) represents only one of them. By applying the entropy-based method described in section 3.1, the group of the baseline signals yields a common wavelet basis set. The baseline data set is then obtained by projecting those baseline signals onto the common wavelet basis set. I subgroup the baseline data set into several blocks to perform the PCA-based denoising, where  $\mu$  and  $\sigma$  of each block are recorded for later use. Here I need to consider that small groups lead to more computation loops while large groups may average the deviation within a group and result in meaningless  $T^2$  values. In addition, the subgroup size affects both degrees of freedom for the F-distribution as used in (18) and (19). Therefore, adjusting the size is a complicated trade-off between computational efficiency and detection sensitivity. In this research, after comprehensive simulation studies I make each subgroup contain 5 wavelet coefficients. Next, outliers are eliminated from the baseline data set through the phase I self-checking in the Hotelling's  $T^2$  analysis. Figure 17(b) exhibits the AHWI coefficient map for the baseline signal in Figure 17(a), and Figure 17(c) is the map for the test signal.

The test signal is then processed using the same wavelet basis and other relevant parameters such as  $\mu$  and  $\sigma$ . After that, the denoised test data vector is compared with the baseline data set. A  $T^2$  chart is plotted as the detection result, where each  $T^2$  value indicates the deviation of the test data block from the corresponding baseline data block. If any  $T^2$  value exceeds the phase II upper control limit, we may make a decision that the structure is damaged. Although it seems difficult to recognize the difference between the two wavelet maps by direct observation, the damage can be detected with 90% confidence from the  $T^2$  chart, as shown in Figure 17(d). We can see that the phase II upper control limit is around 70, while the critical subgroup, which marked with an arrow in Figure 17(d), is around 200. In the presence of noise, although the  $T^2$  values may fluctuate case by case, we can always recognize the same critical subgroup via the  $T^2$



chart. The AHWT coefficients belonging to the critical subgroup are also marked with arrows in Figure 17(b)(c). We can see that the marked block is around the center frequency of the excitation signal (i.e., 90 kHz in this case). In other words, we have verified that the frequency shift is insignificant as the Lamb waves travel through the notch, which has been numerically studied by Alleyne and Cawley (Alleyne and Cawley 1992). I also randomly choose one baseline signal as the test signal to simulate the case of an undamaged test beam. The  $T^2$  values are indicated by the dotted line in Figure 17(d). Clearly, all of these values are well under the phase II upper control limit. In conclusion, the proposed robust and quantitative method can lead to correct decision about the beam status, even in the presence of noise and other variations.

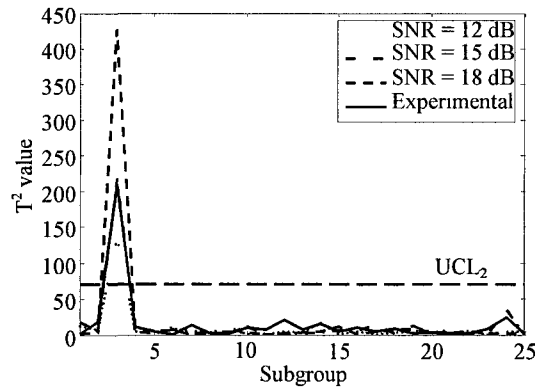


**Figure 18. Detection sensitivity versus signal-to-noise ratio. (Notch width  $w=0.8\text{mm}$  and depth  $h/2d=33.3\%$ )**

### 3.3.2. Estimation of additive noise for numerical simulations

In what follows I discuss the influence of parameters including the center frequency of the excitation signal and notch (damage) size. For such parametric analysis, I mainly use numerical simulation results from the direct finite element analysis. An undamaged beam structure is modeled in ANSYS and meshed mainly by SOLID45 elements with eight nodes and three degrees of freedom (DOF) per node. The Lamb waves are excited by applying pin forces to the nodes located at the two ends of the actuator. The sensor output is obtained through the summation of the strains along the center line of the sensor. The rectangular notch (i.e., the

damage, with the same size as in section 4.1) is introduced by removing elements from the undamaged beam model. Finer meshes around the notch are employed.

In order to perform a parametric study with the finite element model, I incorporate noise into the simulation results so that a group of multiple baseline signals can be constructed numerically. I first estimate the level of the additive noise so that the noisy simulation signals can result in equivalent detection sensitivity compared with experimental signals. According to the central limit theorem, the artificial noise added to numerical signals is assumed as additive white Gaussian noise (AWGN). Figure 18 shows the detection results when using numerical signals with AWGN of different noise levels (SNR = 12, 15, 18 dB). Apparently, this AWGN blurs the numerical signals and therefore reduces the detection sensitivity. Here I regard the level of the noise added to the numerical signals as appropriate if its effect can represent the total effect of all the environmental variations and uncertainties associated with the experiments. In other words, the  $T^2$  values calculated using the experimental signals should be the same as that using simulation outputs added with appropriate AWGN. By comparing the curves corresponding different noise levels in Figure 18, we can see that the numerical signals with SNR = 15 dB result in similar  $T^2$  values as that using experimental signals. Clearly, SNR = 15 dB is a good estimate about the total noise effect. In the following analyses I construct multiple baseline signals as well as the test signal by adding AWGN onto the simulation results while keeping SNR = 15 dB.

### 3.3.3. Truncation threshold $ET\%$ in PCA-based denoising

The truncation threshold  $ET\%$ , as introduced in (18), decides how many principal components are kept in the PCA-based denoising. If too many principal components are kept, meaning too little energy is regarded as noise, then the detection sensitivity would decrease due to the remaining noise. On the other hand, if too few principal components are kept, meaning some signal energy is removed, then the detection sensitivity would also decrease due to less

information provided by the signal. Therefore,  $ET\%$  is an important parameter influencing the effect of denoising.

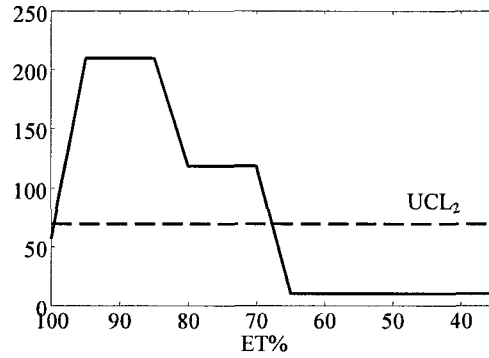


**Figure 19. Detection sensitivity versus truncation threshold. (Notch width  $w=0.8\text{mm}$  and depth  $h/2d=33.3\%$ )**

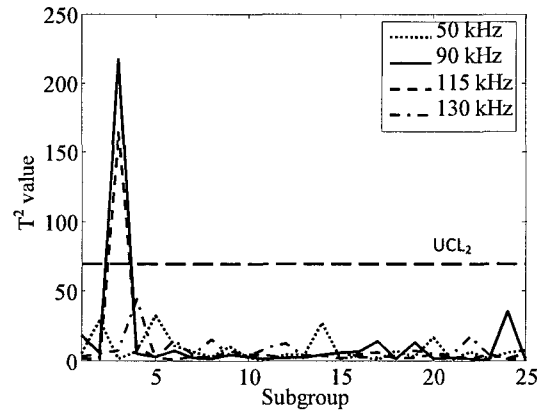


**Figure 20. Detection sensitivity versus center frequencies of the excitation signal. (Notch width  $w=0.8\text{mm}$  and depth  $h/2d=33.3\%$ )**

In my discussion, I consider the peak  $T^2$  value which corresponds to the aforementioned critical subgroup as a measure of the detection sensitivity for each specific configuration. To study the truncation threshold  $ET\%$ , I use the same set of baseline and test signals as in section 4.1. Figure 19 shows the peak  $T^2$  value versus  $ET\%$  when other parameters remain the same. At first, all the principal components are kept when  $ET\%=100\%$  (no denoising). We can see that the peak  $T^2$  value is below the phase II upper control limit, meaning no damage is detected. As  $ET\%$

decreases to 90%, the peak  $T^2$  value reaches its maximum which is above the control limit, meaning that the damage can be detected by the proposed method. When  $ET\%$  goes below 90%, the peak  $T^2$  value decreases again and finally stays below the control limit. Obviously, larger  $T^2$  values would be preferred when processing the same signals, because the detection would be not only more sensitive to small damage but also more robust against signal noises. I thus choose  $ET\%=90\%$  for the following discussions so that  $T^2$  values can be maximized for my specific case.

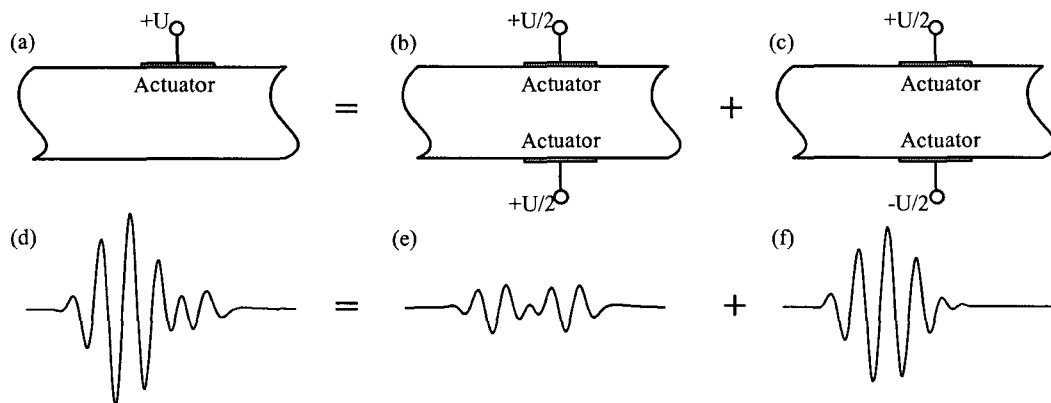


**Figure 21. Equivalent set-ups for generating (a) mixed modes, (b) pure  $S_0$  mode and (c) pure  $A_0$  mode Lamb waves. The same equity holds for the sensor signals (d), (e) and (f).**

### 3.3.4. Detection sensitivity with respect to excitation frequency

Recall that the single piezoelectric actuator excites multiple Lamb modes simultaneously, which in my specific case are the  $S_0$  mode and the  $A_0$  mode. As suggested by Giurgiutiu (Giurgiutiu 2005; Giurgiutiu 2003), damage detection should be carried out at the center frequency where the peak wave amplitude ratio between the  $S_0$  mode and the  $A_0$  mode is the maximum. That center frequency is the ‘sweet spot’ I introduced in previous sections. This ‘sweet spot’ frequency has been analyzed systematically in (Wang et al. 2008) and verified through analytical, numerical, and experimental analyses. For my specific case, the ‘sweet spot’ excitation frequency is 90 kHz.

Figure 20 shows the  $T^2$  values calculated using numerical signals with AWGN for different center frequencies.. As demonstrated in section 4.1, here I add AWGN to the numerical simulation so that a group of eight baseline signals can be obtained with SNR = 15 dB. The test signal is then obtained in the same manner. Note that the ‘sweet spot’ 90 kHz indeed leads to better detection sensitivity than other frequencies.

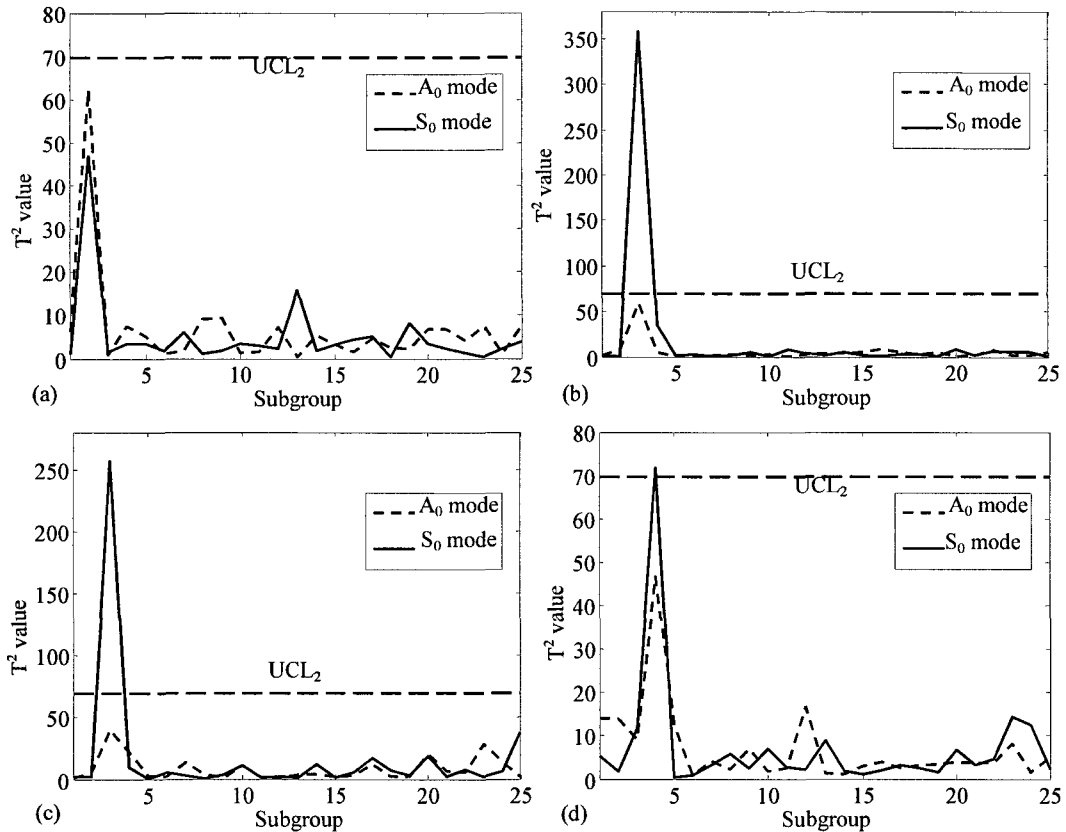


**Figure 22. Detection using pure A0 or pure S0 mode Lamb waves excited at (a) 50 kHz, (b) 90 kHz, (c) 115 kHz and (d) 130 kHz. (Notch width  $w=0.8\text{mm}$  and depth  $h/2d=33.3\%$ )**

Since the ‘sweet spot’ depends on both the  $S_0$  and  $A_0$  Lamb modes, I want to evaluate the individual effects of the  $S_0$  and  $A_0$  Lamb modes under the proposed robust decision making methodology. Since pure  $S_0$  or  $A_0$  mode excitation cannot be achieved by single actuator, in this particular discussion I use two actuators attached on the top and bottom surfaces of the structure.

Thus, pure symmetric Lamb wave modes can be excited by applying in-phase excitation signals onto both actuators, while anti-symmetric modes can be excited by applying out-of-phase excitation signals. Correspondingly, I modify my numerical simulation by introducing the equivalent set-ups shown in Figure 21, where the set-up for generating mixed  $S_0$  and  $A_0$  modes in Figure 21(a) can be replaced by those in Figure 21(b)(c). The actuators in Figure 21(b) generate pure  $S_0$  mode while those in Figure 21(c) generate pure  $A_0$  mode. The summation equality holds for the signals received by the piezoelectric sensor. Examples of the corresponding time domain signals are shown in Figure 21(d), (e) and (f), respectively. Figure 22 shows the detection results for the cases where pure  $S_0$  mode or pure  $A_0$  mode is excited. Each subplot corresponds to one excitation frequency: 50 kHz, 90 kHz, 115 kHz or 130 kHz.

Here I can quantify the detection performance with the presence of noise using the methodology developed in the above sections. As shown in Figure 20, the same trend can be observed for the peak  $T^2$  values, where both the baseline and test signals are contaminated by artificial noises. The discussion in (Wang et al. 2008) also showed that pure  $S_0$  mode leads to a similar trend, while the pure  $A_0$  mode leads to an opposite trend (i.e., negative energy difference). These can now be verified by the peak  $T^2$  values in Figure 22, where the pure  $S_0$  mode always leads to better detection results than the pure  $A_0$  mode. In particular, the peak  $T^2$  value is about 350 for the case that the 90 kHz pure  $S_0$  mode is excited (Figure 22(b)), while that for the case of pure  $A_0$  mode is only around 50 (below the control limit). In comparison, the mixed modes lead to a peak  $T^2$  value about 220 (Figure 20). This indicates that the detection sensitivity is negatively affected by the  $A_0$  mode excited. Using the quantitative decision making method, I have thus verified that for my specific case the ‘sweet spot’ frequency (around 90 kHz) leads to the optimal detection sensitivity, in the presence of noises.

### 3.3.5. Detection sensitivity versus notch depth and width

After analyzing the parameters of the experiment and simulation, I now discuss the detection sensitivity versus the notch depth/width. It is worth mentioning that the single actuator set-up (Figure 21(a)) is used for the following discussion to simulate the effect of mixed  $S_0$  and  $A_0$  modes. In general, larger notches cause more wave energy reflection than smaller notches do, which means more significant difference would be observed in sensor signals. Therefore, we may expect higher  $T^2$  value for larger notches. In this case, the notch size is determined by two parameters: depth and width.

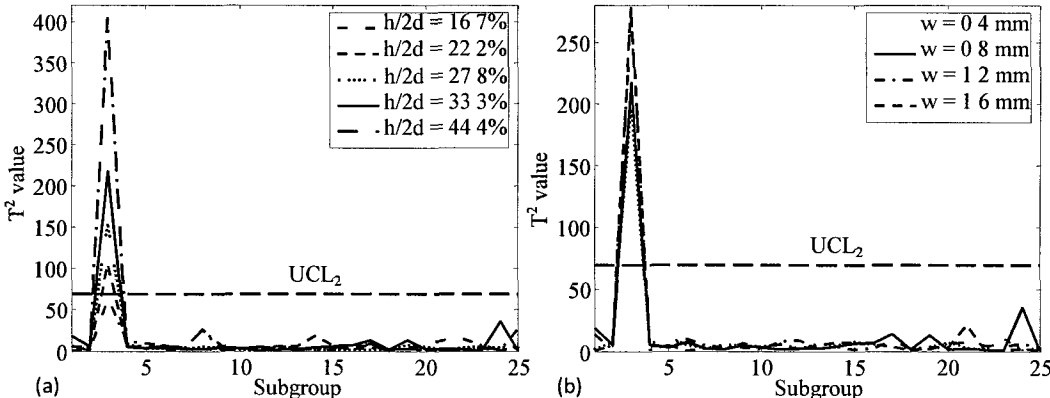


**Figure 23. Detection sensitivity versus (a) notch depth (when  $w=0.8\text{mm}$  is fixed) and (b) notch width (when  $h/2d=33.3\%$  is fixed).**

I first vary the notch depth and keep the notch width fixed as 0.8mm. By modifying the finite element model, I can numerically obtain sensor outputs for different notch depths (from 16.7% to 44.4%). Figure 23(a) shows the detection results as a function of  $h/2d$ . We can see that  $T^2$  values increase as the notch depth increases, meaning that the deeper notches greatly weaken the transmitted wave energy. For the confidence level  $100(1-\alpha)\% = 90\%$ , it can be seen from Figure 23(a) that a 0.8mm wide notch with  $h/2d = 22.2\%$  can be successfully detected.

In comparison, Figure 23(b) shows the detection results for notches with different width when keep the notch depth fixed as  $h/2d = 33.3\%$ . We can see that the  $T^2$  value doesn't change too much as the notch width changes, meaning that the notch width is not a major factor to the

detection sensitivity. Similar observations have been discussed by Alleyne and Cawley (Alleyne and Cawley 1992) in terms of transmission and reflection ratios. From Figure 23(a)(b), I confirm that when the notch width is small compared to the wavelength, as is usually the case in practice, the major factor to the detection sensitivity is the notch depth.

### **3.4 Concluding remarks**

In this research, I develop a combination of signal processing tools for the analysis of Lamb wave-based damage detection using piezoelectric transducers. An improved adaptive harmonic wavelet transform approach is used to extract the common features from multiple baseline signals. This is followed by principal component analysis for feature highlighting and denoising. Quantitative decision making is realized by using Hotelling  $T^2$  analysis that declares damage occurrence under given confidence level. Collectively, these analysis tools lead to a robust and quantitative damage detection methodology for structural components utilizing active interrogation. Experimental, numerical, and analytical studies are carried out on laboratory beam structure to demonstrate and verify the detection performance. A series of parametric studies have been conducted to verify previous theoretical analysis and thus provide general guidelines for similar damage detection applications.



## **Chapter 4. Wireless Sensing Platform for Distributed Signal Processing and Decision Making**

In Chapter 2 and Chapter 3 I discuss autonomous and robust signal processing algorithms for machinery health monitoring and structural damage detection. These algorithms require little or no human intervention. The detection performance is not affected by operation and environmental noises embedded in the signals. In this chapter, I develop a wireless sensing platform that can be used in future to further analyze the decision-making approaches in practical implementation under wireless setting. In order to facilitate detection using a variety of sensors, this platform includes an interface between actual sensors and the local signal acquisition/processing/transmission. For prototyping purposes, I here use an array of microphones as the sensors for implementation demonstration. Recall that microphones have been used for gearbox condition monitoring in Chapter 2. The non-contact nature of microphones can provide extra mobility, flexibility and great potential for further array sensing and signal processing development for future development.

An electret condenser microphone can collect acoustic emission signals of satisfactory quality. An array of multiple microphones can achieve advanced tasks such as localizing the acoustic source: the array can sense the phase difference between any two members, and thus the direction of arrival (DOA) of the sound source can be estimated with any given physical and geometric configuration. In real world application, however, it is still challenging because the received signals are always contaminated with noises. Signal processing techniques again plays a key role. Generally speaking, the more microphones I have in an array, the better performance I can achieve. However, multiple sensors mean more energy consumption, more computational cost and more data to be transmitted. There is a trade-off between performance and material/computational costs.

Wireless technology facilitates damage and fault diagnosis by providing extra flexibilities to the signal acquisition as well as the post-processing. This is especially helpful for hard-to-access systems like wind turbines in remote areas. If equipped with the autonomous and robust methodology introduced in previous chapters, such a system can greatly reduce maintenance costs compared to conventional wired devices. However, the limited power supply and computational resources of a wireless node is a major constrain. Certain powerful but energy demanding IC chips may not be directly used. Similarly, I may give up some well-developed algorithms for local signal processing because of their high computational cost. The relatively low bit rate of wireless transmissions is also a disadvantage to condition monitoring applications. For example, a typical radio from ChipCon (CC24200) can handle up to 250 kbit/s or over 30 kbyte/s, which may not be enough for on-line data transfer from a gearbox running at a normal speed. To solve such issue, I may either adopt a data compression algorithm before the transmission or improve the coding/decoding mechanism in the transmission itself. Throughout the design process I have to carefully consider energy/computational costs, as the power consumption of data processing and data communication are generally interrelated to each other (Liu and Yuan, 2008).

In this chapter, the goal is to design a wireless sensing system that is able to collect signals from an operating machinery, process the signals locally and/or transmit signal features to a workstation for diagnosis. As the first stage, I present a platform prototype that incorporates basic components such as a sensor array, a multi-channel analog-to-digital converter (ADC), a computational module with an operation system (OS), and a wireless transceiver. Hardware components need to be selected based on both their power consumption and performance features. Off-the-shelf wireless nodes require careful selection: some built-in functions may facilitate my own development while others may be solely a waste of energy in this applications. Another challenging work is the software interfacing, without which a software program cannot detect

hardware devices, let alone configure and control them. Since all the algorithms are implemented in nesC language which is optimized for wireless applications, the debugging process is not trivial. After hardware prototyping and software programming, the platform can perform signal collection, local processing and wireless transmission. Preliminary results and analysis are presented.

#### 4.1 Hardware and software development of the wireless sensing platform

The prototype platform consists of hardware components and software programs. Building prototypes for wireless applications used to be a time-consuming work, in which the hardware part alone involves intricate circuitry and thus intensive debugging. Thanks to technology advances and commercialization, a variety of well-developed devices can now be purchased at a reasonable price. For example, based on my requirements and constraints, I could select an off-the-shelf wireless node (also known as a ‘mote’) which itself includes a processor, power supply and management, radio and antenna, and input/output ports. Those motes are often supported by ready-to-use operation systems, which can further facilitate the software development. On top of the hardware, I also need to write software interfaces and high-level applications so that user-defined tasks (e.g., local signal processing) can be accomplished.

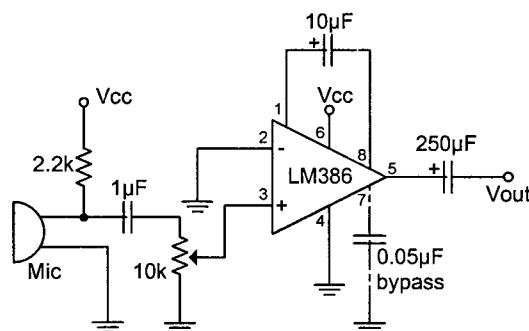


Figure 24. Microphone circuit on the Imote2 wireless node.

#### 4.1.1. Hardware prototyping

My wireless sensor prototype is based on Imote2, a wireless node with excellent computational capability, wide variety of I/O ports and well-developed operation systems. Several motes are commercially available, each with a specialized configuration. Intel Mote 2, also known as Imote2, stands out in its category because of its excellent computational capability (Marvel PXA27x ARM processor with 11-400 MHz and 256kB SRAM, 32MB FLASH, 32MB SDRAM), wide variety of I/O ports (UART, I2C, SPI, I2S, USB, AC97, GPIO, etc) and OS supports (Microsoft .NET Micro, Linux, TinyOS). Since introduced in 2006, Imote2 has quickly drawn attentions from developers in various fields such as structural health monitoring (Rice and Spencer Jr. 2008), volcano monitoring (Xu et al. 2009), and human behavior interpretation (Lymberopoulos et al. 2008). Imote2 can minimize its power consumption and maximize its supporting flexibility when acting as a base to different sensors. Direct memory access (DMA) is another helpful feature. DMA allows certain peripheral devices or companion chips to transfer data to and from memory independently of the processor.

ADCs and sensors are connected to the mote through the I/O ports. Crossbow actually has a basic sensor board (ITS400) that contains a 3D accelerometer, a temperature/humidity sensor, a light sensor and a 4-channel ADC. Although four channels are sufficient for my sensor array design at this stage, I didn't choose that ADC on the ITS400 board because it can only sample one input line at a time through its multiplexer. If all the four channels cannot be sampled simultaneously, then the introduced time delays may complicate the succeeding signal processing and even the fault diagnosis algorithm. With such a consideration, for on-board data acquisition, I select the Texas Instruments (TI) ADS1174, a 4-channel 16-bit ADC that allows simultaneous sampling over all the channels. When operates in a low-power mode, it only consumes 7mW of energy per channel. In addition, the ADS1174 is configured by simply setting the appropriate I/O pins – there are no registers to program. Another useful feature, only in the SPI (Serial Peripheral

Interface) format though, comes from the pin. Just like a trigger, the pin goes low once valid data are ready for retrieval. The software driver, thus, just needs to set up a DMA channel between the ADC and the memory. In the Time-Division Multiplexing (TDM) mode, digital signals from all the channels would then be shifted out sequentially through the DOUT1 pin.

The supporting circuits for the ADS1174 also include but are not limited to a crystal oscillator, input amplifiers, a voltage reference and power supplies. The ADS1174 requires three power supplies for operation: analog supply AVDD, I/O supply IOVDD and digital core supply DVDD. Eventually all of them should be connected to the Imote2. For current prototype, I connect only IOVDD and DVDD to the Imote2 while using a DC power supply (Agilent E3612A) for AVDD. Since AVDD also powers the microphone array, I don't want to exhaust the Imote2's batteries too fast by connecting AVDD onto it. Also, with the DC power supply I can easily monitor the power consumption of the analog part.

Building the sensor array becomes relatively straightforward on top of the above development. I choose the widely used Panasonic WM-61B omni-directional electret condenser microphone as my acoustic sensor. The audio amplification circuit with gain of 200 is designed around an LM386 op-amp as shown in Figure 24. On each wireless sensor node there are four such circuits and thus microphones.

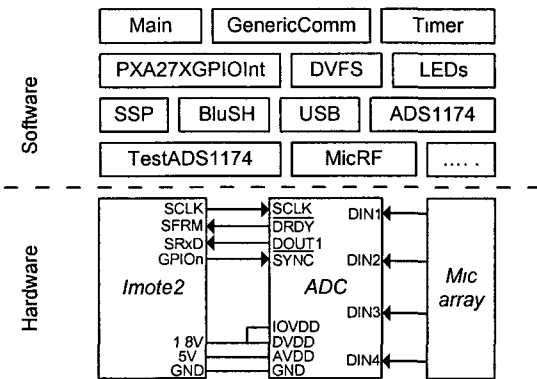


**Figure 25. Hardware and software block diagram**

#### 4.1.2. Software programming

Software interfaces (also called drivers) connecting the hardware and the higher-level applications are the key for the entire platform to function as a whole. Owing to the well-developed Imote2, basic drivers have been included in TinyOS. TinyOS is an open-source operation system designed for wireless sensor networks. It features a component-based architecture optimized for the memory limitations of sensor networks. Programs in TinyOS are built out of components. Components are connected to each other using interfaces. My software development process has been simplified since TinyOS provides interfaces and components for common functions, such as packet communication, clock/timer, LEDs, power management, memory access, and the I/O ports on Imote2. All the TinyOS applications are written in nesC, a dialect of the C language.

In Figure 25 I illustrate TinyOS components involved in this case, including the core ADS1174 component. It provides two interfaces: StdControl and SensorData. Through StdControl, other components can initialize, start or stop the ADS1174 component. If other components call through SensorData, then the requested number of data will be shifted out of the ADC and into the specified buffer. On the other hand, the ADS1174 component itself calls other components. For example, it uses SSP component for preparing DMA channels and transferring ADC data into buffers. Many details need to be considered during the implementation. For example, the timing characteristics of the SPI defined in the Imote2 are different from that defined in the ADC, which makes the data transmission miss the first bit after each interrupt. This problem could be solved by adding a complex programmable logic device (CPLD) between the ADC and the Imote2. However, I choose a simple bypass. As we know, the first bit of each sample represents its sign -- positive for inputs higher than the reference voltage while negative for the rest. If we limit the input signal to the positive (or negative) half, then the first bit doesn't play a significant role any more. The cost of the bypass is losing 8-bit resolution, but I think it's acceptable in this

application. As an ADC driver, ADS1174 allocates memory, prepares DMA channels, and transfers data from the ADC to the system buffer.

The TestADS1174 component is for testing the functionality of the ADC. It first initializes the ADS1174 and other components used and then prepare a buffer for the data to be transferred to. When the user types in the command to get data, the TestADS1174 component requests the specified number of data from the ADS1174 component through its SensorData interface. The ADS1174 component will signal the completion back to the TestADS1174 component when the buffer is filled. The sampling parameters such as sampling frequency, data length and channelID will be packed into a header to be transmitted in front of the data messages. All of them are sent to a PC via the USB component and saved in data files. I can open and read the files in MATLAB and conduct further analysis accordingly.

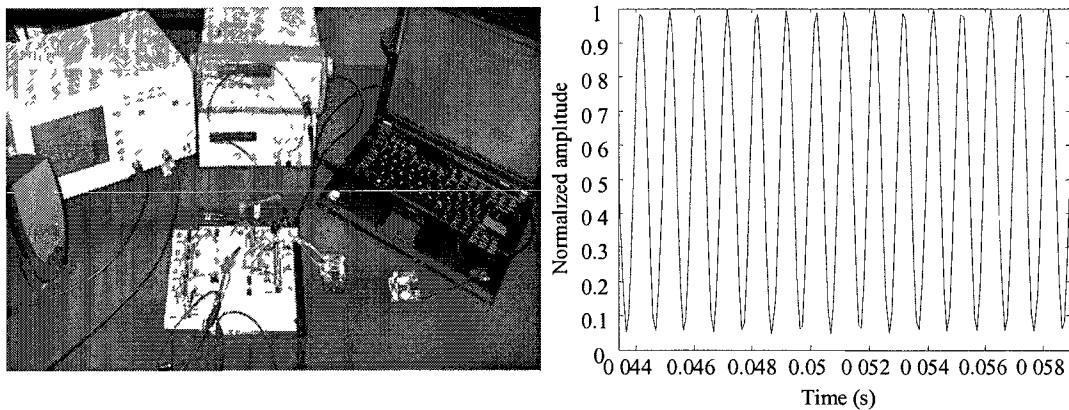


**Figure 26. The prototype platform and the testing system. A segment of data received by the local Imote2 transmitted via SPI port.**

In the current stage, only 1 channel of data is collected by the ADS1174 component through the ADC hardware. Proceeding to the 2-channel case requires increasing the data width from 16 bits to 32 bits for each DMA transfer. However, the 4-channel case cannot be achieved by one SPI port, because each SPI port on the Imote2 has only 32-bit FIFO buffer, meaning that it could only handle 2 channels of 16-bit data. The problem could be solved by using the second SPI port on

the Imote2. The 2 SPI ports share the same interrupt, one port handles the first 2 channels of data, while the other delays its access until the last 2 channels of data are ready. This involves extra interfacing and will be a part of my future development.

The MicRF component tests the entire prototype. It uses the DVFS component for power management, the Timer component for scheduling data acquisitions, the ADS1174 component for data transfer, and the GenericComm component for wireless transmission. When the data are obtained from the ADC, instead of sending them to a PC, the MicRF component pack them into Active Messages (AM is a special message type used by Imote2 for wireless transmission). A data transfer task is then posted to send the AMs sequentially to a remote Imote2 through the radio. In TinyOS, tasks are functions whose execution may be preempted by other asynchronous code. Once scheduled, tasks run to completion and do not preempt one another. So far I haven't included local signal processing into the MicRF, but algorithms can be easily integrated into the MicRF component in future developments.

The TinyOS programs come with a Makefile that allows platform selection and invokes the compiler with appropriate options. The operation system itself is not installed into the Imote2 as Windows is into a PC. Instead, TinyOS code is statically linked with the program code, and compiled into a binary file using a custom GNU toolchain. The binary file is then loaded into the Imote2 through a USB loader host. After reboot, the Imote2 automatically runs the program.

## **4.2 Test results**

The testing system as shown in Figure 26 consists of a waveform generator (Agilent 33220A), a power supply (Agilent E3612A), an oscilloscope (GW instek GDS-820S), a laptop computer with a loudspeaker, the prototype platform (including the local Imote2) and the remote Imote2 connected to the PC via USB. Ideally, the sensing platform uses low-power IC chips and thus can be powered by the local Imote2 alone. In the current prototype I still need a power supply to



provide the 5V DC input because of some non low-power chips involved. However, the imote2 provides the 1.8V input as the IOVDD and DVDD, which will minimize the transition when in the future I remove the external power supply. The loudspeaker is controlled by the PC with MATLAB, acting as a sound source for the microphone array. When test the data transfer in the ADC and the Imote2, I use the waveform generator in order to eliminate the noise factor from the microphone array.

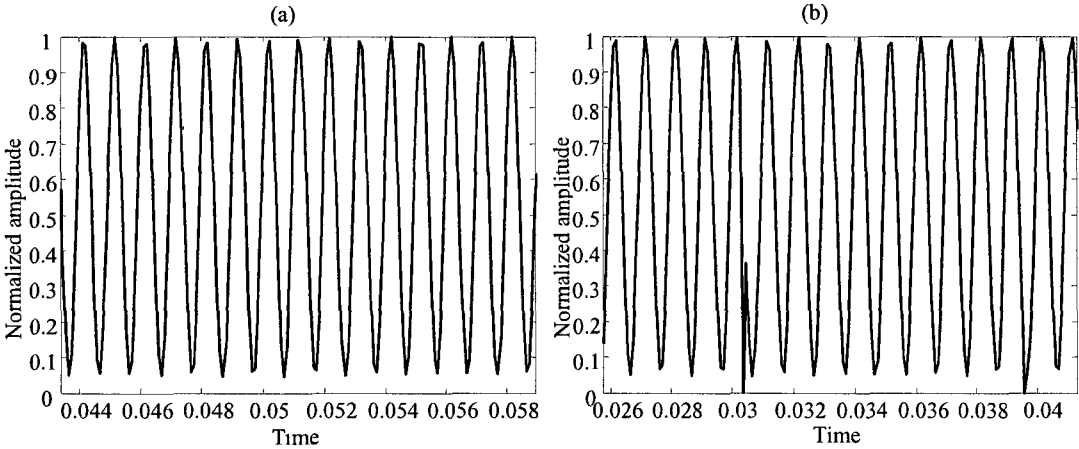


**Figure 27. (a) A segment of data received by the remote Imote2 via wireless transmission. (b) Another segment with discontinuities.**

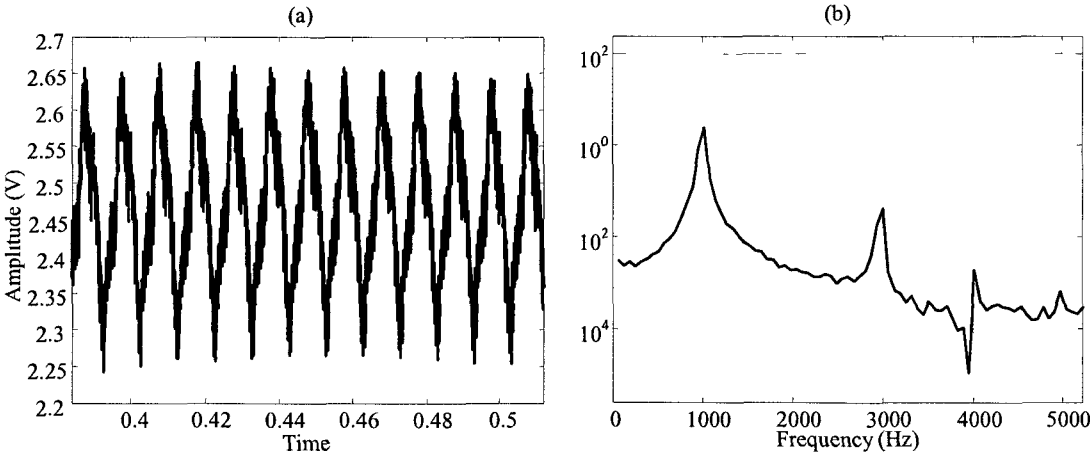


**Figure 28. A segment of data (a) collected from one microphone and its frequency content (b).**

Recall that the program TestADS1174 is written specifically for testing the transfer process. To facilitate debugging, TinyOS itself contains a simple shell interpreter called BluSH that can be accessed by connecting the Imote2 via USB. After the compiled binary file is loaded into the Imote2, I can call the BluSH commands defined in the TestADS1174 component and thus perform data transfer. TinyOS provides such a simple application called iMoteConsole that interfaces with BluSH. The debugging messages are displays in the iMoteConsole, while the digital data received by the Imote2 are forwarded and then saved in a file on the PC through the USB port. In the test, I use the Agilent waveform generator to send a 1kHz sinusoidal as the input signal to the ADC. When the command GetData is called, a block of 1024 data samples are collected. A segment of the data is shown in Figure 26 as an example, with its amplitude been normalized to 1. Preliminary results have demonstrated that the ADC and its SPI connection to the Imote2 are well configured.

After the local data transfer has been tested, I could go one step further to test the wireless transmission between the local Imote2 and the remote one. I compile and load another TinyOS program MicRF into the local Imote2. When turned on, the Imote2 call the GetData command once a second to make the ADC collect 1024 samples. The data are transferred into a buffer whose pointer is returned to the MicRF, which then pack the data into multiple messages to be sent sequentially. The GenericComm component is in charge of sending the messages through the radio at the local side. At the remote side, a program named TOSBase is compiled and loaded into the Imote2. TOSBase will act like a base station that receives the messages and forwards them to the connect PC via a UART serial port on the Imote2. In the remote PC, the data are again forwarded by a java program called SerialForwarder, which acts like a proxy for other programs to read and write the data. I use the java program Oscilloscope to display the received data on the screen and save them into a text file for future access. Figure 27 (a) and (b) each shows a segment of data saved by Oscilloscope. From Figure 27 (b), I can observe a missing data

point (at around 0.086 s along the time axis) and a discontinuity (at around 0.094 s). The missing point is more possible due to the wireless transmission error, since we can see all the following data points are shifted 1 point earlier. According to the IEEE 802.15.4 protocol adopted by the Imote2, the confirmation/acknowledgement mechanism in wireless transmission is by default weak because of the simplicity of the protocol. For higher network layers, the generic communication application GenericComm doesn't have any acknowledgement or confirmation. This left room to improve the wireless transmission quality in future developments: some confirmation/acknowledgement mechanism would be included in the GenericComm application. The above tests are performed by connecting a waveform generator for the analog signal input, whereas the real input should come from the microphone array. Figure 28 (a) shows a segment of data collected directly from one microphone. The sound source is a 1 kHz pure tone coming from the PC speaker. We can see that the frequency of the data is roughly 1 kHz, but it's heavily corrupted by high frequency noises. Those noises may be due to impedance mismatch. Figure 28 (b) shows the frequency response calculated through FFT, where the frequency range is limited to about 5 kHz (half of the ADC's sampling rate 10.537 kHz). Also, the DC component as a distraction has been erased intentionally. These results indicate that the signal quality of the microphone array needs to be improved. The data could be processed even with the noises, but the succeeding DOA estimation would be affected. Thus, improving the microphone array circuit will be included in my future development.

Eventually the platform would be able to handle the 4-member microphone array. To have a flavor of what the data would look like, I sampled the aforementioned 1 kHz sound source through the 4-member microphone array using an ADS1278 (a 24-bit 8-channel version of ADS1174) evaluation board. From Figure 29 we can observe a tiny phase difference between neighboring channels. A correlation-based method may be the most straightforward to find the DOA and thus localize the sound source. Advanced signal processing algorithms are also

available, among which there is a popular category called subspace methods, e.g., MUSIC(Schmidt 1986). If these algorithms are applied in the local Imote2, then I need to consider their restrictions as well as the computational requirements. For example, the original MUSIC assumes the sound sources are in the far field, projecting narrowband signals onto a linear array. From an energy point of view, the computational expense is also a major concern.

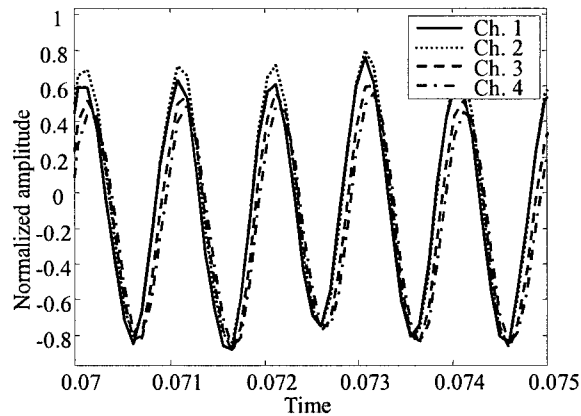


**Figure 29. A segment of data collected from the 4-member microphone array using an ADS1278 evaluation board.**

### 4.3 Concluding remarks

In this chapter, I develop a wireless sensing platform for exploring machinery health monitoring and structural damage detection applications under wireless setting. Analog signals are collected by an array of microphones and converted by an ADC circuit into digital format before going through the on-board signal processing algorithm. The processed data are then transmitted through wireless antenna to another wireless node (usually a more powerful base station) for further analysis and decision making. Development of such a wireless sensing platform enables me to analyze the algorithms I presented in previous chapters in a wireless background. Algorithms' performance depends on various factors when implemented. There is a trade-off between local signal processing and remote decision making after wireless transmission. For

example, intensive local feature extraction may reduce dimensionality of the feature space at the cost of computational power. On the other hand, smaller amount of features requires less energy for the wireless transmission. Outcomes of such case studies can in turn provide a guideline for improving the algorithm I developed. On one hand, the wireless application poses additional challenges. For example, a sustainable power supply must be considered for the system to be truly autonomous, since batteries can only provide limited power supply. On the other hand, there are opportunities associated with such electro-mechanical configuration. Piezoelectric transducers and the coupled circuitry may enable us to tailor the mechanical host structure by tuning the electrical parameters. More details are covered in the succeeding chapter.

## **Chapter 5. Electro-mechanical Tailoring of Structures Through Periodically Coupled Piezoelectric Circuitry**

In Chapter 4, I mentioned one challenge of the wireless sensing platform is its need for continuous energy supply. A sustainable energy source is always preferred, compared to a battery with limited energy supply. One natural thought is that the energy can come from the vibrating host structure through piezoelectric transducers, commonly referred to as energy harvesting these days. Recall in Chapter 3, I have utilized the piezoelectric effect for exciting and sensing Lamb waves. The piezoelectric effect means the appearance of an electrical potential across the transducer patch when it is deformed, and the appearance of deformation when an electrical field is applied. Through the electro-mechanical coupling, the piezoelectric transducers can introduce mechanical stress/strain when electric field is applied or, on the contrary, convert structural vibration energy into electric charge. If connected spatially in a periodic pattern with electrical parameters tuned accordingly, a piezoelectric circuitry has great potential not only for vibration energy harvesting but also for tailoring the mechanical structure to prevent excessive vibration of the host structure. The use of piezoelectric materials and circuitry to alter system dynamics and (vibration) energy flow has been seen in many applications (Tang and Wang 2003; Yu et al 2006; Singh et al. 2004; Rao and Narayanan 2007). In this Chapter, I develop a new approach for manipulating vibratory energy flow in structural elements.

A periodic system (structure) is an assembly of identical subsystems (elements) connected in an identical manner through single or multiple coordinates (Mead 1975). Typical examples include, but are not limited to, rods (Singh et al. 2004; Asiri 2007) and beams (Rao and Narayanan 2007; Mangaraju and Sonti 2004; Yeh and Chen 2006) with spatially periodic supports, turbomachinery bladed disks (Tang and Wang 2003), railway tracks (Gry and Gontier 1997) and conical structures (Tongele and Chen 2004). Harmonic wave motions in such (undamped) perfectly

periodic systems may exhibit unique characteristics: some waves can propagate without attenuation in certain frequency ranges that are called passbands, but in other frequency bands called stopbands waves may be attenuated in amplitude or shifted in phase. The bandwidth and location of those frequency passbands/stopbands are affected by properties such as subsystem length, stiffness or cross-sectional area. For example, the wave propagation characteristics in a beam structure with spatially periodic supports can be altered by changing the stiffness of the spring supports. The amplitude decay and phase change of waves is often expressed in terms of the propagation constant. A propagation constant is defined in such a way that its real part indicates the decay rate of wave amplitude, while its imaginary part measures the phase angle shift. Also, it has been shown that the number of couplings between adjacent elements dictates the number of wave pairs that can exist independently in the system at any frequency. Each wave pair includes two waves traveling in opposite directions but sharing the same decay rate and phase change. By adjusting the system properties, I may control the harmonic wave propagation to meet a variety of application needs (Singh et al. 2004; Asiri 2007; Tongele and Chen 2004). Some studies have proposed to utilize periodic structures as mechanical filters to block vibration transmission within a frequency stopband. Tongele (Tongele and Chen 2004) used a series of conical spikes to form a periodic structure, which could reduce vibration transmission from one end to the other. Its effective frequency range, i.e., the stopband of the periodic structure, is determined by the shape of each conical spike, which implies that the structure is not adaptable to the vibration source once its conical spikes are chosen. In comparison, the passband/stopband of a periodic rod with piezoelectric inserts can be tuned by applying external control voltage (Asiri 2007). However, for each and every piezoelectric insert to produce accurate feedback, such closed-loop active control requires a separate set of control ancillaries such as power amplifiers, phase shifters and signal conditioners.

In what follows, I introduce an integrated electro-mechanical periodic system that consists of a mechanical host structure with piezoelectric transducers attached and coupled through an electrical circuitry. Piezoelectric transducers have inherent capacitance effect. Hagood and von Flotow (Hagood and von Flotow 1991) provided the first systematic analysis for piezoelectric transducers shunted with a resistor circuit (RC) or a resistor and inductor circuit (RLC). They showed that a piezoelectric transducer shunted with the inductor and resistor had an electrical resonance that could be tuned to be similar to a vibration absorber. Since Hagood and von Flotow's initial research, many have worked to understand, optimize, and improve shunting techniques (Wang and Tang 2008). By adaptively tuning the electrical parameters, Hollkamp (Hollkamp 1994) expanded the piezoelectric absorber concept to show that it was possible to suppress multiple vibration modes using a single piezoelectric transducer. Using operational amplifiers (op-amps), one can synthesize electrical elements that can be tuned online to different values, e.g., variable capacitances (Lenk 1993) and variable inductances (Wang and Tang 2008). Such tunable elements have been employed in a variety of smart material-based sensing and control studies (Wang and Tang 2008; Wang and Tang 2010; Park and Baz 2005). Casadei et al. (Casadei et al. 2010) applied shunted piezoelectric transducers periodically to reduce broadband vibration over tunable frequency bands. Each surface-bonded piezoelectric transducer is connected to a single independent RL circuit, and all shunt circuits are tuned to the same frequency. Since in their scheme the transducers are not connected to each other, no additional coupling was created. Instead, vibration energy is dissipated within each shunt circuit. In recent years, there has been a series of research that focuses on converting ambient vibratory energy into useful electrical energy, i.e., energy harvesting. Circuitry design plays an important role in such research that aims at maximizing the energy harvesting efficiency (Anton and Sodano 2007). One advantage that circuitry synthesis entertains in an electro-mechanical system integration is that there is virtually no constraint in choosing the circuitry configuration. Building upon the



previous studies and aiming at taking full advantage of the circuitry concept, here in this research I propose to integrate one or multiple periodically coupled circuits onto the host mechanical structure. By doing so, the overall electro-mechanical periodic system can provide more design freedom for various engineering needs. For example, a simply supported, uniform beam structure itself can be considered as a bi-coupled mechanical system. If piezoelectric transducers are attached to the beam in a spatially periodic manner and identical electrical components are used in each shunt circuit whereas the circuits are coupled through capacitances (Figure 30), the integrated piezoelectric circuitry becomes a mono-coupled periodic system, which provides an additional coupling between adjacent beam segments on which it is attached. Recall that the number of couplings dictates the number of wave pairs that can exist independently in the system. In that way, the integrated system is tri-coupled and thus one more wave pair is induced.

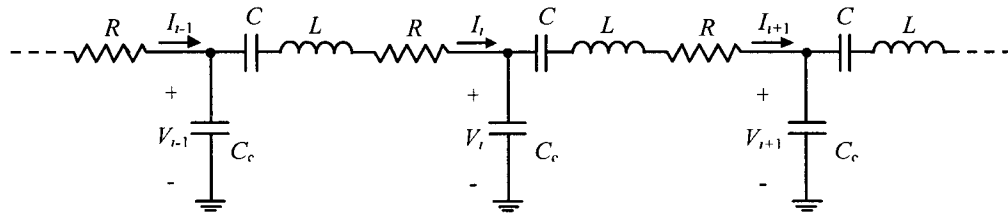


**Figure 30. Mono-coupled periodic circuitry.**

In order to characterize the dynamics of the electro-mechanical periodic system, I adopt a transfer matrix based method. Transfer matrix based methods have been a common choice in the modeling and analysis of periodic structures/systems (Yeh and Chen 2006; Gry and Gontier 1997; Duhamel et al. 2006). Because of the repetitive nature, each subsystem can be described by a transfer matrix that relates the physical coordinates before and after it. The traveling of waves throughout the system can thus be expressed by the product of all the transfer matrices. It has been shown that the eigenvalues of the transfer matrix are exponential functions of the aforementioned propagation constants (Bouzit and Pierre 2000). In addition, the eigenvectors relate the wave amplitudes with the original physical coordinates. By investigating the

generalized eigenvalue problem, I can demonstrate typical passband/stopband behaviors in the proposed electro-mechanical periodic system. Mechanical and electrical energy carried by the electro-mechanical waves in the system can be manipulated through circuitry designs. By tuning the electrical components, I may control the wave propagation and thus the energy flow. Potential applications include, but are not limited to, vibration isolation/suppression and vibration energy harvesting. As pointed out in literature, the mechanism for a periodic system to affect mechanical vibration is different from the damping mechanism where energy is dissipated irreversibly (Castanier and Pierre 1993). Instead, the energy is spatially redistributed within the system. As mentioned above, the harmonic motion consists of different types of waves, all of which are considered in a collective manner. Tuning certain electrical components may benefit vibration isolation, while tuning others may benefit energy harvesting through the piezoelectric circuitry. Comprehensive analyses are carried out to reveal the effects of the inductances, the coupling capacitances and the resistances in different applications. It is worth mentioning that although irregularities (mistuning) in the periodic system may change the dynamic response (Hodges 1982; Pierre et al. 1996), that subject is beyond the scope of this research and will be analyzed in future.

### **5.1 Mono-coupled periodic circuitry**

Let us start the analysis from a mono-coupled electrical periodic circuitry as shown in Figure 30. It is easier than in the analogous mechanical system to see why some frequencies are passed and others are stopped (Brillouin 1953). In the following discussions, I neglect the damping effect caused by the resistors ( $R=0$ ) as it has different nature. Indeed, damping introduces energy dissipation that leads to additional attenuation for all the waves propagating in the system, and such energy dissipation occurs at any frequency. The stop- and pass-band feature of a periodic system, on the other hand, involves no energy dissipation and is frequency selective. Under

harmonic excitation with frequency  $\omega$ , the voltage and current can be denoted by  $V_i e^{j\omega t}$  and  $I_i e^{j\omega t}$ , respectively, in the  $i$ -th circuit loop. I can thus define the electrical state vector  $\mathbf{z}_i^{\text{elec}}$  as

$$\mathbf{z}_i^{\text{elec}} = [I_i \quad V_i]^T \quad (21)$$

From Kirchoff's current and voltage laws, I have

$$\begin{cases} I_{i+1} = I_i - j\omega C_c V_i \\ V_{i+1} = V_i - \left(\frac{1}{j\omega C} + j\omega L\right) I_{i+1} \end{cases} \quad (22)$$

Thus, the adjacent state vectors  $\mathbf{z}_i^{\text{elec}}$  and  $\mathbf{z}_{i+1}^{\text{elec}}$  are related through the frequency-dependent transfer matrix  $\mathbf{T}_i^{\text{elec}}$ . If the system is perfectly periodic, then each transfer matrix is identical, i.e.,  $\mathbf{T}_i^{\text{elec}} = \mathbf{T}^{\text{elec}}$ .

$$\begin{bmatrix} I_{i+1} \\ V_{i+1} \end{bmatrix} = \begin{bmatrix} 1 & -j\omega C_c \\ -\frac{1}{j\omega C} - j\omega L & 1 + \frac{C_c}{C} - \omega^2 LC_c \end{bmatrix} \begin{bmatrix} I_i \\ V_i \end{bmatrix} \quad \text{or} \quad \mathbf{z}_{i+1}^{\text{elec}} = \mathbf{T}^{\text{elec}} \mathbf{z}_i^{\text{elec}} \quad (23)$$

Besides the above model in the physical coordinates, we can also analyze the system in the wave coordinates. According to (Mead 1975), in this mono-coupled periodic system, there is one pair of harmonic waves travelling simultaneously and independently in opposite directions. Let the amplitudes of the right-going and left-going waves be  $a^+$  and  $a^-$ , respectively, the wave propagation can be expressed in terms of the propagation constant  $\mu$ :

$$\begin{bmatrix} a_{i+1}^+ \\ a_{i+1}^- \end{bmatrix} = \begin{bmatrix} e^\mu & \\ & e^{-\mu} \end{bmatrix} \begin{bmatrix} a_i^+ \\ a_i^- \end{bmatrix} \quad \text{or} \quad \mathbf{a}_{i+1}^{\text{elec}} = \mathbf{\Lambda}^{\text{elec}} \mathbf{a}_i^{\text{elec}} \quad (24)$$

where the real part of  $\mu$  describes the decay (or growth) of the wave and the imaginary part describes the phase shift.  $\mu$  is a function of the frequency  $\omega$ . At a certain frequency, if  $\text{Re}(\mu) > 0$  ( $\text{Re}(\mu) < 0$ ), the wave amplitude decays in the negative (positive) direction (Mead 1975). If  $\text{Re}(\mu) = 0$ , the wave pair can propagate without attenuation in amplitude. Therefore,

the frequency range within which  $\text{Re}(\mu) = 0$  is called *passband*, while the one with  $\text{Re}(\mu) \neq 0$  is called *stopband* (Bouzit and Pierre 2000).

Furthermore, I can find a nonsingular 2-by-2 matrix  $\mathbf{V}^{\text{elec}}$  to define the transformation from the physical to wave coordinates:

$$\mathbf{z}_i^{\text{elec}} = \mathbf{V}^{\text{elec}} \mathbf{a}_i^{\text{elec}} \quad (25)$$

Substituting (25) into (23) and comparing it with (24), I obtain the following relation:

$$\mathbf{\Lambda}^{\text{elec}} = (\mathbf{V}^{\text{elec}})^{-1} \mathbf{T}^{\text{elec}} \mathbf{V}^{\text{elec}} \quad (26)$$

From (26) we can see that  $e^\mu$  and  $e^{-\mu}$  are the eigenvalues of the transfer matrix  $\mathbf{T}^{\text{elec}}$  while the columns of the matrix  $\mathbf{V}$  are the corresponding eigenvectors.

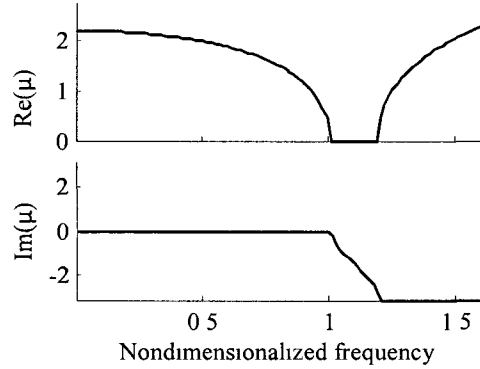


**Figure 31. One propagation constant versus nondimensionalized frequency for the mono-coupled periodic circuitry.**

In the wave coordinates, each wave must have its counterpart propagating in the opposite direction. Therefore, the eigenvalues always exist in reciprocal pairs. For a mono-coupled system, only one  $\mu$  is sufficient to define the propagation properties. Without loss of generality, in the following figures I will only display the one with nonnegative real part in each pair. Figure 31 shows the real and imaginary parts of  $\mu$  versus the frequency nondimensionalized by the natural frequency of each circuit

$$\Omega^{\text{elec}} = \omega\sqrt{LC} \quad (27)$$

In the interest of consistent comparisons, the parameters in this demonstration case are specifically chosen as  $L = 0.0063\text{H}$ ,  $C = 0.0841\mu\text{F}$  and  $C_c = 0.841\mu\text{F}$ . Later discussions in Section 4.3 and Section 5.3 will explain why the values are selected in such a way. In Figure 31 there are two stopbands and one passband within the entire frequency range of my interest. From the filtering perspective, the circuitry acts like a band pass filter whose passband is around  $\Omega^{\text{elec}} = 1$ . The width of such a passband is determined by the coupling capacitance  $C_c$ .

## 5.2 Baseline analysis of host structure without periodic circuitry

To demonstrate the effects of the integrated piezoelectric circuitry, I first analyze the host structure without circuitry as the baseline. Without loss of generality, here I consider an undamped, straight, uniform beam as the host structure. The beam can be analyzed as a periodic structure by using a model with successively connected smaller elements, each having two degrees of freedom coupled with its neighbors as shown in Figure 32. I consider harmonic excitation, and the mechanical state vector consists of four components: deflection  $w$ , slope  $\varphi$ , moment  $M$  and shear force  $F$ . At the coupling point  $i$  along the beam length (Figure 32) I thus have

$$\mathbf{z}_i^{\text{mech}} = [w_i \quad \varphi_i \quad M_i \quad F_i]^T \quad (28)$$

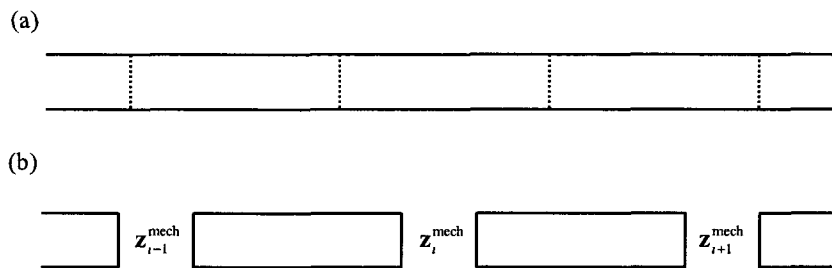


**Figure 32. (a) A bare beam structure virtually divided into identical elements. (b) Beam elements and their state vectors.**

I here consider the beam segment of length  $l$  with the following properties that are constant over its length: cross-sectional area  $A$ , bending stiffness  $EI$ , and mass per unit length  $m$ . Neglecting the damping effects, shear deflection and rotary inertia, I can express the relationship between adjacent state vectors  $\mathbf{z}_i^{\text{mech}}$  and  $\mathbf{z}_{i+1}^{\text{mech}}$  using the transfer matrix  $\mathbf{T}^{\text{mech}}$  (Pestel and Leckie 1963)

$$\begin{bmatrix} w_{i+1} \\ \varphi_{i+1} \\ M_{i+1} \\ F_{i+1} \end{bmatrix} = \begin{bmatrix} c_0 & lc_1 & \frac{l^2 c_2}{EI} & \frac{l^3 c_3}{EI} \\ \frac{\beta^4}{l} c_3 & c_0 & \frac{lc_1}{EI} & \frac{l^2 c_2}{EI} \\ \frac{\beta^4 EI}{l^2} c_2 & \frac{\beta^4 EI}{l} c_3 & c_0 & lc_1 \\ \frac{\beta^4 EI}{l^3} c_1 & \frac{\beta^4 EI}{l^2} c_2 & \frac{\beta^4}{l} c_3 & c_0 \end{bmatrix} \begin{bmatrix} w_i \\ \varphi_i \\ M_i \\ F_i \end{bmatrix} \quad \text{or} \quad \mathbf{z}_{i+1}^{\text{mech}} = \mathbf{T}^{\text{mech}} \mathbf{z}_i^{\text{mech}} \quad (29)$$

where

$$\beta^4 = \frac{\omega^2 ml^4}{EI} \quad (30)$$

and

$$\begin{aligned} c_0 &= (\cosh \beta + \cos \beta) / 2 \\ c_1 &= (\sinh \beta + \sin \beta) / 2\beta \\ c_2 &= (\cosh \beta - \cos \beta) / 2\beta^2 \\ c_3 &= (\sinh \beta - \sin \beta) / 2\beta^3 \end{aligned} \quad (31)$$

Note that the above transfer matrix is derived from the Euler-Bernoulli model. The derivation under other beam theories could follow the same procedure with certain modifications.

The eigenvalues of the transfer matrix  $\mathbf{T}^{\text{mech}}$  are  $e^{\pm\beta}$  and  $e^{\pm j\beta}$  (Pestel and Leckie 1963). Similar to the analysis outlined in Section 2, the wave propagation can be expressed in the wave coordinates as

$$\begin{bmatrix} a_{i+1}^{\text{I}+} \\ a_{i+1}^{\text{II}+} \\ a_{i+1}^{\text{I}-} \\ a_{i+1}^{\text{II}-} \end{bmatrix} = \begin{bmatrix} e^{\beta} & & & \\ & e^{j\beta} & & \\ & & e^{-\beta} & \\ & & & e^{-j\beta} \end{bmatrix} \begin{bmatrix} a_i^{\text{I}+} \\ a_i^{\text{II}+} \\ a_i^{\text{I}-} \\ a_i^{\text{II}-} \end{bmatrix} \quad \text{or} \quad \mathbf{a}_{i+1}^{\text{mech}} = \mathbf{\Lambda}^{\text{mech}} \mathbf{a}_i^{\text{mech}} \quad (32)$$

The eigenvalues and the eigenvectors satisfy

$$\mathbf{\Lambda}^{\text{mech}} = (\mathbf{V}^{\text{mech}})^{-1} \mathbf{T}^{\text{mech}} \mathbf{V}^{\text{mech}} \quad (33)$$

where  $\mathbf{V}^{\text{mech}}$  is the 4-by-4 matrix of eigenvectors and relates the physical and the wave amplitudes

$$\mathbf{z}_i^{\text{mech}} = \mathbf{V}^{\text{mech}} \mathbf{a}_i^{\text{mech}} \quad (34)$$

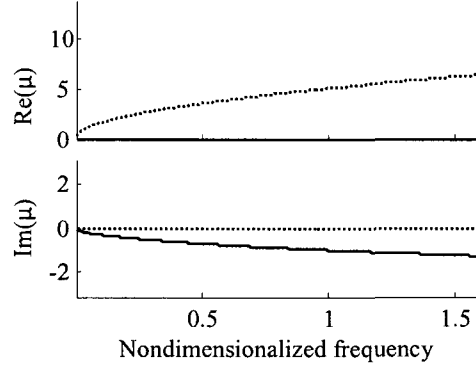


**Figure 33. Two propagation constants (solid line and dotted line) versus nondimensionalized frequency for the bare beam structure.**

The number of coupled coordinates dictates how many pairs of characteristic waves can exist at any frequency (Mead 1973). Thus, I here need 2 propagation constants to describe the wave propagation. In Figure 33 I have their real and imaginary parts plotted. Similarly, the frequency has been nondimensionalized with respect to the natural frequency of each free-free beam segment. The nondimensionalized frequency can thus be expressed as

$$\Omega^{\text{mech}} = \frac{\omega l^2}{\zeta^2} \sqrt{\frac{m}{EI}} \quad (35)$$

where  $\zeta = 4.73004074$  for the 1<sup>st</sup> natural frequency.

Table 1 lists the geometric and material properties of the beam segment I used for this demonstration. We can see that there is always a propagating wave type and an attenuated one, since one of the propagation constant is real while the other is imaginary over the entire frequency range. In other words, regardless how we adjust the structure's parameters, the passband/stopband characteristics cannot be changed.

**Table 1 Mechanical and electrical properties**

	Beam element (Aluminum)	Piezoelectric patch (PZT)
Density $\rho$ (kg/m <sup>3</sup> )	2780	7800
Length $l$ (m)	0.05	0.05
Breadth $b$ (m)	0.0254	0.0254
Thickness $t$ (m)	0.003175	0.000508
Young's Modulus $Y_{11}$ (N/m <sup>2</sup> )	$7.3 \times 10^{10}$	$6.2 \times 10^{10}$
Piezoelectric constant $h_{31}$		$5.9 \times 10^8$
Relative dielectric constant $K$		3800

### 5.3 Electro-mechanical periodic system

Wave propagation becomes more complicated when we integrate the periodic circuitry onto the beam structure since one more coupling leads to an additional pair of waves. I use piezoelectric transducers in this case because they can conveniently convert mechanical energy into electrical energy and vice versa. The converted electrical energy can then propagate through the circuitry in a way similar to the mechanical waves propagating in the mechanical structure. The additional electrical waves introduced can in return affect the host structure through the piezoelectric transducers.

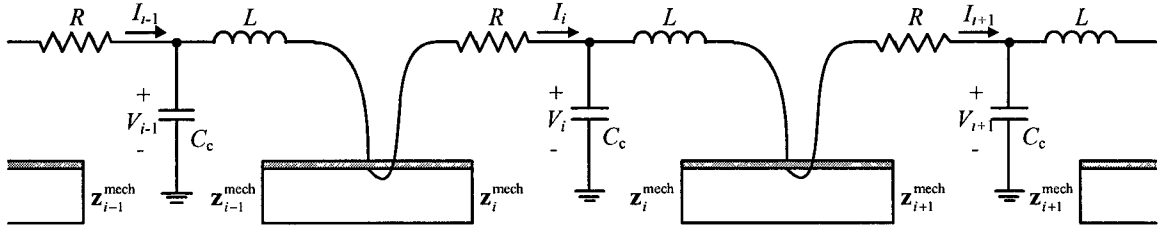


**Figure 34. Tri-coupled electro-mechanical periodic system with a piezoelectric circuitry coupled onto the beam structure.**

#### 5.3.1. Transfer matrix based model including the piezoelectric circuitry

In Figure 34, each piezoelectric transducer patch covers one beam segment and connects to other patches through the circuitry. The bonding layer is non-conductive so that I can have more flexibility in the circuitry design, since the circuits can be grounded in other manners than through the host structure. On one hand, the attachment of piezoelectric transducers inevitably



changes the bending stiffness of the integrated system. For simplicity, the mechanical transfer matrix with the new bending stiffness is still denoted by  $\mathbf{T}^{\text{mech}}$ . On the other hand, the electrical circuits provide an extra coupling coordinate for the total wave motion. Therefore, the new state vector has to include both the mechanical and the electrical variables:

$$\mathbf{z}_i = [w_i \quad \varphi_i \quad M_i \quad F_i \quad I_i \quad V_i]^T = [\mathbf{z}_i^{\text{mech}} \quad \mathbf{z}_i^{\text{elec}}]^T \quad (36)$$

When interacting with the host structure, each piezoelectric transducer patch plays a dual role as energy transducer: it converts mechanical strain or stress into electric charge or voltage, and vice versa. I here adopt the simplified equivalent circuit model, in which each piezoelectric transducer is treated as a voltage source  $V_p$  in series with a capacitor  $C_p$ . First let us consider the voltage generation due to mechanical deformation. From the piezoelectric constitutive equation (IEEE 1987), I can express the stress  $\tau$  and the electric field  $E$  in terms of the strain  $\varepsilon$  and the electric displacement  $D$  so that in the one-dimensional case

$$\begin{cases} \tau = Y_{11}^D \varepsilon - h_{31} D \\ E = -h_{31} \varepsilon + \beta_{33}^e D \end{cases} \quad (37)$$

where  $Y_{11}^D$ ,  $h_{31}$  and  $\beta_{33}^e$  represent the Young's modulus, piezoelectric constant and dielectric constant of the transducer, respectively. The subscripts 1, 2 and 3 denote the  $x$ ,  $y$  and  $z$  directions. By definition, the voltage generated across the piezoelectric transducer patch is  $V_p = Et_p$ , where  $t_p$  is the thickness. Holding the electric field constant in (37), I have

$$V_p = -h_{31} t_p \varepsilon \quad (38)$$

The strain  $\varepsilon$  is usually approximated using the slope at both ends of the beam segment

$$\varepsilon = \frac{t_b}{2l} (\varphi_{i+1} - \varphi_i) \quad (39)$$

Substituting (28) and (39) into (38) and defining  $\alpha = \begin{bmatrix} 0 & -h_{31}t_p t_b / 2l & 0 & 0 \end{bmatrix}$ , I can obtain the voltage  $V_p$  rewritten in the vector form as

$$V_p = \alpha(\mathbf{z}_{i+1}^{\text{mech}} - \mathbf{z}_i^{\text{mech}}) \quad (40)$$

Applying the Kirchhoff's voltage law to the  $i$ -th circuit loop (Figure 34), I then have

$$\begin{cases} I_{i+1} = I_i - j\omega C_p V_i \\ V_{i+1} = V_i - (R + \frac{1}{j\omega C} + j\omega L)I_{i+1} - V_p \end{cases} \quad (41)$$

The capacitance  $C_p$  of each piezoelectric transducer patch is calculated from the material/geometric parameters using the following expression (IEEE 1987)

$$C_p = \frac{K\varepsilon_0 bl}{t_p} \quad (42)$$

where  $K$  denotes the relative dielectric constant of the piezoelectric transducer,  $\varepsilon_0 = 8.9 \times 10^{-12}$  the permittivity of free space and  $b$  the width of the beam (and also the piezoelectric transducer patch).

The electric current due to circuitry dynamics can in turn drive the piezoelectric patch to yield a moment onto the host structure. In this regard, I can treat the patch as an actuator. This time holding the strain constant, I plug  $I_i = j\omega Dbl$  into (37) and obtain

$$\tau = -\frac{h_{31}}{j\omega bl} I_i \quad (43)$$

By integrating over the entire volume of the piezoelectric transducer (Crawley and Anderson 1990), I obtain the total applied moment with respect to the beam's neutral axis as

$$M_p = -\frac{h_{31}}{2j\omega l} \left[ \left( \frac{t_b}{2} + t_p \right)^2 - \left( \frac{t_b}{2} \right)^2 \right] I_i = \kappa_I I_i \quad (44)$$

Define  $\kappa = \begin{bmatrix} 0 & 0 & \kappa_I & 0 \end{bmatrix}^T$  and  $\mathbf{z}_p = \begin{bmatrix} 0 & 0 & M_p & 0 \end{bmatrix}^T$ , and rewrite (44) in the vector form:

$$\mathbf{z}_p = \boldsymbol{\kappa} J_l \quad (45)$$

The mechanical reaction from the piezoelectric transducer can be treated as moment  $M_p$  applied only at both ends of the covered beam segment. Therefore, the relationship between the mechanical state vectors  $\mathbf{z}_{i+1}^{\text{mech}}$  and  $\mathbf{z}_i^{\text{mech}}$  becomes

$$\mathbf{z}_{i+1}^{\text{mech}} = \mathbf{T}^{\text{mech}} (\mathbf{z}_i^{\text{mech}} - \mathbf{z}_p) + \mathbf{z}_p = \mathbf{T}^{\text{mech}} \mathbf{z}_i^{\text{mech}} + (\boldsymbol{\kappa} - \mathbf{T}^{\text{mech}} \boldsymbol{\kappa}) J_l \quad (46)$$

Substituting (46) back into (40) and then to (41), I have  $Q_{i+1}$  expressed in terms of  $Q_i$  and  $Q_{i-1}$  as

$$V_{i+1} = \left[ \varepsilon_l - (\boldsymbol{\alpha} \boldsymbol{\kappa} - \boldsymbol{\alpha} \mathbf{T}^{\text{mech}} \boldsymbol{\kappa}) \right] J_l + \varepsilon_\nu V_i - (\boldsymbol{\alpha} \mathbf{T}^{\text{mech}} - \boldsymbol{\alpha}) \mathbf{z}_i^{\text{mech}} \quad (47)$$

where  $\varepsilon_\nu = 1 - \omega^2 LC_c + \frac{C_c}{C_p} + j\omega RC_c$  and  $\varepsilon_l = -R - \frac{1}{j\omega C_p} + j\omega L$ .

Finally, from (41) (46) and (47), I have the new 6-by-6 transfer matrix  $\mathbf{T}$  in  $\mathbf{z}_{i+1} = \mathbf{T} \mathbf{z}_i$  :

$$\mathbf{T} = \begin{bmatrix} \mathbf{T}_{11} & \mathbf{T}_{12} \\ \mathbf{T}_{21} & \mathbf{T}_{22} \end{bmatrix} \quad (48)$$

where  $\mathbf{T}_{11} = \mathbf{T}^{\text{mech}}$  ,  $\mathbf{T}_{12} = [\boldsymbol{\kappa} - \mathbf{T}^{\text{mech}} \boldsymbol{\kappa} \quad \mathbf{0}]$  ,  $\mathbf{T}_{21} = \begin{bmatrix} \mathbf{0} \\ \boldsymbol{\alpha} \mathbf{T}^{\text{mech}} - \boldsymbol{\alpha} \end{bmatrix}$  and

$\mathbf{T}_{22} = \begin{bmatrix} 1 & -j\omega C_c \\ \varepsilon_l - \boldsymbol{\alpha} \boldsymbol{\kappa} + \boldsymbol{\alpha} \mathbf{T}^{\text{mech}} \boldsymbol{\kappa} & \varepsilon_\nu \end{bmatrix}$ . Comparing (48) to (23) and (29), we can see that  $\mathbf{T}_{11}$  is the

same as the 4-by-4 transfer matrix  $\mathbf{T}^{\text{mech}}$  which relates the mechanical state variables only, while  $\mathbf{T}_{22}$  is derived from the 2-by-2 transfer matrix  $\mathbf{T}^{\text{elec}}$  which relates the electrical state variables only. If they were separate systems, the overall transfer matrix would be a direct sum of  $\mathbf{T}^{\text{mech}}$  and  $\mathbf{T}^{\text{elec}}$ . Now with the piezoelectric coupling of the transducer patches, the overall transfer matrix for the new system has extra terms in  $\mathbf{T}_{12}$ ,  $\mathbf{T}_{21}$  and  $\mathbf{T}_{22}$ , which represents the interactions between the mechanical and electrical subsystems.

### 5.3.2. Eigenvalue problem and wave propagation properties

The new integrated electro-mechanical system has three coupled coordinates and thus three pairs of characteristic waves. Therefore, I can modify the wave propagation equation shown in the preceding discussion by adding another wave pair to reflect the extra degrees of freedom:

$$\begin{bmatrix} a_{i+1}^{I+} \\ a_{i+1}^{II+} \\ a_{i+1}^{III+} \\ a_{i+1}^{I-} \\ a_{i+1}^{II-} \\ a_{i+1}^{III-} \end{bmatrix} = \begin{bmatrix} \lambda_I & & & & & \\ & \lambda_{II} & & & & \\ & & \lambda_{III} & & & \\ & & & 1/\lambda_I & & \\ & & & & 1/\lambda_{II} & \\ & & & & & 1/\lambda_{III} \end{bmatrix} \begin{bmatrix} a_i^{I+} \\ a_i^{II+} \\ a_i^{III+} \\ a_i^{I-} \\ a_i^{II-} \\ a_i^{III-} \end{bmatrix} \quad \text{or} \quad \mathbf{a}_{i+1} = \mathbf{\Lambda} \mathbf{a}_i, \quad (49)$$

where  $\mathbf{\Lambda} = \mathbf{V}^{-1} \mathbf{T} \mathbf{V}$  is the matrix of eigenvalues and  $\mathbf{V}$  is the corresponding matrix of eigenvectors. Again, I have the transformation between the physical and the wave amplitudes expressed as

$$\mathbf{z}_i = \mathbf{V} \mathbf{a}_i, \quad (50)$$

As mentioned, each eigenvalue  $\lambda$  can be written in terms of a propagation constant  $\mu$

$$\lambda = e^{\mu} = e^{\text{Re}(\mu) + j \text{Im}(\mu)} \quad (51)$$

Generally, three cases can be distinguished based on the nature of  $\mu$ . At any frequency, if  $\mu$  is either pure real or of the form  $\text{Re}(\mu) \pm j\pi$ , then the wave is attenuated in amplitude and thus said to be in a frequency stopband. If  $\mu$  is purely imaginary, the wave propagates without attenuation and is said to be in a passband. The wave is otherwise said to be in a complexband where the wave is simultaneously propagating and attenuating along the structure (Bouzit and Pierre 2000).

Those eigenvalues, and thus propagation constants, play a critical role in understanding and analyzing the wave propagation properties for periodic structures. For this 6-by-6 transfer matrix, I can simplify the eigenvalue problem into an equivalent form with fewer variables. Using the reciprocity of the eigenvalues, the characteristic equation of  $\mathbf{T}$  can be reorganized as

$$\left( \lambda + \frac{1}{\lambda} \right)^3 + g_1 \left( \lambda + \frac{1}{\lambda} \right)^2 + g_2 \left( \lambda + \frac{1}{\lambda} \right) + g_3 = 0 \quad (52)$$

where the coefficients are given in terms of the invariants  $I_T$ ,  $II_T$  and  $III_T$  of the matrix  $\mathbf{T}$

$$\begin{aligned} g_1 &= -I_T \\ g_2 &= II_T - 3 \\ g_3 &= 2I_T - III_T \end{aligned} \quad (53)$$

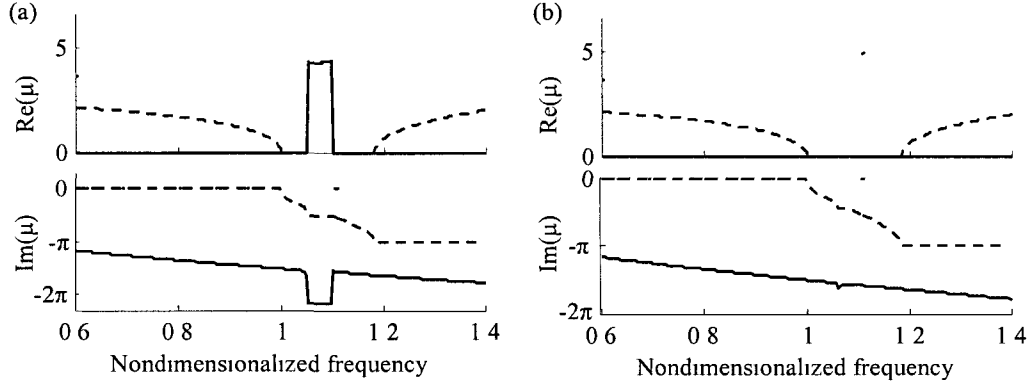


**Figure 35. (a) Three propagation constants (solid line, dotted line and dashed line) versus nondimensionalized frequency for the electro-mechanical periodic system. (b) Two propagation constants (solid line and dotted line) for a separate beam structure, and one propagation constant (dashed line) for a separate periodic circuitry.**

According to the cubic formula, the three roots of (52) are given as

$$\lambda + \frac{1}{\lambda} = \begin{cases} -\frac{1}{3} \left( g_1 + \sqrt[3]{\frac{f_1 + \sqrt{f_2}}{2}} + \sqrt[3]{\frac{f_1 - \sqrt{f_2}}{2}} \right) \\ -\frac{1}{3} \left( g_1 + \frac{1 + \sqrt{3}j}{2} \sqrt[3]{\frac{f_1 + \sqrt{f_2}}{2}} + \frac{1 - \sqrt{3}j}{2} \sqrt[3]{\frac{f_1 - \sqrt{f_2}}{2}} \right) \\ -\frac{1}{3} \left( g_1 + \frac{1 - \sqrt{3}j}{2} \sqrt[3]{\frac{f_1 + \sqrt{f_2}}{2}} + \frac{1 + \sqrt{3}j}{2} \sqrt[3]{\frac{f_1 - \sqrt{f_2}}{2}} \right) \end{cases} \quad (54)$$

where  $f_1 = 2g_1^3 - 9g_1g_2 + 27g_3$  and  $f_2 = f_1^2 - 4(g_1^2 - 3g_2)^2$ . Then, each eigenvalue pair can be solved using the quadratic formula. Such a method of expressing the characteristic equation in terms of invariants has been often adopted for simplification purposes (Romeo and Paolone 2007)

### 5.3.3. Analysis of electro-mechanical interactions in terms of propagation constants

For the tri-coupled periodic structure, with two mechanical and one electrical couplings, three eigenvalues  $\lambda_I$ ,  $\lambda_{II}$  and  $\lambda_{III}$  ( $|\lambda| \geq 1$ ) are sufficient to completely define the wave propagation properties. For demonstration purposes, I plot in Figure 35(a) three propagation constants ( $\mu$ ) versus the nondimensionalized frequency. Three electro-mechanical wave pairs are denoted by solid, dotted and dashed lines, respectively. Mechanical and electrical waves cannot be separated because of the piezoelectric coupling. From Figure 35(a) we can see that one wave pair (solid line) begins with a passband and ends with a stopband, while another wave pair (dashed line) begins with a stopband but ends with a passband. The other wave pair (dotted line) is mainly in a stopband. There is also a small region in which both the real and imaginary parts of the propagation constant are non-zero, so it is a complexband where the wave is simultaneously propagating and attenuating along the structure (Bouzit and Pierre 2000). The location and size of those frequency bands are determined by the system's mechanical and electrical parameters. Recall that in Section 2 I selected the same electrical parameters for the mono-coupled periodic circuitry. Since I integrated exactly the same circuitry, only with  $C_p = C$ , onto the host structure, the discussions here become consistent by this selection. To be exact, here I have  $L = 0.0063$  H so that each circuit's resonance frequency matches each beam segment's natural frequency, i.e.,  $\Omega = \Omega^{\text{mech}} = \Omega^{\text{elec}}$ . The coupling capacitance is chosen as 10 times the piezoelectric patch's capacitance, i.e.,  $C_c = 0.841$   $\mu\text{F}$ . Later in Section 5.3 I will discuss the impacts of different values of  $C_c$ . For comparison, I also plot the degenerated case of  $h_{31} = 0$ , i.e., no piezoelectric coupling, in Figure 35(b). We can see that Figure 35(b) is exactly the combination of Figure 31 and Figure 33 due to the aforementioned selection of the electrical and mechanical parameters. The solid line and the dotted line correspond to the mechanical wave pairs, whereas the dashed line corresponds to the electrical wave pair.

The differences between Figure 35(a) and Figure 35(b) indicate the effects of the electro-mechanical coupling. Before the periodic circuitry is bonded onto the bare beam, no stopband/passband characteristics have been observed from the propagation constants. When each circuit is coupled with the beam segment through a piezoelectric patch, a channel between the mechanical energy in the beam and the electrical energy in the circuit is formed. Therefore, any mechanical vibration in the beam structure will excite electrical dynamics in the circuitry, and vice versa. Also, the segmented nature of the piezoelectric actuation introduces spatial discontinuities onto the host beam structure, so altogether this system becomes an electro-mechanical periodic system. We can thus observe stopband/passband characteristics in this system as shown in Figure 35(a). Around  $\Omega=1.08$  we can see a frequency range within which all three propagation constants have non-zero real part, meaning all three propagating waves experience amplitude attenuation. The larger the non-zero real part, the more severe the attenuation is. By tuning electrical parameters in the system, I can thus alter the dynamic response of the beam structure. Properties and applications of such structure will be discussed further in the following sections.

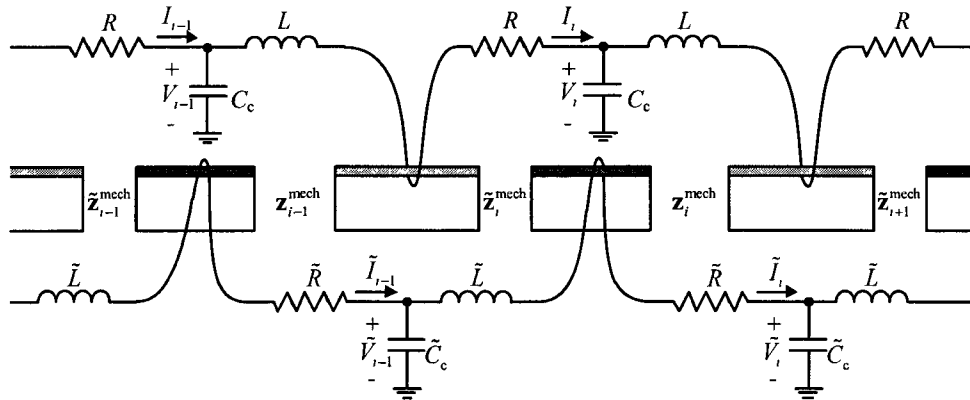


**Figure 36. An electro-mechanical periodic system with two piezoelectric circuitries coupled onto the beam structure.**

#### 5.3.4. Multi-branch circuitries integrated to the electro-mechanical periodic system

A direct extension of the above electro-mechanical periodic system is to apply multi-coupled multi-branch circuitries onto the mechanical structure. Recall that the integration of the above periodic circuitry introduces one more pair of waves propagating in system and thus provides one set of electrical parameters to tune the system dynamics. Adding more circuitry elements can obviously provide more design freedom, and wave interactions will become more intriguing: mechanical vibrations induce electrical charge flows in multiple circuitries, while the circuitries themselves are further coupled through the mechanical structure. More complex energy/wave propagation will occur with such an arrangement. Figure 36 shows an example of such integration, where two circuitries are coupled to the beam through piezoelectric transducer patches independently. The total state vector then becomes

$$\mathbf{z}_i = \left[ w_i \quad \varphi_i \quad M_i \quad F_i \quad I_i \quad V_i \quad \tilde{I}_i \quad \tilde{V}_i \right]^T = \left[ \mathbf{z}_i^{\text{mech}} \quad \mathbf{z}_i^{\text{elec}} \quad \tilde{\mathbf{z}}_i^{\text{elec}} \right]^T \quad (55)$$

where the tilded variables are pertaining to the second circuitry. From the previous derivations, I can easily have two intermediate transformations

$$\begin{bmatrix} \tilde{\mathbf{z}}_{i+1}^{\text{mech}} \\ \mathbf{z}_{i+1}^{\text{elec}} \\ \tilde{\mathbf{z}}_i^{\text{elec}} \end{bmatrix} = \begin{bmatrix} \mathbf{T}_{11} & \mathbf{T}_{12} & \mathbf{0} \\ \mathbf{T}_{21} & \mathbf{T}_{22} & \mathbf{0} \\ \mathbf{0} & \mathbf{0} & \mathbf{I} \end{bmatrix} \begin{bmatrix} \mathbf{z}_i^{\text{mech}} \\ \mathbf{z}_i^{\text{elec}} \\ \tilde{\mathbf{z}}_i^{\text{elec}} \end{bmatrix} \quad \text{and} \quad \begin{bmatrix} \mathbf{z}_{i+1}^{\text{mech}} \\ \mathbf{z}_{i+1}^{\text{elec}} \\ \tilde{\mathbf{z}}_{i+1}^{\text{elec}} \end{bmatrix} = \begin{bmatrix} \tilde{\mathbf{T}}_{11} & \mathbf{0} & \mathbf{T}_{12} \\ \mathbf{0} & \mathbf{I} & \mathbf{0} \\ \tilde{\mathbf{T}}_{21} & \mathbf{0} & \tilde{\mathbf{T}}_{22} \end{bmatrix} \begin{bmatrix} \tilde{\mathbf{z}}_{i+1}^{\text{mech}} \\ \mathbf{z}_{i+1}^{\text{elec}} \\ \tilde{\mathbf{z}}_i^{\text{elec}} \end{bmatrix} \quad (56)$$

where  $\mathbf{I}$  is a 2-by-2 unitary matrix. Thus, the total transfer matrix can be obtained as

$$\mathbf{T} = \begin{bmatrix} \tilde{\mathbf{T}}_{11} & \mathbf{0} & \mathbf{T}_{12} \\ \mathbf{0} & \mathbf{I} & \mathbf{0} \\ \tilde{\mathbf{T}}_{21} & \mathbf{0} & \tilde{\mathbf{T}}_{22} \end{bmatrix} \begin{bmatrix} \mathbf{T}_{11} & \mathbf{T}_{12} & \mathbf{0} \\ \mathbf{T}_{21} & \mathbf{T}_{22} & \mathbf{0} \\ \mathbf{0} & \mathbf{0} & \mathbf{I} \end{bmatrix} \quad (57)$$

Recall Equation (31). In general, the characteristic equation of a higher order transfer matrix can still be written as

$$\left( \lambda + \frac{1}{\lambda} \right)^n + \tilde{g}_1 \left( \lambda + \frac{1}{\lambda} \right)^{n-1} + \tilde{g}_2 \left( \lambda + \frac{1}{\lambda} \right)^{n-2} + \cdots + \tilde{g}_n = 0 \quad (58)$$



where  $\bar{g}$ 's are functions of the matrix invariants. This form may simplify the solution because it reduces the order of the equation by half. For a 4th order equation, we may use the quartic formula to solve for the eigenvalues and thus propagation constants. However, analytical solutions to equations of more than 4th order are generally not available. Then, numerical algorithms are necessary for the calculation. It is worth noting that, although the eigenvalues of (57) can be solved using numerical matrix analysis, here I rewrite the characteristic equation in the form of (58) to retain the physical significance of the wave propagation constants.

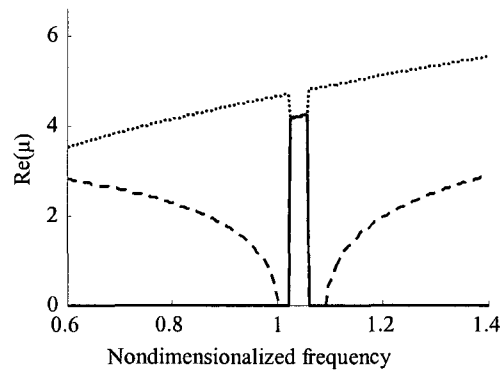


**Figure 37. Three real part of the propagation constants (solid line, dotted line and dashed line) versus nondimensionalized frequency.  $C_c = 1.68\mu\text{F}$  and  $L = 0.0063\text{H}$ .**

## 5.4 Discussions and case studies

### 5.4.1. System dynamics in wave and physical coordinates

As a result of the electro-mechanical coupling, wave propagation in the periodic system exhibits unique features. The following discussions focus on the typical tri-coupled system. In the wave coordinates, for any excitation frequency there are 3 pairs of electro-mechanical waves existing independently and simultaneously in the system. According to (49), each wave may decay at a certain spatial rate or propagate without attenuation from one point to another. Recall that in the baseline analysis of the host structure, one wave can propagate without attenuation at any frequency, whereas the other is always attenuated. When integrated with the periodic circuitry, the mechanical structure's propagation characteristics are affected by the electro-mechanical

interaction. Figure 37 shows the case where the parameters are the same as used in Figure 35(a) except  $C_c = 1.68\mu\text{F}$ , which confirms that the integrated circuitry can create a frequency range (roughly  $\Omega^{\text{mech}} = 1.03 \sim 1.06$  this time) in which the real parts of all the three waves are nonzero. In the wave coordinates, that means all three waves are attenuated when propagating. Recall that the coupling capacitance determines the width of the passband for the electrical periodic circuitry. Here we find that it can affect the electro-mechanical interaction and thus the overall system dynamics. For convenience, hereafter I call this unique frequency range an “all-attenuation zone”. In Figure 37, it can be seen that the “all-attenuation zone” is narrower than that in Figure 35.

The complexity of multi-coupled periodic systems results in difficulties in analyzing the propagation constants. At certain frequency, an individual propagation constant may be in a stopband, or a passband, or a complex band. For a tri-coupled system, we may observe combinations such as pass-pass-pass, pass-pass-stop, complex-stop, stop-stop-stop (Romeo and Paolone 2007). For a periodic system with more degrees of freedom, the combinations can be even more complicated (Pierre et al. 1996). It is worth emphasizing that the wave coordinates serve only as an auxiliary tool for the mathematical modeling and analysis. In real applications, a system’s dynamic behaviors can be directly observed only in the physical coordinates. From (50) we know that each physical response is a linear combination of all the wave responses, related by the eigenvector matrix  $\mathbf{V}$ . For example, the vertical displacement  $w_i$  can be expressed as  $w_i = v_{11}a_i^{\text{I}^+} + v_{12}a_i^{\text{II}^+} + v_{13}a_i^{\text{III}^+} + v_{14}a_i^{\text{I}^-} + v_{15}a_i^{\text{II}^-} + v_{16}a_i^{\text{III}^-}$ , where each  $a$  is the wave amplitude and its weight  $v$  is the first element of that corresponding eigenvector. Therefore, all the wave pairs should be considered in a collective manner. Hereafter my attention is mostly focused on the “all-attenuation zone”, where all three wave pairs experience decay. Consequently, one can expect that the physical wave motion will be attenuated and thus the carried energy will be

confined to a region near the excitation source. As demonstrated in the case studies, this feature can be used for manipulating mechanical and/or electrical energy within the coupled system.

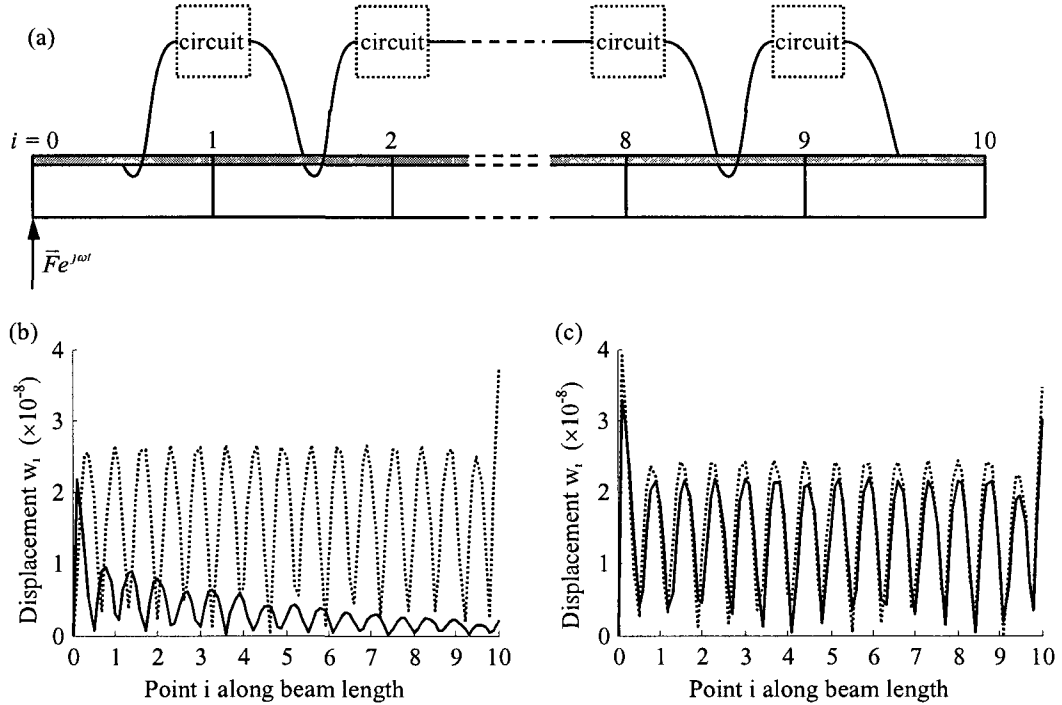


**Figure 38. (a) A 10-segment electro-mechanical system excited by a harmonic force.  $C_c = 1.68\mu\text{F}$  and  $L = 0.0063\text{H}$ . Vertical displacement  $w_i$  along the beam length direction (solid line) compared to that of the bare beam without the PZT circuitry (dotted line). The excitation frequency is (b) within and (c) out of the “all-attenuation zone”.**

#### 5.4.2. Case studies

In the wave coordinates we can better understand the system dynamics, but the responses in the physical coordinates are linear combinations of wave responses. One potential application of the proposed system is to control the vibration energy propagation, i.e., isolating vibration in the mechanical structure.

To demonstrate the effects, I here consider an example of a 10-element electro-mechanical periodic system as shown in Figure 38(a). Each element is mathematically described by (48) and connected to its neighbors as shown in Figure 34. This free-free structure is excited by a

harmonic force of constant magnitude. We choose  $L=0.0063\text{H}$ ,  $C_c=1.68\mu\text{F}$  and other material/geometric properties as listed in Table 1 so that each transfer matrix will be identical to the case discussed in Section 5.1. Therefore, the propagation constants remain the same as shown in Figure 37, where the “all-attenuation zone” is located around  $\Omega=1.03\sim 1.06$ .

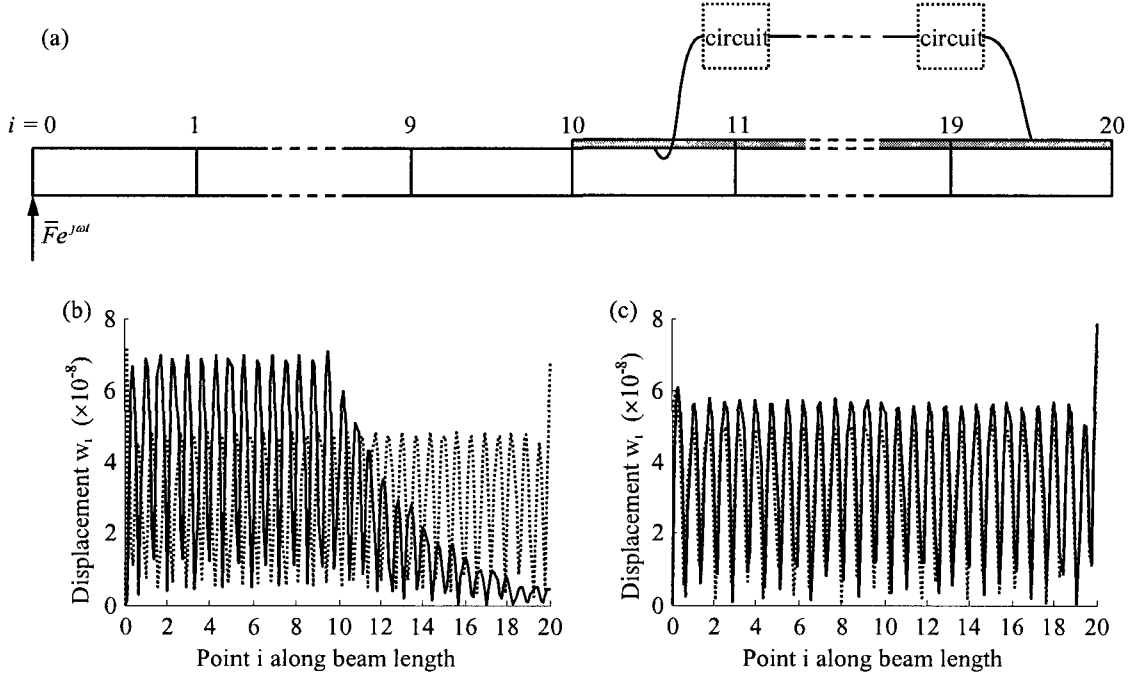


**Figure 39. (a) 20-segment electro-mechanical system excited by a harmonic force.  $C_c=1.68\mu\text{F}$  and  $L=0.0063\text{H}$ . Vertical displacement  $w_i$  along the length direction when the excitation frequency is (b) within or (c) out of the “all-attenuation zone”.**

First let’s see the case where the excitation frequency  $\Omega=1.03$  is within that zone. Using a finite element model, I can easily calculate the vertical displacement  $w_i$  along the length direction. For comparison, I also plot the displacement distribution along the baseline structure without the circuitry. Then, I pick another excitation frequency  $\Omega=0.85$  which is out of the “all-attenuation zone”. In Figure 38(b) and Figure 38(c), the solid line represents the result of the integrated system while the dotted line represents that of the baseline structure. We can see that in Figure

38(b) the mechanical vibration is obviously confined around the source (point 0), whereas in Figure 38(c) it propagates along the structure.

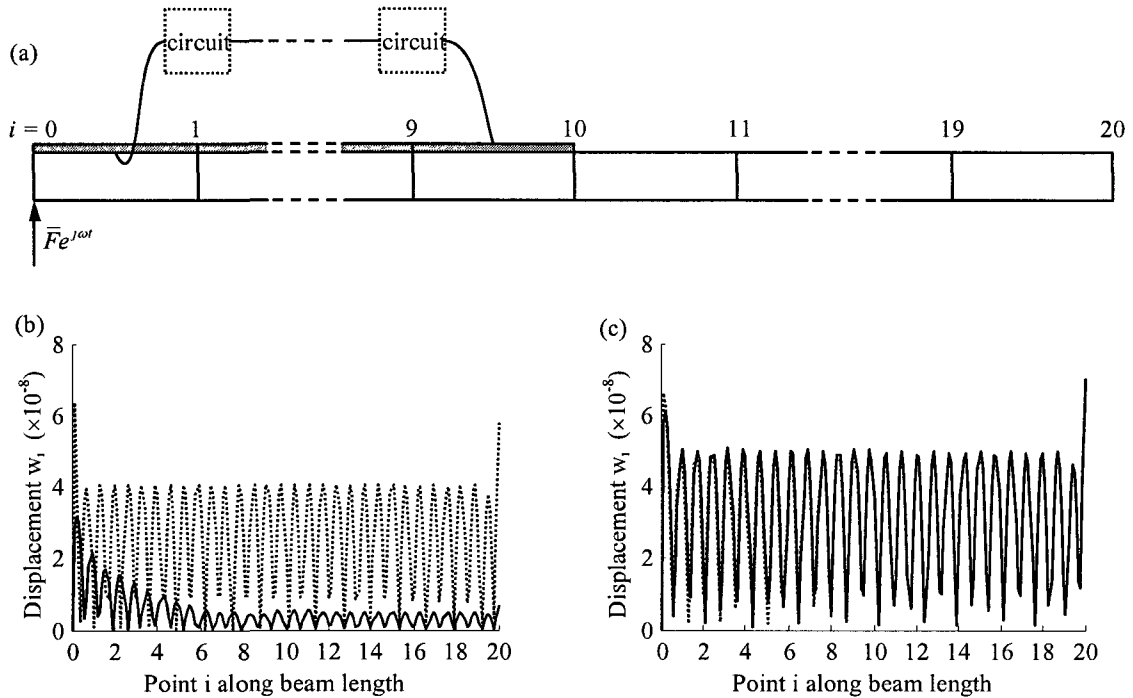


**Figure 40. (a) 20-segment electro-mechanical system excited by a harmonic force.  $C_c = 1.68\mu\text{F}$  and  $L = 0.0063\text{H}$ . Vertical displacement  $w_i$  along the length direction when the excitation frequency is (b) within or (c) out of the “all-attenuation zone”.**

The above example demonstrates the application in vibration isolation when the piezoelectric circuitry covers the entire host beam. I can have more flexibility in the system tailoring by integrating the piezoelectric circuitry at different locations of the host beam. Figure 39(a) shows an example that the electro-mechanical system is formed at the right hand side of the host beam. The excitation source and boundary conditions remain the same as above. Following a similar finite element analysis, the vertical displacements are calculated and plotted in Figure 39(b) where  $\Omega = 1.04$ . Compared to Figure 39(c), it can be seen that, when the frequency falls within the all-attenuation zone, the vibration in the right hand side of the system has been significantly reduced. Similarly, I can deploy the piezoelectric circuitry at the left hand side of the host beam

as shown in Figure 40(a). When the frequency falls within the all-attenuation zone, the vibration of the entire beam structure can be reduced, since the circuitry is near to excitation source. By properly adjusting the configuration of the integrated circuitry on the host structure, I can guide the vibration energy into desired regions.

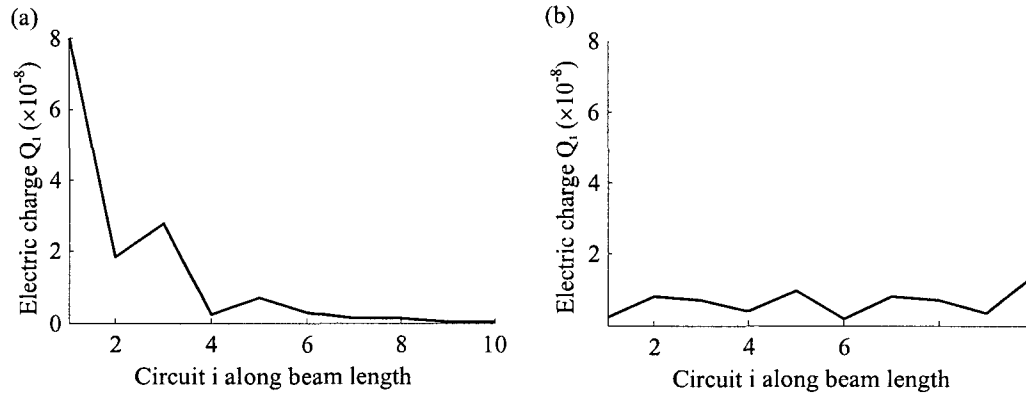


**Figure 41. Electric charge in each circuit as shown in Figure 38, when the excitation frequency is (a) within or (b) out of the “all-attenuation zone”.**

Another potential application of the proposed electro-mechanical periodic system is to utilize the electrical energy in the circuitry. The electrical energy converted from the vibration of the host structure may be collected to power, for instance, wireless sensors, or stored for later usage (Liao and Sodano 2009; Liao and Sodano 2008). In such case, the system serves as an energy harvesting device. One may store the energy in distributed capacitive elements such as batteries, which could replace  $C_c$ 's in the aforementioned configurations. The electrical energy is then proportional to the electric current in each circuit.

Figure 41 shows an example where I use the same configuration as in Figure 38(a) to study the electric charge in the coupled circuits. This time I again choose  $L = 0.0063\text{H}$  and  $C_c = 1.68\mu\text{F}$  so that each subsystem's propagation constants are still the same as in Figure 37. Recall the mechanical vibration of the host beam structure can be significantly reduced by the integrated piezoelectric periodic circuitry, even though there is no mechanical damping or electrical

resistance involved. Comparing Figure 41(a) to Figure 41(b), we can tell there is more electric charge in the circuitry when the frequency is within the “all-attenuation zone”. Recall that in this “all-attenuation zone”, vibration of the host beam has been reduced significantly, which doesn’t involve energy dissipation as I have assumed no damping for the beam and no resistance in the circuitry. By integrating the connected piezoelectric circuits, I have an extra wave pair for energy propagation. The mechanical energy flow originally propagating in the beam now has evolved into the electro-mechanical energy flow propagating in the electro-mechanical periodic system. Qualitatively speaking, the reduced mechanical energy has thus been converted into the electrical form and redistributed across the circuitry. Since the electrical charge in each circuit should experience similar attenuation due to the “all-attenuation zone” feature, I should observe more overall electrical charge but distributed in a decay pattern across the circuitry. From this example, I can conclude that the electro-mechanical system may improve energy harvesting efficiency.

#### 5.4.3. Tunability of the integrated electro-mechanical system

One advantage of integrating electrical circuitries onto the mechanical structure is that the system dynamics, or wave propagation properties, can be tuned in real-time by varying only the electrical parameters. I mainly have two tunable parameters: the inductance  $L$  and the coupling capacitance  $C_c$  (Tang and Wang 2001). To facilitate further discussions, I define the ratio of  $C_p$  over  $C_c$  as a nondimensionalized tuning parameter

$$r_c = \frac{C_p}{C_c} \quad (59)$$

The capacitance of the piezoelectric transducer  $C_p$  is determined by its geometric and material properties that cannot be changed online. Therefore,  $C_p$  is not tunable and the ratio  $r_c$  represents

the tuning of  $C_c$ . Another nondimensionalized parameter  $r_L$  represents the tuning of the inductance  $L$ . It is defined as

$$r_L = \frac{\Omega^{\text{elec}}}{\Omega^{\text{mech}}} = \frac{\zeta}{l^2} \sqrt{\frac{EILC_p}{m}} \quad (60)$$

Let's first discuss the tuning of the coupling capacitance  $C_c$ . Recall that Figure 35(a) shows the propagation constant for the case  $L=0.0063\text{H}$  and  $C_c=0.84\mu\text{F}$ , which can serve as a starting point for the following discussion. In that case, the nondimensionalized parameters are  $r_c=10$  and  $r_L=1$ , meaning the coupling capacitance  $C_c$  is selected as 10 times of  $C_p$  and the inductance  $L$  is selected to make  $\Omega^{\text{mech}} = \Omega^{\text{elec}}$ . If I adjust the value of  $r_c$  while holding  $r_L=1$  fixed, then the resulting propagation constants can be obtained as in Figure 42. The width of the “all-attenuation zone” changes as  $r_c$  increases from  $r_c=8$  to  $r_c=25$ . Recall that the coupling capacitance  $C_c$  determines the width of the periodic circuitry's own passband. Also, the “all-attenuation zone” only appears within the periodic circuitry's own passband. Therefore, the change in the coupling capacitance  $C_c$  indirectly affects the width of the “all-attenuation zone”. Since the “all-attenuation zone” may benefit both the vibration isolation and energy harvesting applications as evidenced by the preceding case studies, its width becomes an important factor for the overall system performance. However, it is not a simple linear relation between the two.

Another parameter that plays an important role is the inductance  $L$ . From (60) we can tell that the inductance value affects the electrical resonance frequency and thus the ratio  $r_L$ . By tuning the inductance, I can change the location of the “all-attenuation zone” along the frequency axis. Figure 43 shows the propagation constants for different  $r_L$  values when holding  $r_c=20$  fixed. Compared with Figure 37(c) where  $r_L=1$ , Figure 43(a) and Figure 43(b) depict the shifting of the “all-attenuation zone” as  $r_L$  increases from 0.8 to 1.2. We can see that the tuning of  $L$  clearly



determines where the overlapping and/or crossing of the curves occur. Altogether, I can implement tunable vibration isolation using the electro-mechanical periodic system with  $L$  and  $C_c$  as the tuning factors

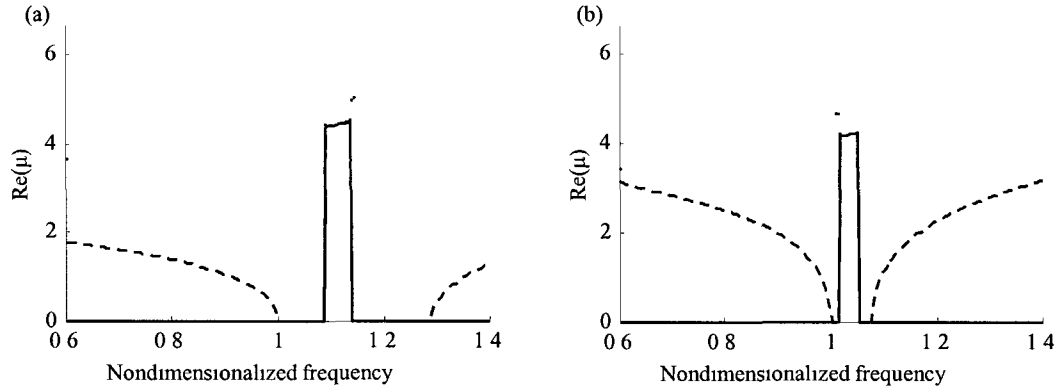


**Figure 42. Three propagation constants (solid line, dotted line and dashed line) versus nondimensionalized frequency when (a)  $r_c = 8$  or (b)  $r_c = 25$ . The inductance  $L$  has been chosen to fix  $r_L = 1$**

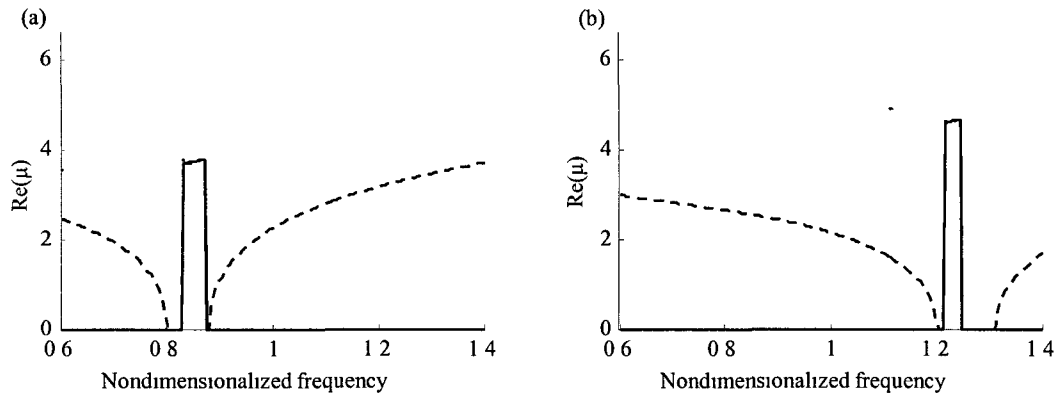


**Figure 43. Three propagation constants (solid line, dotted line and dashed line) versus nondimensionalized frequency when (a)  $r_L = 0.8$  or (b)  $r_L = 1.2$ .  $r_c$  has been fixed at  $r_c = 20$**

### 5.5 Concluding remarks

In this chapter, a multi-coupled electro-mechanical periodic system is proposed to control the dynamic response and energy flow. Piezoelectric transducers connected through circuitry are integrated onto the host mechanical structure. The coupling provided by the electrical subsystem

provides additional degree of freedom and thus tunability on the overall system dynamics. A transfer-matrix based method is adopted for the dynamic analysis, where propagation constants of the electro-mechanical harmonic waves can be calculated from the eigenvalues of the transfer matrix. By carefully selecting the electrical parameters, I can observe frequency passbands, stopbands and complexbands for each wave pair. One feature of the integrated system is that I can find a frequency range in which all three pairs of waves experience attenuation. That frequency range is named “all-attenuation zone” because of its effects in the wave coordinates. Case study shows how the electrical parameters affect the overall vibration in the original coordinates. The inductance has an impact on the location of the “all-attenuation zone” along the frequency axis, while the coupling capacitance affects its width. The proposed electro-mechanical periodic system is particularly suitable for isolation of tonal vibrations with varying frequency (e.g., wind turbine gearbox-induced vibration). It can also be integrated into wireless sensor to harvest energy corresponding to varying frequency excitation.

## Chapter 6. Conclusions and Future Work

Damage detection and health monitoring of mechanical systems have long been an important part of regular operation and maintenance. It is particularly valuable for mechanical systems located in remote areas. As microelectronics and information technologies evolve drastically, innovative monitoring and diagnosis systems have emerged. Vibration, acoustic, wave propagation and other sensor signals become viable inputs for structural health monitoring and damage detection. An autonomous methodology means the system can be diagnosed with little or no human intervention. By robust I mean the diagnosis performance is not affected by various operational and environmental noises. For complex mechanical systems located in remote areas such as wind turbine systems, such autonomous and robust diagnosis of damage, defects or faults is of critical value.

In Chapter 2 and Chapter 3, a series of signal processing and decision making developments have been conducted to make the damage detection and condition monitoring autonomous and robust. For example, a wavelet based feature extraction technique is adopted to capture fault sensitive features in the time-frequency domain. Statistical analysis is used to quantitatively investigate the existence or severity of various damage and faults. Also, multiple sensors are often deployed for the purpose of information redundancy in various applications, especially when individual sensor's performance may be compromised under certain constraints. The autonomous and robust methodology requires the information contained in multiple data collections to be fused together before diagnosis. Theoretical modeling, numerical simulation and experimental investigation have been conducted to demonstrate the effectiveness and efficiency of the proposed methodology in various engineering situations. The algorithms developed in this dissertation research are highly transferable to other mechanical structures or rotating machineries.

A wireless sensing platform has been built to investigate the feasibility and implementation of collecting and processing sensor signals on board and then transmitting them to a base station for further processing and decision making. Trade-off has to be made between local computational costs and energy consumption of the wireless transmission. Aiming at fundamental breakthroughs in vibration-based energy harvesting and vibration suppression, an electro-mechanical tailoring scheme has been developed to explore the manipulation of vibratory energy in structural systems. The proposed methodology is to use a periodic circuitry with piezoelectric transducers bonded onto the mechanical structure. It is identified that such an arrangement can create a variety of frequency bands that correspond to different wave/energy propagation patterns. Theoretical study and numerical simulation agrees that mechanical and electrical energy can be redistributed by tuning the circuitry parameters such like inductance and capacitance. Moreover, such an electro-mechanical periodic system can also be used for vibration control to prevent excessive vibration of the host structure, which in return can further reduce maintenance costs.

The ultimate goal of research along the direction of this dissertation work is to synthesize an autonomous and self-powered sensor network to robustly detect, diagnose and identify various faults/damages/failures of the monitored mechanical system, and eventually to realize simultaneous monitoring and maintenance to extend the service life of structural/machinery systems such as wind turbines. Building upon the foundational elements laid down in this dissertation, future work may include:

- Implementing the decision making algorithms developed in Chapter 2 and Chapter 3 into the wireless sensing platform developed in Chapter 4, and developing sensor optimization by carrying out trade-off studies among local signal processing, decision making, and power consumption.

- Synthesizing a self-powering wireless sensor by integrating an energy harvesting piezoelectric circuitry based on the new concept introduced in Chapter 5 into the above mentioned wireless sensor node for sustainable damage detection and health monitoring.
- Developing a concurrent health monitoring and vibration control system that is capable of continuously elucidating the condition/health of structures/machineries and meanwhile controlling/isolating wave/energy flow using the energy localization results outlined in Chapter 5 for fundamentally enhanced performance/durability.

## Bibliography

1. Alleyne, D. N. and Cawley, P. 1992. The interaction of lamb waves with defects. *IEEE Transactions on Ultrasonics, Ferroelectrics, and Frequency Control* 38(1)-97.
2. Anton, S. R. and Sodano, H. A. 2007. A review of power harvesting using piezoelectric materials (2003-2006). *Smart Materials and Structures* 16 (3).
3. Asiri, S. 2007. Tunable mechanical filter for longitudinal vibrations. *Shock and Vibration* 14 (5) 377-91.
4. Bouzit, D. and Pierre, C. 2000. Wave localization and conversion phenomena in multi-coupled multi-span beams. *Chaos, Solitons & Fractals* 11 (10) 1575-96.
5. Brandstein, M. S. and H. F. Silverman. 1997. A robust method for speech signal time-delay estimation in reverberant rooms. *IEEE International Conference on Acoustics, Speech, and Signal Processing*, .
6. Brillouin, L. 1953. *Wave propagation in periodic structures; electric filters and crystal lattices*. 2d , with corrections a additions ed. New York: Dover Publications.
7. Byington, C., M. Watson, H. Lee and M. Hollins. 2008. Sensor-level fusion to enhance health and usage monitoring systems. 64th Annual Forum - AHS International, Montreal.
8. Casadei, F., Ruzzene, M., Dozio, L. and Cunefare, K. A. 2010. Broadband vibration control through periodic arrays of resonant shunts: Experimental investigation on plates. *Smart Materials and Structures* 19 (1) 015002.
9. Castanier, M. P. and Pierre, C. 1993. Individual and interactive mechanisms for localization and dissipation in A mono-coupled nearly-periodic structure. *Journal of Sound and Vibration* 168 (3) 479-505.
10. Cawley, P. and Adams, R. D. 1979. Location of defects in structures from measurements of natural frequencies. *J Strain Anal Eng Des* 14 (2) 49-57.
11. Coifman, R. R. and Wickerhauser, M. V. 1992. Entropy-based algorithms for best basis selection. *IEEE Transactions on Information Theory* 38 (2 pt II) 713-8.
12. Crawley, E. F. and Anderson, E. H. 1990. Detailed models of piezoceramic actuation of beams. *Journal of Intelligent Material Systems and Structures* 1 (1) 4-25.
13. Daubechies, I. 1992. *Ten lectures on wavelets*. Philadelphia, PA: Society for Industrial and Applied Mathematics.
14. Duhamel, D., Mace, B. R. and Brennan, M. J. 2006. Finite element analysis of the vibrations of waveguides and periodic structures. *Journal of Sound and Vibration* 294 (1-2) 205-20.

15. Dunia, R. and Qin, S. J. 1998. Joint diagnosis of process and sensor faults using principal component analysis. *Control Engineering Practice* 6 (4) 457-69.
16. Fang, X. and J. Tang. 2006. Damage detection of engine bladed-disks using multivariate statistical analysis. *Smart Structures and Materials 2006 - Sensors and Smart Structures Technologies for Civil, Mechanical, and Aerospace Systems*, San Diego, CA.
17. Ganesan, R., Das, T. K. and Venkataraman, V. 2004. Wavelet-based multiscale statistical process monitoring: A literature review. *IIE Transactions (Institute of Industrial Engineers)* 36 (9) 787-806.
18. Girdhar, P. and Scheffer, C. 2004. *Practical machinery vibration analysis and predictive maintenance*. Oxford, United Kingdom: Newnes.
19. Giurgiutiu, V. 2005. Tuned lamb wave excitation and detection with piezoelectric wafer active sensors for structural health monitoring. *Journal of Intelligent Material Systems and Structures* 16 (4) 291-305.
20. Giurgiutiu, V. 2003. Lamb wave generation with piezoelectric wafer active sensors for structural health monitoring. *Smart Structures and Materials 2003: Smart Structures and Integrated Systems*, San Diego, CA.
21. Giurgiutiu, V., Zagari, A. and Bao, J. J. 2002. Piezoelectric wafer embedded active sensors for aging aircraft structural health monitoring. *Structural Health Monitoring* 1 (1) 41-61.
22. Gry, L. and Gontier, C. 1997. Dynamic modelling of railway track: A periodic model based on a generalized beam formulation. *Journal of Sound and Vibration* 199 (4) 531-58.
23. Hagood, N. W. and von Flotow, A. 1991. Damping of structural vibrations with piezoelectric materials and passive electrical networks. *Journal of Sound and Vibration* 146 (2) 243-68.
24. Hall, D. L. and McMullen, S. A. H. 2004. *Mathematical techniques in multisensor data fusion*. Boston, MA: Artech House.
25. Hodges, C. H. 1982. Confinement of vibration by structural irregularity. *Journal of Sound and Vibration* 82 (3) 411-24.
26. Hollkamp, J. J. 1994. Multimodal passive vibration suppression with piezoelectric materials and resonant shunts. *Journal of Intelligent Material Systems and Structures* 5 (1) 49-57.
27. Hou, Z., Noori, M. and Amand, R. S. 2000. Wavelet-based approach for structural damage detection. *Journal of Engineering Mechanics* 126 (7) 677-83.
28. IEEE. 1987. ANSI/IEEE std 176-1987, IEEE standard on piezoelectricity ANSI/IEEE Std 176-1987.
29. Jackson, J. E. 2003. *A user's guide to principal components*. New York etc.: Wiley-Interscience.

30. Jardine, A. K. S., Lin, D. and Banjevic, D. 2006. A review on machinery diagnostics and prognostics implementing condition-based maintenance. *Mechanical Systems and Signal Processing* 20 (7) 1483-510.
31. Johnson, R. A. and Wichern, D. W. 2007. *Applied multivariate statistical analysis*. 6th ed. Englewood Cliffs, N.J.: Prentice-Hall.
32. Kessler, S. S. and C. T. Dunn. 2003. Optimization of lamb wave actuating and sensing materials for health monitoring of composite structures. *Smart Structures and Materials 2003: Smart Structures and Integrated Systems*, San Diego, CA.
33. Kim, H. and Melhem, H. 2004. Damage detection of structures by wavelet analysis. *Engineering Structures* 26 (3) 347-62.
34. Knapp, C. and Carter, G. 1976. The generalized correlation method for estimation of time delay. *Acoustics, Speech and Signal Processing, IEEE Transactions on* 24 (4) 320-7.
35. Konstantinides, K. and Yao, K. 1988. Statistical analysis of effective singular values in matrix rank determination. *IEEE Transactions on Acoustics, Speech, and Signal Processing* 36 (5) 757-63.
36. Lenk, J. D. 1993. *McGraw-hill circuit encyclopedia and troubleshooting guide*. New York: McGraw-Hill.
37. Liao, Y. and Sodano, H. A. 2009. Optimal parameters and power characteristics of piezoelectric energy harvesters with an RC circuit. *Smart Materials and Structures* 18 (4) 045011.
38. Liao, Y. and Sodano, H. A. 2008. Model of a single mode energy harvester and properties for optimal power generation. *Smart Materials and Structures* 17 (6) 065026.
39. Liggins, M. E., Hall, D. L. and Llinas, J. 2009. *Handbook of multisensor data fusion : Theory and practice*. Boca Raton, FL: CRC Press.
40. Lin, X. and Yuan, F. G. 2001a. Detection of multiple damages by prestack reverse-time migration. *AIAA Journal* 39 (11) 2206-15.
41. Lin, X. and Yuan, F. G. 2001b. Diagnostic lamb waves in an integrated piezoelectric sensor/actuator plate: Analytical and experimental studies. *Smart Materials and Structures* 10 (5) 907.
42. Liu, B. 2003. Adaptive harmonic wavelet transform with applications in vibration analysis. *Journal of Sound and Vibration* 262 (1) 45-64.
43. Lu, C. -. and Hsu, Y. -. 2002. Vibration analysis of an inhomogeneous string for damage detection by wavelet transform. *International Journal of Mechanical Sciences* 44 (4) 745-54.
44. Lu, Y. and J. Tang. 2009. Prototyping a wireless sensing platform for acoustic emission signals collected by microphone arrays. *Proceedings of SPIE, Smart Structures / NDE*, San Diego, CA.



45. Lu, Y., Wang, X., Tang, J. and Ding, Y. 2008. Damage detection using piezoelectric transducers and the lamb wave approach: II. robust and quantitative decision making. *Smart Materials and Structures* 17 (2).
46. Lymberopoulos, D., Teixeira, T. and Savvides, A. 2008. Macroscopic human behavior interpretation using distributed imager and other sensors. *Proceedings of the IEEE* 96 (10) 1657-77.
47. Lynch, J. P., Law, K. H., Kiremidjian, A. S., Carryer, E., Farrar, C. R., Sohn, H., Allen, D. W., Nadler, B. and Wait, J. R. 2004 Design and performance validation of a wireless sensing unit for structural monitoring applications. *Structural Engineering and Mechanics* 17 (3-4) 393-408.
48. Lynch, J. P., Wang, Y., Loh, K. J., Yi, J. -. and Yun, C. -. 2006. Performance monitoring of the geumdang bridge using a dense network of high-resolution wireless sensors. *Smart Materials and Structures* 15 (6) 1561-75.
49. MacGregor, J. F. and Kourtı, T. 1995. Statistical process control of multivariate processes. *Control Engineering Practice* 3 (3) 403-14.
50. Mangaraju, V. and Sonti, V. R. 2004. Wave attenuation in periodic three-layered beams: Analytical and FEM study. *Journal of Sound and Vibration* 276 (3-5) 541-70.
51. Mead, D. J. 1975. Wave propagation and natural modes in periodic systems: I. mono-coupled systems. *Journal of Sound and Vibration* 40 (1) 1-18.
52. Mead, D. J. 1973. A general theory of harmonic wave propagation in linear periodic systems with multiple coupling. *Journal of Sound and Vibration* 27 (2) 235-60.
53. Naidu, V. P. S. and Raol, J. R. 2008. Pixel-level image fusion using wavelets and principal component analysis. *Defence Science Journal* 58 (3) 338-52.
54. Newland, D. E. 1994. Harmonic and musical wavelets. *Proceedings: Mathematical and Physical Sciences* 444 (1922) 605-20.
55. Newland, D. E. 1993. Harmonic wavelet analysis. *Proceedings: Mathematical and Physical Sciences* 443 (1917) 203-25.
56. Park, C. H. and Baz, A. 2005. Vibration control of beams with negative capacitive shunting of interdigital electrode piezoceramics. *Journal of Vibration and Control* 11 (3) 331.
57. Park, S., Yun, C. -, Roh, Y. and Lee, J. -. 2006. PZT-based active damage detection techniques for steel bridge components. *Smart Materials and Structures* 15 (4) 957-66.
58. Peng, Z. K. and Chu, F. L. 2004. Application of the wavelet transform in machine condition monitoring and fault diagnostics: A review with bibliography. *Mechanical Systems and Signal Processing* 18 (2) 199-221.
59. Pestel, E. C. and Leckie, F. A. 1963. *Matrix methods in elastomechanics*. New York: McGraw-Hill.

60. Pierre, C., Castanier, M. P. and Chen, W. J. 1996. Wave localization in multi-coupled periodic structures: Application to truss beams. *Applied Mechanics Reviews* 49 (2) 65-86.
61. Quek, S. T., Wang, Q., Zhang, L. and Ong, K. H. 2001. Practical issues on the detection of damage in beams using wavelets. *Smart Materials and Structures* 10 (5) 1009-17.
62. Raghavan, A. and Cesnik, C. E. S. 2005. Finite-dimensional piezoelectric transducer modeling for guided wave based structural health monitoring. *Smart Materials and Structures* 14 (6) 1448-61.
63. Rao, M. S. and Narayanan, S. 2007. Active control of wave propagation in multi-span beams using distributed piezoelectric actuators and sensors. *Smart Materials and Structures* 16 (6) 2577-94.
64. Rice, J. A. and B. F. Spencer Jr. 2008. Structural health monitoring sensor development for the Imote2 platform. *Sensors and Smart Structures Technologies for Civil, Mechanical, and Aerospace Systems 2008*, San Diego, CA.
65. Romeo, F. and Paolone, A. 2007. Wave propagation in three-coupled periodic structures. *Journal of Sound and Vibration* 301 (3-5) 635-48.
66. Rose, J. L. 2004. *Ultrasonic waves in solid media*. Cambridge, UK: Cambridge Univ. Press.
67. Schmidt, R. O. 1986. MULTIPLE EMITTER LOCATION AND SIGNAL PARAMETER ESTIMATION. *IEEE Transactions on Antennas and Propagation* AP-34 (3) 276-80.
68. Seber, G. A. F. 1984. *Multivariate observations*. New York etc.: John Wiley and Sons.
69. Singh, A., Pines, D. J. and Baz, A. 2004. Active/passive reduction of vibration of periodic one-dimensional structures using piezoelectric actuators. *Smart Materials and Structures* 13 (4) 698-711.
70. Staszewski, W. J. 2002. Intelligent signal processing for damage detection in composite materials. *Composites Science and Technology* 62 (7-8) 941-50.
71. Tang, J. and Wang, K. W. 2001. Active-passive hybrid piezoelectric networks for vibration control: Comparisons and improvement. *Smart Materials and Structures* 10 (4) 794.
72. Tang, J. and Wang, K. W. 2003. Vibration delocalization of nearly periodic structures using coupled piezoelectric networks. *Journal of Vibration and Acoustics, Transactions of the ASME* 125 (1) 95-108.
73. Tonge, T. N. and Chen, T. 2004. Control of longitudinal wave propagation in conical periodic structures. *JVC/Journal of Vibration and Control* 10 (12) 1795-811.
74. Tseng, K. K. H. and Naidu, A. S. K. 2002. Non-parametric damage detection and characterization using smart piezoceramic material. *Smart Materials and Structures* 11 (3) 317-29.
75. Tua, P. S., Quek, S. T. and Wang, Q. 2004. Detection of cracks in plates using piezo-actuated lamb waves. *Smart Materials and Structures* 13 (4) 643-60.

76. Wan, F., Xu, Q. and Li, S. 2004. Vibration analysis of cracked rotor sliding bearing system with rotor-stator rubbing by harmonic wavelet transform. *Journal of Sound and Vibration* 271 (3-4) 507-18.
77. Wang, K. W. and Tang, J. 2008. Adaptive structural systems with piezoelectric transducer circuitry. New York: Springer.
78. Wang, Q., Wang, D. and Su, X. 1999. Crack detection of structure for plane problem with spatial wavelets. *Acta Mechanica Sinica/Lixue Xuebao* 15 (1) 50-1.
79. Wang, W. J. and McFadden, P. D. 1995. Application of orthogonal wavelets to early gear damage detection. *Mechanical Systems and Signal Processing* 9 (5) 497-507.
80. Wang, X., Lu, Y. and Tang, J. 2008. Damage detection using piezoelectric transducers and the lamb wave approach: I. system analysis. *Smart Materials and Structures* 17 (2).
81. Wang, X. and Tang, J. 2010. An enhanced piezoelectric impedance approach for damage detection with circuitry integration. *Smart Materials and Structures* 19 (4) 045001.
82. Wornell, G. M. 1996. Signal processing with fractals :A wavelet-based approach. Upper Sadalle River, New Jersey: Prentice Hall.
83. Xu, M., Song, W. -, Huang, R., Peng, Y., Shirazi, B., Lahusen, R., Kiely, A., et al. 2009. Design of smart sensing components for volcano monitoring. *Pervasive and Mobile Computing* 5 (5) 639-53.
84. Yan, R. and Gao, R. X. 2010. Harmonic wavelet-based data filtering for enhanced machine defect identification. *Journal of Sound and Vibration* 329 (15) 3203-17.
85. Yeh, J. and Chen, L. 2006. Wave propagations of a periodic sandwich beam by FEM and the transfer matrix method. *Composite Structures* 73 (1) 53-60.
86. Yu, L. and Giurgiutiu, V. 2005. Advanced signal processing for enhanced damage detection with piezoelectric wafer active sensors. *Smart Structures & Systems* 1 (2) 185-215.
87. Yu, H., Wang, K. W. and Zhang, J. 2006. Piezoelectric networking with enhanced electromechanical coupling for vibration delocalization of mistuned periodic structures-theory and experiment. *Journal of Sound and Vibration* 295 (1-2) 246-65.